UNIVERSITY OF CALIFORNIA, MERCED

MOLECULAR DYNAMICS SIMULATION OF NANOSCALE WEAR IN ATOMIC FORCE MICROSCOPY

by

Xiaoli Hu

A dissertation submitted in partial satisfaction of the
requirements for the degree of
Doctor of Philosophy

in

Mechanical Engineering

Committee in charge:
Professor Ashlie Martini, Advisor
Professor Min Hwan Lee
Professor Yanbao Ma
Professor Tao Ye

The Dissertation of Xiaoli Hu is approved, and it is acceptable in quality and form for publication on microfilm and electronically:

Professor Ashlie Martini, Advisor Date

Professor Min Hwan Lee Date

Professor Yanbao Ma Date

Professor Tao Ye Date

University of California, Merced

2017

To all the blessings of life

ACKNOWLEDGEMENTS

I have so many people to thank and this is a short list of them who helped me come here.

First and foremost, I wish to thank my advisor, Dr. Ashlie Martini, for her patience, support, guidance and encouragement for my research throughout the process. I sincerely appreciate that I have had the opportunity to work with her and learned from her about knowledge in tribology and dedication to scientific research.

I want to thank Dr. Yanbao Ma, Dr. Min Hwan Lee, and Dr. Tao Ye for serving on my PhD committee and providing scientific guidance and support along the way.

I appreciate the opportunities to work with so many great people at various institutions: at Iowa State University: Christopher J. Tourek and Dr. Sriram Sundararajan; at University of Calgary (Canada): Nicholas Chan and Dr. Philip Egberts; at Lawrence Berkeley National Laboratory: Dr. Virginia Altoe; at University of Pittsburgh: Sai Bharadwaj Vishnubhotla, Dr. Subarna Khanal and Dr. Tevis Jacobs. I am also grateful for helpful assistance from Tzu-Ray Shan related to the charge-optimized many-body potential.

I also want to thank Dr. Christopher Viney and Dr. J. Arthur Woodward for their guidance and encouragement in classes.

I would like to thank the former and current group members of Martini Research Group: Drs. Chun Tang, Taeil Yi, Yalin Dong, Xiawa Wu, Gustavo Brunetto, Jejoon Yeon, Eric Osei-Agyemang, Zhijiang Ye, Hongyu Gao and Uma Ramasamy, Michelle Len, Duval Johnson, Sean Lantz, Rimei Chen, Azhar Vellore, Arash Khajeh, Mohammad Rasool Vazirisereshk for helpful discussions, guidance and much fun.

I would like to take the opportunity to thank the administrative staff in the School of Engineering for their help with administrative requirements during my graduate studies, including Tomiko Hale and Tamika Hankston. I want to thank Belinda Braunstein for her help in English pronunciation and Becky Mirza for assistance in visa problems.

Lastly, I would like to thank my parents and my sister for their unconditional support through the years. I also would like to thank my good friend Ye Liu for her inspiration in difficult times.

CURRICULUM VITAE

EDUCATION

- Ph.D. in Mechanical Engineering, University of California-Merced (Merced, CA, US), 2017 (expected).
- M.S. in Atomic and Molecular Physics, Graduate University of Chinese Academy of Sciences (Beijing, China), 2012.
- B.S. in Applied Physics, Beijing University of Aeronautics and Astronautics (Beijing, China), 2009.

HONORS AND AWARDS

- UC Merced Spring 2017 Graduate Deans Dissertation Fellowship (2017)
- Chinese Government Award for Outstanding Self-Financed Student Abroad (2017)
- Finalist, BASF Science Competition (2016)
- STLE Northern California Research Scholarship (2015)
- 1st Place, Student Poster Competition, Society of Tribologists and Lubrication Engineers Annual Meeting and Exhibition (2014)

PUBLICATIONS

1. **Xiaoli Hu**, M. Virginia P. Altoe and Ashlie Martini, Amorphization-assisted nanoscale wear during the running-in process, *Wear*, **370-371**, 46-50 (2017)
2. **Xiaoli Hu**, Nicholas Chan, Ashlie Martini and Philip Egberts, Tip convolution on HOPG surfaces measured in AM-AFM and interpreted using a combined experimental and simulation approach, *Nanotechnology*, **28**, 025702 (2017)
3. **Xiaoli Hu**, Philip Egberts, Yalin Dong and Ashlie Martini, Molecular dynamics simulation of amplitude modulation atomic force microscopy, *Nanotechnology*, **26**, 235705 (2015)

4. **Xiaoli Hu**, and Ashlie Martini, Atomistic simulation of the effect of roughness on nanoscale wear, *Computational Materials Sciences*, **102**, 208-212 (2015)

5. **Xiaoli Hu**, Sriram Sundararajan and Ashlie Martini, The effects of adhesive strength and load on material transfer in nanoscale wear, *Computational Materials Sciences*, **95**, 464-469 (2014)

6. **Xiaoli Hu**, Chris Tourek, Zhijiang Ye, Sriram Sundararajan and Ashlie Martini, Structural and Chemical Evolution of the Near-Apex Region of an Atomic Force Microscope Tip Subject to Sliding, *Tribology Letters*, **53**, 181-187 (2014)

ORAL PRESENTATIONS

1. **Xiaoli Hu**, Nicholas Chan, Philip Egberts and Ashlie Martini, Surface characterization using atomistic models of amplitude modulation atomic force microscopy, *STLE Tribology Frontiers Conference*, Chicago IL (November 2016)

2. **Xiaoli Hu**, and Uma Shantini Ramasamy, Novel method correlating chemistry and functionality, *BASF Science Competition*, Tarrytown NY (August 2016)

3. **Xiaoli Hu**, and Ashlie Martini, How simulations can contribute to our understanding of tribology and lubrication Engineering, *STLE Northern California Section Meeting*, Berkeley CA (June 2016)

4. **Xiaoli Hu**, M. Virginia P. Altoe and Ashlie Martini, Modeling nanoscale wear of an atomic force microscope tip during run-in, *STLE Tribology Frontiers Conference*, Denver CO (October 2015)

5. **Xiaoli Hu**, Philip Egberts, Yalin Dong, Nicholas Chan and Ashlie Martini, Molecular dynamics simulation of amplitude modulation atomic force microscopy, *STLE 2015 Annual Meeting*, Dallas TX (May 2015)

6. **Xiaoli Hu**, and Ashlie Martini, Modelling of nanoscale wear and adhesion of an atomic force microscope tip, *STLE Tribology Frontiers Conference*, Chicago IL (October 2014)

POSTER PRESENTATIONS

1. **Xiaoli Hu**, M. Virginia P. Altoe and Ashlie Martini, Modeling nanoscale wear of an atomic force microscope tip during run-in, *STLE 2016 Annual Meeting*, Las Vegas NV (May 2016)

2. **Xiaoli Hu**, and Ashlie Martini, The effect of roughness on nanoscale adhesion and wear, *STLE 2014 Annual Meeting*, Orlando FL (May 2014)

3. **Xiaoli Hu**, Chris Tourek, Zhijiang Ye, Sriram Sundararajan and Ashlie Martini, Modeling of Nanoscale Wear between Metals, *STLE 2013 Annual Meeting*, Detroit MI (May 2013)

TABLE OF CONTENTS

LIST OF FIGURES

LIST OF TABLES

ABSTRACT

Wear is the loss or displacement of material due to contact or relative motion between bodies. Wear plays an important role in the performance of tribological components and is undesirable in most machine applications. Wear is also important for small scale instruments such as the atomic force microscope (AFM). The AFM has become one of the most widely used tools in the fields of nanoscience and nanotechnology for the preparation and analysis of surfaces and materials. It has been shown that AFM tip wear affects the performance and operating life of the AFM used for applications such as nanomanufacturing, nanoscale metrology and probe-based data storage applications. As AFM techniques advance from use in research laboratories to industrial applications, the durability and stability of the tip itself become more critical. However, the fundamental wear mechanisms and how wear affects the performance of precision components at the nanoscale are not fully understood. Thus, it is necessary to explore the qualitative as well as quantitative nature of nanoscale wear.

In this thesis, we studied the mechanisms of nanoscale wear in contact mode AFM and explored the effect of tip wear on topography measurement in amplitude modulation AFM using molecular dynamics (MD) simulation. We characterized wear in terms of the structural and chemical evolution of the sliding surfaces, which revealed that nanoscale wear can occur through both adhesion and abrasion. Wear during running-in was also studied and it was observed that crystalline materials may become amorphous before they are removed from the surface. We then studied the effects of load, adhesive strength and surface roughness on nanoscale wear, and the results suggested that it is possible to identify optimum sliding conditions to minimize wear. In addition, we developed a model of amplitude modulation AFM and studied the effect of nanoscale wear on topography measurement. It was found that the resolution of amplitude modulation AFM measurements could be correlated to tip size and this relationship was also affected by the deformation of the materials. This research provides important insights into the fundamental mechanisms of nanoscale wear, which will lead to a better understanding of this technologically-important phenomenon that controls the failure of systems from the macroscale to the nanoscale, with substantial economic, energetic, and environmental impacts.

Chapter 1

INTRODUCTION

1.1 Atomic Force Microscopy

The atomic force microscope (AFM) is one of the most important tools used to observe surface features at the nanoscale [1–4]. The AFM consists of a cantilever with a sharp tip at its end, which is used to scan specimen surfaces. The fundamental concept behind AFM measurement is the relationship between AFM tip-sample interaction force and the relative distance between the AFM tip and sample. Figure 1.1 shows the major components of a typical AFM. The operating principles of AFM are as follows [1, 5–7]: a cantilever with a sharp tip (the radius of the tip is typically a few nanometers) is attached to a piezoelectric transducer. Light from a laser beam is reflected by the cantilever and received by a quadrant photodiode. When the cantilever approaches the sample, it bends due to the interaction force between tip and surface. Thus, the position of the light on the quadrant photocell changes. This signal can be used as the input to a servo system and become a measure of the deflection of the cantilever due to the force between the tip and surface.

AFM has three primary operation modes [5–7]: contact mode, amplitude modulation (AM-AFM), and frequency modulation AFM (FM-AFM). Among these three modes, contact mode AFM is considered static while AM-AFM and FM-AFM are considered dynamic. Figure 1.2 shows the interaction force between the tip and substrate as a function of the distance between them. It should be noted that contact mode AFM operates in the repulsive force region, where the total force is positive and decreases with increasing distance. In both AM-AFM and FM-AFM, the AFM tip is oscillated above the surface due to an external excitation force applied on the cantilever. During tip oscillation, the tip-sample interaction force could be attractive or repulsive in AM-AFM while it is generally only attractive in FM-AFM. In addition to imaging the topography of surfaces under various environments, AFM is also widely used in nanomanufacturing methods such as nanomanipulation and nanolithography [8–11].

1.1.1 Contact Mode AFM

In contact mode AFM, the AFM tip stays close to the sample, such that the tip-sample interaction force is repulsive. The cantilever deflection is used as the

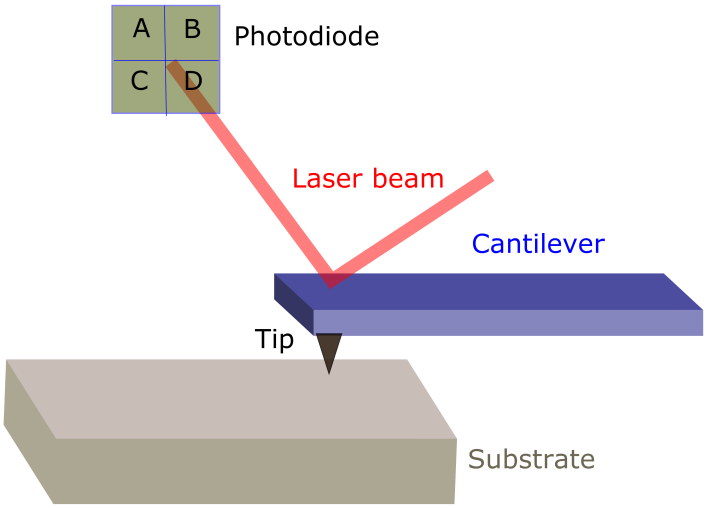

Figure 1.1: A simplified schematic of an AFM in which the tip scans over the surface and the interaction force between the tip and substrate causes the cantilever to bend, changing the position of the laser beam on the photodiode.

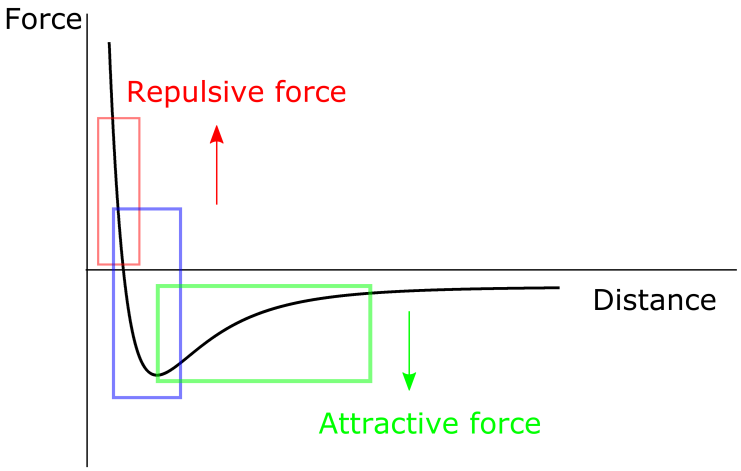

Figure 1.2: Interaction force between the tip and substrate as a function of distance, which reflects different types of interactions at different tip-sample distances. The regime in red indicates where contact mode AFM operates, the regime in blue indicates where AM-AFM operates and the regime in green indicates where FM-AFM operates.

measurement of tip-sample interaction force, $F_{ts} = k_c \Delta x$, where k_c is the cantilever stiffness and Δx is the cantilever deflection. The cantilever stiffness is a critical parameter in AFM [1]. The typical cantilever stiffness in contact mode AFM is $0.01 \sim 10$ N/m. The cantilever stiffness should be smaller than the effective force constant between the tip and sample so that the cantilever deflection is larger than the tip/sample deformation [12]. When contact AFM is applied to measure the surface topography, the cantilever deflection is kept constant by adjustment of the cantilever base or sample position, which ensures that the interaction force between the tip and sample is constant as the tip scans over the surface. The same interaction force at every surface position implies that the distance between the tip and substrate is the same. Thus, when the cantilever scans over the surface, it follows the surface topography.

The application of contact AFM is also increasingly used for tribological studies of engineering surfaces at the nanoscale. For example, AFM has been employed to measure friction with atomic-scale contrast [13–16]. In measurement of friction force at the nanoscale, the tip is brought into contact with the sample surface. The normal load on the tip-sample contact is measured as normal bending of the cantilever. When there is relative sliding between the tip and sample, the lateral force can be recorded as twisting of the cantilever [17]. AFM has therefore provided a means of measuring friction at the nanoscale. For instance, measurements using contact AFM have demonstrated atomic-scale stick-slip behavior, with the tip following the substrate lattice periodicity [18,19]. In addition, conductive AFM, which is operated in contact mode, can be used to measure the electric properties of the surface. In this measurement, a voltage difference is applied between a conductive tip and sample holder and then the current flowing between sample and tip can be measured.

1.1.2 Amplitude Modulation AFM

AM-AFM is one of two basic methods in dynamic AFM. In AM-AFM, the tip has intermittent contact with substrate. AM-AFM is widely used in nanoscale imaging, manipulation, spectroscopy, and lithography [8, 9, 20, 21]. It allows high resolution images of sample surfaces that are easily damaged, loosely held to their substrate, or difficult to image by other AFM techniques. In AM-AFM, the cantilever is excited at or near its resonant frequency by an actuator with fixed amplitude. When the tip is far from the sample, the oscillation amplitude is called the free amplitude A_0. As the oscillating tip is moved toward the surface, the tip oscillation is reduced due to energy loss caused by the tip interaction with the surface. During the operation of AM-AFM, the oscillation amplitude changes with the distance between tip and sample. Using a feedback loop, the tip oscillation amplitude is maintained constant, which ensures the distance between the tip and sample is the same during scanning. Thus, the topographic features of the sample

surface can be tracked. AM-AFM is preferred over contact mode AFM in some applications because of its minimal interaction with the sample [20, 22, 23]. In the operation of AM-AFM, the total amount of time that the tip interacts with the sample is reduced. In addition, since the applied force is vertical, interfacial shear forces between tip and substrate are significantly reduced. Thus, AM-AFM can reduce wear by eliminating shear stresses between tip and substrate and decreasing contact time, which are intrinsically present in contact mode AFM.

1.1.3 Frequency Modulation AFM

Similar to AM-AFM, in FM-AFM, an oscillating tip is used to image the sample topography. However, in FM-AFM, the cantilever is driven at its resonance frequency with a 90 degree phase shift, that is, the driving frequency is equivalent to the current resonance frequency. Thus, the frequency shift can be obtained and used as a direct measure of the tip-sample interaction. Most FM-AFM is operated in ultra-high vacuum (UHV) since the attractive force between the tip and sample is substantially weaker than the force used in AM-AFM or contact mode AFM. In FM-AFM, the tip is usually considered not to be in mechanical contact with the sample surface. However, this is not always true, since FM-AFM can also operate in the repulsive tip-sample interaction regime [12]. Recently, FM-AFM has been successfully implemented to achieve true atomic resolution of surface images [24, 25].

1.2 Nanoscale Wear

As AFM techniques advance from use in research laboratories to industrial applications, it has become more important to understand contact and relative motion between the AFM tip and surface. Many studies have been performed to investigate adhesion, friction, and wear at the nanoscale [26–29]. In this section, we will present a brief review of wear at the macroscale, and then introduce the applications and atomistic mechanisms of nanoscale wear.

1.2.1 A Brief Review of Wear at the Macroscale

Wear is the surface damage or removal of material from solid surfaces during sliding, rolling, or impact between two bodies [30]. It is unavoidable and can be desirable in some manufacturing processes such as polishing. However, in most areas of engineering and industry, wear is undesirable. Wear is complicated and can occur through mechanical processes or chemical reactions. Generally, there are seven major types of wear mechanisms, which are adhesive wear, abrasive wear, fatigue wear, impact by erosion and percussion, chemical wear, and electrical-arc-induced wear [30, 31]. In this section, we focus on adhesive wear and abrasive wear since they are the most important wear mechanisms during sliding in AFM [32–39].

Adhesive wear occurs when sliding surfaces under load adhere through solid phase welding of asperities [30]. The contacts are then sheared by sliding, which may result in detachment of a fragment from one surface and attachment to the other surface. Adhesive wear of dissimilar pairs is generally lower than that for similar pairs. Adhesive wear at macroscale can be described by Archard's law,

$$V_{adh} = k_{adh}\frac{Wx}{H} \tag{1.1}$$

where V_{adh} is adhesive wear volume, k_{adh} is a nondimensional adhesive wear coefficient, W is the applied load, x is sliding distance, and H is surface hardness. k_{adh} varies over a wide range from 10^{-2} to 10^{-8}, and depends on the materials and operating conditions [30].

Abrasive wear occurs when a hard rough surface slides across a softer surface leading to plastic deformation or fracture in the interface [30]. Ploughing, wedge formation, and cutting are three important deformation modes in abrasive wear. During ploughing, the material is shifted to the sides of the wear groove, resulting in the formation of ridge without removing material. In wedge formation, the material is displaced from a groove to the front rather than the sides. Wedge formation usually occurs when the ratio of the shear strength of the interface relative to the shear strength of the bulk is high. Cutting occurs when the material is removed from the surface in the form of discontinuous or ribbon-shaped debris. The degree of penetration and the interfacial shear strength of the interface are two controlling factors for the three modes of deformation in abrasive wear. Equation 1.2, which

has a similar form to Archard's equation for adhesive wear, can be applied to a wide range of abrasive wear.

$$V_{abr} = \frac{k_{abr} W x}{H} \tag{1.2}$$

where V_{abr} is abrasive wear volume, and k_{abr} is a nondimensional abrasive wear coefficient. The typical value of k_{abr} ranges from 10^{-6} to 10^{-1}, and is usually two to three orders of magnitude larger than k_{adh} [30]. It should be noted that both adhesive wear and abrasive wear have also been observed at the nanoscale [33, 34, 40, 41].

Wear processes are usually quantified by wear rate, which is defined as the volume or mass of material removed per unit time or per sliding distance. Wear is not an intrinsic property of the material but a system property. Therefore, wear rate depends on the material structures and properties as well as on surface preparation and operating conditions [30, 31]. The wear rate can also be reported in terms of a wear factor, defined as wear volume per unit applied normal load and per unit sliding distance (mm^3/Nm). Wear rate is a complex function of time rather than a constant. Wear rate may start low and rise later or vice versa, and the initial period is identified as the running-in wear stage. This running-in wear stage is followed by steady state wear, where the wear rate typically remains constant for a period of time. Then failure in the system may occur when the system exhibits a high wear rate. The beginning of steady state marks the start of the working life while the end of steady stage indicates the end of useful life [31].

1.2.2 Applications of Nanoscale Wear

There are many examples of Archard-like wear at the macroscale [42, 43], which is useful for characterizing wear and predicting the working life of engineering components. However, contacts at the macroscale consist of multi-asperity contacts [44], which means their behavior could be different from single-asperity contact, such as that in AFM measurement. With the development of AFM techniques, the durability and stability of the tip itself, as well as damage to the sample surface, have become more critical. It has been suggested that, in AFM images, most of the image artefacts are due to geometrical convolution of the surface structures with the tip shape [3], which can be affected by wear. For example, in the measurement of topography using contact mode AFM and AM-AFM, wear of the tip can result in the increase of tip radius, which can directly affect the attainable resolution of the topography image. Knowledge of the geometry and the physical characteristics of the tip as well as the nature of the interaction between tip and substrate are of critical importance for AFM measurement.

Nanoscale wear not only affects surface measurement, but also has an influence on the performance of nanoscale devices. Over the years, AFM has been extended to nanotechnology such as nanolithography, high-density data storage and nanoelectromechanical systems. In these applications, the wear of the tip is also a

serious limitation. It has been shown that, due to the strong adhesion between metal surfaces, nanoelectromechanical switches can prematurely fail through permanent adhesion of device components [45]. In tip-based nanomanufacturing and metrology, in which precision components play an important role, wear needs to be avoided for the process to be commercially possible. For nanoscale applications, wear occurs in different ways and can have various adverse effects on device performance. Thus, investigation of wear mechanisms at the nanoscale is necessary to enable the prediction of wear trends as well as to determine the optimum interface and operating conditions to minimize wear.

1.2.3 Atomistic Mechanisms of Nanoscale Wear

It is well known that nearly all surfaces are rough at the nanoscale [44], mechanical contact occurs mostly between the asperities of the surfaces, the smallest of which are nanoscale. Due to the high surface-to-volume ratio in nanoscale contacts, undesirable wear can be particularly critical, which can severely limit the durability and stability of nanoscale devices. At small scales, traditional methods and models are not always sufficient to characterize tribological behaviors [46]. Thus, experiments and simulations are needed to study wear mechanisms and then determine the optimum parameters. In experiment, transmission electron microscope (TEM) combined with AFM is often employed to study interface properties at the naoscale. For example, tip profiles measured with TEM can be used to estimate the volume loss over the course of a wear test in AFM [47–49]. In simulation, molecular dynamics (MD) is widely used to explore the mechanical, chemical, thermal and even electrical properties at the interface [16, 41, 50–52]. From simulations of nanoscale wear, the process of removing atoms from the surface can be observed directly.

Using both experimental and simulation techniques, some previous studies have shown that mechanical contacts at the nanoscale can obey the predictions of continuum contact mechanics [14, 53]. However, it is not reasonable to assume that continuum models should always apply at the nanoscale. In fact, most studies have shown that nanoscale contacts cannot be described by continuum contact models [54–56]. This suggests that nanoscale wear may not follow continuum laws as well [44, 49, 57].

Various mechanisms of wear at the nanoscale have been proposed. First, nanoscale wear can occur through fracture or plastic deformation, as is observed at the macroscale [33, 34, 36]. In this process, the two surfaces come into contact and then fracture of the material occurs during plowing or cutting. The local temperature at the contact could increase due to the mechanical deformation, which could further accelerate wear. Another observation from wear studies at the nanoscale is that wear may occur by the removal of one atom at a time from the surface [49, 57]. During atom-by-atom removal, two surfaces come into contact in quasi-static equilibrium, then an under-coordinated atom from one surface can form a bond with

one or more atoms from the counter surface. With sliding, the formed bond can break and thus the atom can transfer from one surface to another. This thermally activated process can be facilitated by compressive or shear stresses. In addition, amorphization of materials during sliding can facilitate the wear process at the nanoscale [58–60]. In this process, mechanical amorphization occurs to the surface material before it is removed. While wear has been analyzed in a wide variety of systems and conditions at the nanoscale, wear mechanisms are still not fully understood. In addition, although different mechanisms have been proposed, wear processes can be very complicated, in particular at extreme conditions that are often encountered by AFM tips. Thus, it is necessary to explore the applicability of competing wear mechanisms at different conditions.

1.3 Molecular Dynamics Simulation

Molecular dynamics (MD) simulation [61], which is based on Newton's second law, has been introduced to complement experimental studies of tribological behavior at the nanoscale [16]. This is because, in MD simulation, properties such as the force, displacement and velocity of each atom in the model system can be calculated. Thus, the collective behavior of the system can be analyzed with atomic detail. In addition, it is easier to control some variables in simulation than in experiment. For example, it is difficult to implement ultra high vacuum and extremely low temperature in experiment. However, these variables can be controlled easily in simulation, which can help us understand the mechanisms underlying physical and chemical phenomenon under specific conditions.

In MD simulation, the model setup is primarily determined by the geometry, the interaction potential among atoms and the thermostat applied to control the temperature of the model. Figure 1.3 shows a snapshot of an MD model of AFM. This model captures the apex of the AFM tip and its interaction with the substrate. The choice of interatomic potential is based on material. In addition, a thermostat, such as Nosé-Hoover or Langevin, is applied to some or all of the atoms in the model to dissipate the energy in the system. More details about MD simulation models are presented in the following chapters. All simulations reported in this thesis were performed using the large-scale atomic/molecular massively parallel simulator (LAMMPS) simulation software [62, 63].

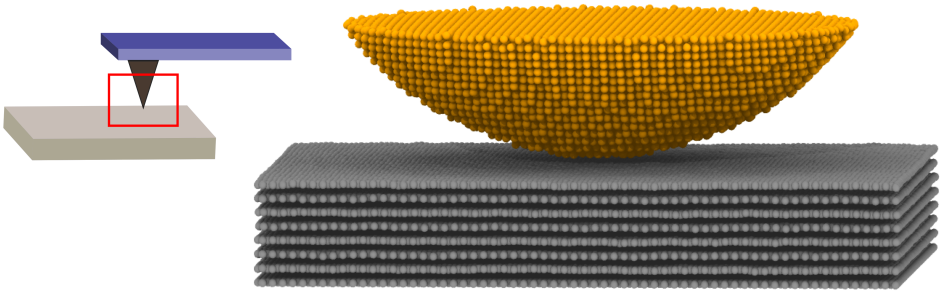

Figure 1.3: The interface formed between tip and substrate, identified by the red square in the left image, is modeled in MD. In a typical MD simulation of AFM, the hemispherical cap consisting of orange atoms represents the apex of a sharp AFM tip, and the block consisting of gray atoms represents the substrate.

1.4 Research Objectives

In this research, wear at the nanoscale was investigated using MD simulations of AFM. There were three major objectives of this research. First, using MD simulations, we sought to develop physically-realistic models of contact mode AFM and amplitude modulation AFM. The goal of this development was to perform simulations that are matched to AFM experiments in terms of the geometry of the tip apex, crystal orientation of the asperity in contact, and sliding distance, so that the simulations can provide mechanistic insights into AFM contact and sliding processes. Second, using these matched simulations, we aimed to study wear mechanisms at the nanoscale and to gain new fundamental understanding of nanoscale wear. Specifically, MD simulations provided ways to explore the effects of sliding distance, adhesive strength, load and tip roughness on wear. Third, by analyzing the effect of tip size on image resolution, we attempted to characterize the resolution loss in AFM measurement due to tip wear. In general, with a better understanding of tip-sample interactions and wear at the nanoscale, the durability and stability of nanoscale components can be improved, which in turn can reduce economic cost and environmental effects by predicting and controlling the failure of nanoscale systems.

1.5 Thesis Outline

This thesis consists of eight chapters. In Chapter 1 (this chapter), the background of AFM, nanoscale wear and MD simulations for studying these topics were introduced. The objectives of this research were also stated. From Chapter 2 to Chapter 5, we discuss sliding wear in contact AFM at different conditions. Specifically, we develop a sliding wear model and compare the results from simulation with experimentally-observed wear (Chapter 2), study the effects of adhesive strength, applied load and tip roughness on nanoscale wear (Chapters 3 and 4), and build a physically-realistic model of AFM tip to investigate the amorphization of tip material during sliding (Chapter 5). In Chapters 6 and 7, we present a noval MD simulation model of AM-AFM, which captures the tip oscillation and interaction with the sample. With this model, the effect of tip wear on image resolution is analyzed. Lastly, Chapter 8 contains a summary of this work, along with suggestions for future research.

Chapter 2

STRUCTURAL AND CHEMICAL EVOLUTION OF THE SLIDING INTERFACE

2.1 Introduction

It is well recognized that the shape and chemistry of the apex of an AFM tip greatly affect the tip-sample interactions and, therefore, all AFM-related measurements. Measurements involving sliding are further complicated by the fact that the tip can undergo physical and chemical changes through nanoscale wear processes. Consequently, characterization and prediction of the wear of the tip apex, both in terms of its shape and chemistry, as well as that of the contacting substrate are critical to enhancing our understanding of AFM-based measurements and methods. Most experimental studies of nanoscale wear occuring at the AFM tip-sample contact have focused on structural (i.e. shape) evolution due to sliding (see for example [47, 49, 57, 64, 65]). These experiments have been complemented by MD simulations that provide information about atomic bonding and rearrangement at sliding interfaces [16] but, like the corresponding AFM experiments, have been primarily focused on structural changes (see for example [41, 66, 67]). The important topic of chemical evolution of the tip due to sliding has remained relatively unexplored. Further, there have been no direct and quantitative comparisons of sliding-induced nanoscale wear predicted using MD and measured using AFM.

To address this, in this chapter, we performed MD simulations that complement AFM experiments of a silicon dioxide tip sliding against a copper substrate. Then, atom probe tomography (APT), which provided three-dimensional material structure and chemistry at near-atomic resolution [68], was used to investigate the chemical evolution of the AFM tip due to sliding. In this work, both AFM and APT experiments were performed by our collaborators from Iowa State University [69]. We compared model-predicted and experimentally-measured chemical and structural evolution, and showed that transitions between wear modes at the nanoscale were determined by both sliding distance and applied normal load.

2.2 Methods

The molecular dynamics simulation consists of a SiO_2 tip and a Cu substrate with a face centered cubic structure. The tip radius is 30 nm and the height of

the spherical cap is 2 nm. We believe that the model tip height of 2 nm, although only a small subset of the experimental tip, is sufficient to capture the wear mechanisms expected under the conditions explored here; this is indirectly supported by the observation that the atoms in the topmost 1/4th of the model tip exhibit negligible wear and experience only minimal interactions with the substrate. The dimensions of the Cu substrate are 60×40×2.2 nm in the x-, y- and z-directions, respectively. Periodic boundary conditions are applied in the x- and y- directions. The atoms of top three layers in the tip and the bottom two layers in the substrate are fixed, forming the z- boundary. The inter-atomic interactions within the tip are described by the Tersoff potential [70] with the parameters for SiO_2 reported by Adams et al. [71]. The Cu-Cu interactions are modeled using the Embedded Atomic Method [72] using the parameters given in recent work [73]. The long range interactions between tip and substrate atoms are described by the Lennard-Jones (LJ) potential. The LJ parameters of Cu-Si (ε_{Cu-Si} = 0.942 eV and σ_{Cu-Si} = 0.2217 nm) are the same as that reported by recent work [74]. The LJ parameters of Cu-O (ε_{Cu-O} = 0.043 eV and σ_{Cu-O} = 0.2644 nm) are obtained via the combination rules using previously-reported LJ parameters for Cu-Cu (ε_{Cu-Cu} = 0.415 eV and σ_{Cu-Cu} = 0.2277 nm) [75] and O-O (ε_{O} = 0.0045 eV and σ_{O} = 0.3010 nm) [76]. The Nosé-Hoover thermostat is applied to the free atoms in the system with a target temperature of 300 K. A constant normal load is maintained on the rigid top layers of the tip and the system is allowed to relax for 0.01 ns. Then the tip slides along the x-direction at a constant speed of 10 m/s through a distance of 30 nm.

2.3 Results and Discussion

We first characterize the structural evolution of the tip and substrate as functions of load where the simulations are performed at four different normal loads: 100, 400, 700 and 1000 nN. In all cases, substrate wear is quantified by the depth of the wear track and tip wear by the radius of tip's apex (where an increase in radius corresponds to more of the apex being worn away). Consistent with previous nanoscale wear studies [40, 57, 77–79], we find that both wear track depth and tip radius increase with load as shown in Fig. 2.1 and Fig. 2.2, respectively.

.

In addition to structural evolution, the chemical changes that occur during sliding wear can be observed from MD simulations, where each atom is modeled explicitly so the atomic composition and distribution are known; snapshots of the model tip after sliding are shown in Fig. 2.3. Qualitative analysis reveals similar trends in the simulation and atom probe tomography (APT) experiment, where the mass spectrum provides information about the chemical composition before and after sliding and the tip reconstruction provides information about the spatial distribution of atoms [69]. Specifically, in both cases there is a significant amount

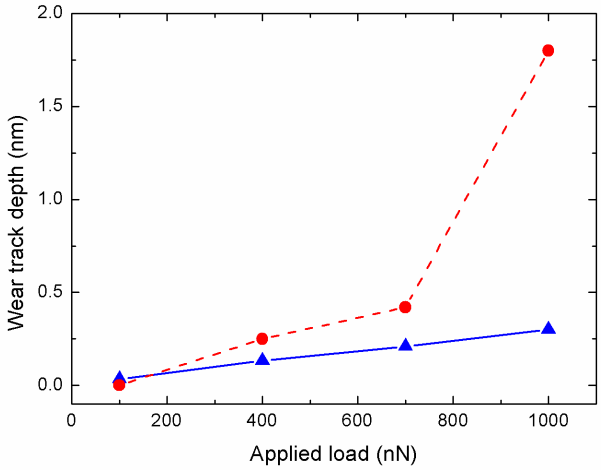

Figure 2.1: Wear track depth as a function of applied load: circles with a red dashed line represent experimentally-measured depth and triangles with a blue solid line represent simulation-calculated depth. All experimental results in this chapter are provided by the group led by Dr. Sriram Sundararajan.

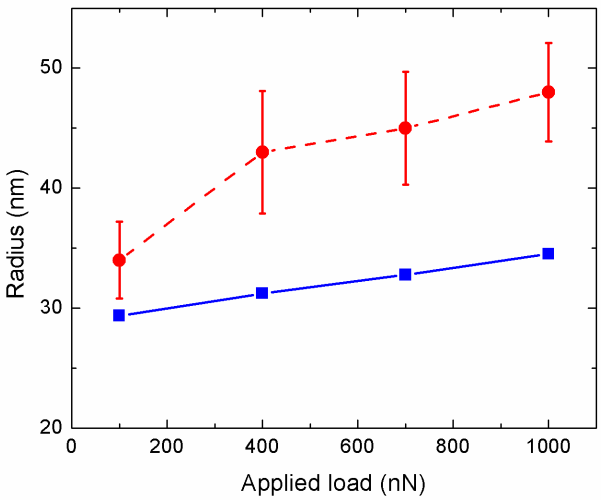

Figure 2.2: Radius of the tip as a function of applied load: circles with a red dashed line represent experimentally-measured tip radii and squares with a blue solid line represent simulation-calculated radii. Error bars on experimental data points represent 90% confidence intervals.

of Cu on the tip after sliding and there is more material transfer at the leading edge (in the sliding direction) of the tip.

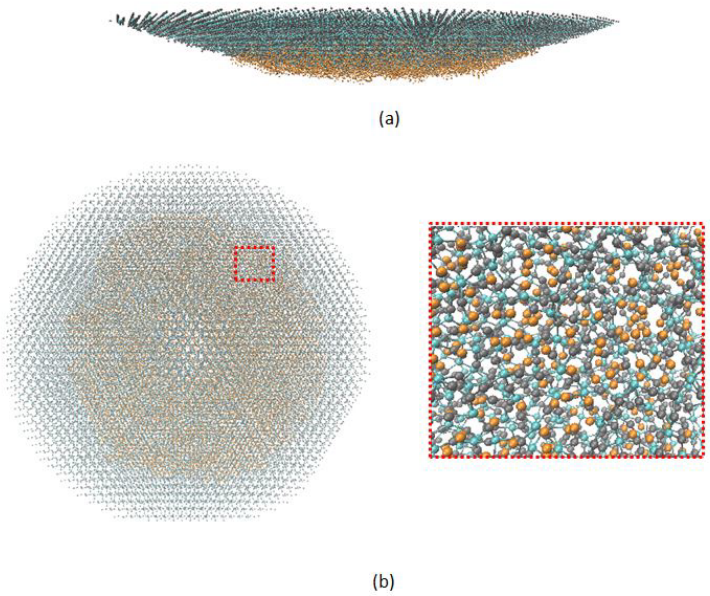

Figure 2.3: Side view (a) and bottom view (b) of the model tip after sliding. A close-up view of the tip structure is shown in (b). Copper atoms are shown in orange, silicon atoms in gray and oxygen atoms in cyan

Chemical evolution is characterized quantitatively in both experiments and simulations by the number of Cu atoms divided by the total number of atoms in the bottommost 2 nm of the tip. The results are shown in Fig. 2.4. In the experiments, the amount of Cu in the tip increases as the load increases from 100 to 400 nN, but then decreases as the load is further increased from 400 to 1000 nN. However, in the simulations, the amount of Cu transferred to the tip increases over the entire load range from 100 nN to 1000 nN. As discussed next, both the similarities and differences between the simulation and experiment provide insight into the wear mechanisms.

First, we consider our results in the context of classic wear theories where the wear rate is a function of the material volume lost. The wear volume of the substrate is calculated directly from the wear track depth (Fig. 2.1) as:

$$V_{substrate} = [R_0^2 \arcsin(w/2R_0) - (1/2)w(R_0 - d)]s \tag{2.1}$$

where w is the width of the wear track, R_0 is the tip radius before wear, d is the depth of wear track,s is the sliding distance in simulation and the scan length in experiment. Using this formulation, the substrate wear rate for the simulation is

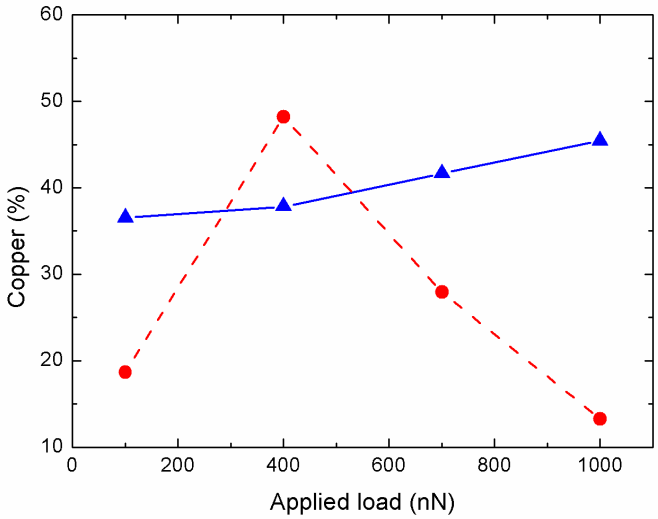

Figure 2.4: The percent of Cu atoms in the tip as a function of applied load: circles with a red dashed line represent experimentally-measured results and triangles with a blue solid line represent simulation-calculated data.

found to be 1.8×10^{-3} $mm^3/(N \cdot m)$ and for the experiment to be 4.32×10^{-5} $mm^3/(N \cdot m)$ from 100 to 700 nN and 5.17×10^{-4} $mm^3/(N \cdot m)$ from 700 to 1000 nN. The wear rates calculated from the model and experimental substrate wear track cannot be compared directly because they are calculated from different sliding patterns. Specifically, in an experiment, the tip moves back and forth on the substrate and the wear track depth that is measured after a total sliding distance of 0.24 mm is the result of many cycles of repeated sliding. The timescale limitation of MD simulation precludes reproducing this motion pattern. Instead, the tip moves only forward and the depth is reported after a single pass of 30 nm sliding.

Wear rate can also be characterized in terms of the change of the tip radius. If we assume the apex of the tip is initially a perfect hemisphere, the tip volume can be expressed as

$$V_{tip} = \int_0^R r^2 dr \int_0^{2\pi} d\varphi \int_{\pi-\theta_0}^{\pi} \sin\theta d\theta \tag{2.2}$$

where (r, θ, ϕ) represents spherical coordinates, R is the radius of the worn tip (Fig. 2.2) and $\theta_0 = \arccos(29/30)$ is the circumferential angle of the worn tip. The wear volume calculated from equation (2) is verified by integrating the simulation wear volume over a 3-dimensional domain. Although uncertainly in the APT measurements precludes making this comparison for the experiments, we anticipate the error

is systematic (similar at all loads) and so does not affect the calculated wear rate significantly. We find the tip wear rate is $2.19 \times 10^{-5}\ mm^3/(N \cdot m)$ for the experiment and $3.28 \times 10^{-2}\ mm^3/(N \cdot m)$ for the simulation. Thus the tip wear rates differs by three orders of the magnitude. The two most significant differences between the simulation and experiment are the sliding velocity and the sliding distance. For solid-solid contact, wear rates have been found to be comparable in high and low sliding velocity regimes [80]. Therefore, the observed wear rate discrepancy is likely attributable to the sliding distance [81]: 0.24 mm in the experiment but 30 nm in the simulation. Wear rates can decrease during continued sliding because the tip (a) becomes blunter as it slides [47] which results in increased contact area and in turn decreased contact pressure, or (b) can become harder due to microstructural changes that occurs during sliding [82]. We estimate the contact pressure using the Derjaguin-Muller-Toporov (DMT) contact model [83] to be between 5.7 and 6.2 GPa in the simulation and between 4.8 and 5.2 GPa in the experiment. The simulation contact pressure is consistently higher than that in the experiment because the model radius is smaller after wear.

It has been proposed that classical theories may not be applicable to nanoscale wear because, for example, wear may not increase linearly with load as in Fig. 2.1. An alternative model has been proposed based on transition state theory (TST) to address this issue [49, 57, 81, 84, 85]. This model is based on the assumption that wear is gradual and occurs though atom-by-atom, stress-assisted bond formation and breaking. According to this theory, the fundamental rate of atom loss due to wear can be expressed as

$$k_{atom-loss} = k_0 exp\left(-\frac{\Delta E_{act}}{k_B T}\right) \tag{2.3}$$

where k_0, is the attempt frequency, ΔE_{act} is the activation energy, k_B is the Boltzmann constant and T is the absolute temperature [86]. It has been argued that the activation barrier can be reduced through bond stretching due to stress τ, where $\tau = F_{applied}/A_{contact}$ if adhesion is neglected. Thus, the activation barrier can be simplified as $\Delta E_{act} = \Delta G_{act} - \tau V_{act}$ where V_{act} has units of volume and is referred as the activation volume and ΔG_{act} is the stress-free activation barrier. Fitting our data to this expression leads to ΔG_{act}=0.39 eV and V_{act}=1.5 Å^3 for the simulations and ΔG_{act}=1.33 eV and V_{act}=13.3 Å^3 for the experiments. The experimental and simulation data fit follow the trend predicted by TST reasonably well; the average relative error in the wear volume prediction is found to be 6.3% is the simulation and 33.5% in the experiment. In both cases, the fit parameters are comparable to the range of values reported previously, ΔG_{act}=0.34-1eV and V_{act}=6.7-340 $\mathring{A}^3$ (obtained via fit to experiment) [86].

However, we are hesitant to extract too much meaning from these results

since the TST-based wear models are based on the assumption that wear is a gradual atom-by-atom process which may not be the case for the high loads applied in this study (previous experiments fit to the TST model were performed at the 0 to 100nN load range). Indeed, Fig. 2.4 shows that more than 10% of the bottom 2 nm of the tip at any load; this translates to thousands of Cu atoms being removed from the substrate. Particularly in the case of the simulations, this means wear is occurring very rapidly, i.e. not through an atom-by-atom process. We further analyze the applicability of this theory to our system by adapting the model to describe the transfer of Cu atoms from substrate to tip. Fitting our data to the adapted model yields negative values of the activation volume V_{act}, which is unphysical, and supports the suggestion that the observed wear may be too severe to be described by TST-based theories.

Lastly, we consider our results in terms of possible wear modes: adhesive and abrasive. Adhesive wear occurs when the pressure between sliding surfaces is high enough to cause plastic deformation and results in welding between the contacting asperities. This kind of wear results in significant material transfer. Abrasive wear occurs when a hard protuberance or particle indents and cuts a groove in the softer material [87]. This type of wear is associated with mechanical deformation and cutting. Although adhesive and abrasive wear were originally understood in terms of their role in macroscale wear, they are very relevant to nanoscale wear as well [32]. The atom-scale data available from APT and simulations provide a unique opportunity to observe transitions between these two mechanisms in nanoscale sliding contact.

Fig. 2.4 shows that, in the experiment, the amount of Cu transferred to the sliding tip increases with load up to 400 nN load, after which it decreases. The data suggests that there may be a transition from an adhesive mode (where the amount of Cu increases with normal load) to a mode where abrasive mechanism begins to dominate, leading to less Cu being transferred to the tip. This idea is supported by examining the degree of penetration parameter (D_p), which was introduced as a severity index of sliding [88]. D_p is defined as the ratio of the groove depth to the radius of contact and can be calculated as

$$D_p = R\left(\frac{\pi H_\nu}{2W}\right)^{1/2} - \left(\frac{\pi H_\nu}{2W}R^2 - 1\right)^{1/2} \tag{2.4}$$

where R is the radius of the sliding tip, W is the normal load, and H_ν is the hardness of the substrate (we use 4 GPa). D_p can be used to establish the likelihood of the wear mode during sliding. Examination of sliding contacts showed that low values of D_p (< 0.06) for a material pair correspond to ploughing while increasing values correspond to other modes of abrasion such as shear tongue formation ($0.06 < D_p < 0.09$) and wedge formation and cutting ($D_p > 0.09$) [82]. Using the experimentally-measured data (Fig. 2.4), we find that D_p increases with load

such that the wear mechanisms in our sliding experiments become predominantly abrasive (wedge formation and cutting) at normal loads of 400 nN and higher. With an increased propensity to generate wedges and cutting debris, the amount of Cu transferred to the tip via adhesive mechanism is reduced, as borne out in our APT data.

Recall from Fig. 2.4 that the simulations predict the amount of Cu transferred to the tip will increase monotonically with load. This indicates that there is no transition between wear modes. We can consider which mode is dominant by evaluating the normal and shear forces that occur during the wear processes. It has been proposed that the atoms involved in wear processes may adhere to a probe tip if the normal forces are more significant than the shear forces; alternatively, if shear forces are dominant, the wear can be regarded as abrasive [32]. In our simulations, we find that the normal force on the tip is larger than the shear force, which suggests that the adhesive wear mechanism dominates at all loads.

2.4 Summary

In summary, MD simulations were used to characterize nanoscale wear of a sliding AFM tip in terms of wear track depth as well as change in tip radius and chemical composition. The results were compared with experimental measurements. We found that substrate wear increases with load in both simulations and experiments and that the wear rates calculated using a classical wear model cannot be directly compared due to different sliding patterns. Tip wear, characterized by the radius of the tip apex, increases with load as well, but the rate of increase is much larger in the simulation than that in the experiment. This discrepancy was attributed to the significant difference between sliding distance in the experiment and simulation and the effect of that distance on tip shape. We also considered the wear trends we observed in terms of a model based on transition state theory, but found that the conditions used in this study cause wear that is not gradual and so does not meet the criteria for this theory. Finally, we evaluated the wear modes present during sliding. Comparison of the normal and shear forces on the tip in the simulation indicates that the model experiences adhesive wear at any load. By the comparison between simulations and experiments, our study has shown that nanoscale wear can occur through both adhesion and abrasion, and that the dominant mode is determined by both sliding distance and load. Material transfer from the substrate to the tip was observed during both wear modes, with the amount of transfer being higher when adhesion is the dominant mode.

Chapter 3

THE EFFECTS OF ADHESION AND LOAD ON NANOSCALE WEAR

3.1 Introduction

As suggested in Chapter 2, the two primary mechanisms through which nanoscale wear occurs are abrasion and adhesion [32–39]. The key features of abrasive wear are cutting or plowing of the softer surface by the harder counterface. Typical observations of abrasive wear at the nanoscale are broken bonds and displaced material. Adhesive wear evolves through the formation of adhesive junctions, their growth, and fracture. The transfer of material, specifically atoms transferred due to bonds breaking and reforming at the nanoscale, between the contacting solid surfaces, is regarded as the characteristic feature of this mechanism of wear [89]. However,material transfer has been used as a means of quantifying wear in general [69, 90–97]. It is likely that both adhesion and abrasion contribute to material transfer, with one or the other mechanism being dominant, depending on condition such as load [69].

Previous AFM-based studies have shown that load and adhesive strength significantly affect nanoscale wear [37, 47, 48, 78, 79, 98–101]. However, it is difficult to quantify this relationship since adhesive strength cannot be easily controlled during the wear process. Further, AFM cannot be used to investigate wear in terms of material transfer. To address the latter issue, APT has been used to characterize the composition of the AFM tip before and after sliding [69, 102, 103]. APT, however, does not provide a means of characterizing adhesive strength. Thus, previous experimental efforts have not directly shown how the adhesive strength of an interface affects material transfer.

There are fewer MD simulations specifically focused on the role of adhesive strength on nanoscale wear. Simulations of tip loading and unloading showed that large adhesive strength led to substantial plastic deformation on separation and some material transfer, while small adhesive strength resulted in separation of the materials at a critical force without material transfer or plastic deformation [104, 105]. Simulations of sliding predicted that wear increased with adhesive strength. In one case, a simulation of sliding on graphene showed that the rate of graphene bonds broken and the shear experienced by the tip increased as the adhesive strength

between graphene and substrate was increased [34]. Also, simulations of two contacting, sliding asperities revealed that increasing adhesive strength resulted in more bonding between the asperities along with more heat generation and an increase of temperature in the contact area [41].

Material transfer wear has also been studied theoretically [90, 92, 93, 96]. It was found that the transfer tendency can be predicted by comparing the cohesive strengths of the sliding components [90]. Also a lump growth model was developed based on transfer mechanisms observed at the macroscale and it was predicted that lump growth can be decreased by higher surface hardness of the workpiece, lower roughness of the tool surface, or lower shear strength of the interface [92, 93, 96].

In this chapter, we quantitatively characterized the effect of adhesive strength on material transfer, and the dependence of that effect on load and sliding. We used MD simulations of a model SiO_2 AFM tip sliding on a Cu substrate with artificially modulated adhesive interactions between the two. Predicted work of adhesion was correlated to material transfer before and after sliding at normal loads between 100 and 1000 nN. The results indicated that there was a work of adhesion- and load-dependent threshold below which no material transfer would occur. Above that threshold, the severity of the material transfer wear increased with adhesive strength and load. In addition, the relative contributions of adhesion and abrasion to observed wear were analyzed in terms of the ratio of number of atoms transferred at 0 nm to that at 30 nm. The findings shed light on the complex process by which adhesive and abrasive mechanisms determine the load-dependent wear of nanoscale sliding contacts.

3.2 Methods

The model in this project is similar to the one we described in Chapter 2. Similarly, the Lennard-Jones (LJ) potential is used to model the interactions between tip and substrate atoms:

$$E_{ij} = 4\varepsilon \left[\left(\frac{\sigma}{r_{ij}} \right)^{12} - \left(\frac{\sigma}{r_{ij}} \right)^{6} \right] \tag{3.1}$$

where ε is the LJ interaction strength parameter with units of energy, σ is the zero-crossing distance with units of length, and r_{ij} is the distance between a given substrate atom i and a given tip atom j. The LJ parameters for Cu-Si ($\varepsilon_{Cu-Si} = 0.942$ eV and $\sigma_{Cu-Si} = 0.2217$ nm) are the same as those reported in recent work [74]. The LJ parameters for Cu-O ($\varepsilon_{Cu-O} = 0.043$ eV and $\sigma_{Cu-O} = 0.2644$ nm) are obtained via the combination rule [74] using previously-reported LJ parameters for Cu-Cu ($\varepsilon_{Cu-Cu} = 0.415$ eV and $\sigma_{Cu-Cu} = 0.2277$ nm) [75] and O-O ($\varepsilon_{O-O} = 0.0045$ eV and $\sigma_{O-O} = 0.3010$ nm) [76]. To simulate different adhesive strengths, the magnitudes of ε_{Cu-Si} and ε_{Cu-O} are artificially changed, while the parameters σ_{Cu-Si}

Table 3.1: Summary of the Lennard-Jones potential parameters used to vary the adhesive strength of the interface.

	LJ1	LJ2	LJ3	LJ4
ε_{Cu-Si} (eV)	0.314	0.6	0.942	1.256
ε_{Cu-O} (eV)	0.014	0.025	0.043	0.057

and σ_{Cu-O} are held constant as 0.2217 nm and 0.2644 nm, respectively; the tip-substrate interaction parameters studied are summarized in Table 1. The ratio of ε_{Cu-Si} to ε_{Cu-O} is approximately constant across the four groups of LJ potential parameters. Changing the interaction strength parameter of the LJ potential has been successfully employed in the previous MD simulations to modulate the adhesive strength between two surfaces [34, 41, 106]. The adhesive strength between the tip and substrate could be affected by the tip termination, size or shape. However, to exclude these effects, the same tip is employed in all simulations and adhesive strength is changed using LJ parameters only. All simulations are performed using LAMMPS simulation software [62, 63] with a time step of 1 fs.

To assess the adhesive strength of the interfaces with different LJ interaction strengths, we calculate the ideal work of adhesion W as:

$$W = \frac{E_1 + E_2 - E_{12}}{A_c} \tag{3.2}$$

where A_c is the contact area, E_{12} is the total energy of the interface (consisting of the tip and substrate) at equilibrium, and E_1 and E_2 are the total energies of the tip and the substrate at equilibrium, respectively [107–109]. E_1 and E_2 are calculated from energy minimization after the tip and substrate are relaxed separately. To obtain E_{12}, the tip is placed 0.3 nm above the substrate surface and then the system is relaxed without applied load for 0.05 ns to allow the system to reach a stable potential energy. Then the system energy is minimized to calculate E_{12}. Note that the distance between the tip and substrate is allowed to change freely during the relaxation process, so the initial distance does not affect the calculated energy. The area A_c is calculated from the positions of contacting atoms, where tip contact atoms are identified as those within 0.3 nm of a substrate atom; 0.3 nm is chosen here because it is slightly larger than the equilibrium distance between tip atom and substrate atom. Two different cross sections are used to estimate the diameter of the circle formed by the contacting atoms from which we can calculate contact area. These calculations are performed with the tip-substrate geometry since that is the configuration used in the sliding wear simulations. However, we find that calculations performed with a slab-on-slab geometry yield qualitatively and quantitatively comparable results.

After determining the work of adhesion for each case, MD simulations are conducted with each model to investigate the wear behavior at various loads and adhesive strengths. A constant normal load (100, 400, 700 or 1000 nN) is maintained on the rigid top layers of the tip and the system is allowed to relax for 0.01 ns. This method of applying load directly to the atoms in the rigid top layers of the tip makes it possible to isolate the effect of load from that of adhesive strength. Then the tip slides along the x-direction at a constant speed of 10 $m\,s^{-1}$ through a distance of 30 nm. This speed, although fast compared to an AFM experiment, is necessitated by the timescale limitation of MD simulation, particularly for the relatively large number of atoms in this model. The sliding distance is determined based on the observation that 30nm is sufficiently beyond the point at which the system exhibits linearly increasing wear (shown later). The Nosé-Hoover thermostat is applied to the free atoms in the system with a target temperature of 300 K. It should be noted that whether or not the thermostat is applied to the atoms near the contact has little effect on material transfer results. The kinetic energy bias of the tip (due to the constant lateral speed) can be ignored in our system since the number of atoms in the tip is very small compared to that in the substrate. To confirm this, we calculate the temperature of the system after removing the kinetic energy bias and find it is only 1 K lower than when the bias is included, which indicates that this bias insignificantly affects the energetics of the system.

The material transfer before and after sliding are characterized in terms of the number of Cu atoms attached to the tip after it is separated from the substrate. The tip is displaced in the z-direction with a velocity of 50 m/s and the number of atoms transferred between tip and substrate is determined when they are completely separated. Simulations with velocities from 5 m/s to 100 m/s reveal that the number of atoms transferred decreases somewhat with velocity, but that this effect is small compared to that of load or adhesive strength.

3.3 Results and Discussion

The work of adhesion W is calculated for each group of LJ parameters to quantify the adhesive strength. The work of adhesion with respect to ε_{Cu-Si} and ε_{Cu-O} is shown in Figure 3.1. It can be seen that W increases monotonically with interaction strength. The magnitudes of work of adhesion computed here are comparable to values obtained for the same material system from first-principles calculations [109] and from experiment using an indentation technique [110].

Figure 3.2 is a snapshot of the simulation during the process of pulling the tip away from the substrate before sliding. It can be seen that some atoms are transferred from the substrate to the tip but none are transferred from tip to substrate. This is observed at all adhesive strengths and all loads before and after sliding; the behavior is reasonable since the tip is harder than the substrate and this unidirectional material transfer has been reported previously [92, 96].

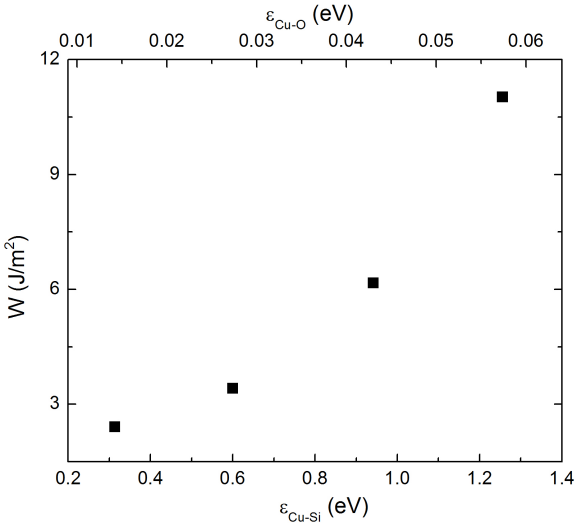

Figure 3.1: The work of adhesion as a function of Cu-Si (ε_{Cu-Si} on the lower x-axis) and Cu-O (ε_{Cu-O} on the upper x-axis) interaction strength.

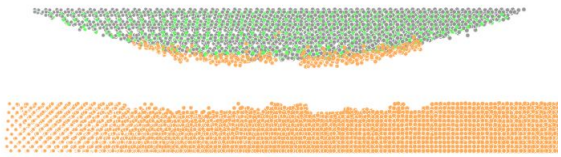

Figure 3.2: Snapshot of the tip being pulled away from the substrate for a simulation without sliding where the load is 100 nN and work of adhesion is $W = 6.16 J/m^2$. Color scheme same as in Figure

The increase of material transfer with sliding distance is shown in Figure 3.3. To confirm observed trends are statistically significant, we perform pull-off simulations four times for all loads with different seed numbers (i.e. random numbers used to generate an ensemble of velocities at the start of the simulation) and find the variation from simulation to simulation is very small, with error bars being smaller than the symbols in Figure 3.3. This figure indicates that the number of atoms transferred increases with sliding distance and the rate of increase is nearly constant after a distance of approximately 10 nm. Note that we do not identify this slope as a steady state wear rate since material transfer is not expected to continue increasing linearly (unlike, for example, wear volume). The increased wear with sliding can be qualitatively correlated to contact area. Snapshots of the contact area, identified as the area of the model's smallest x-y cross-section, before sliding and after sliding as shown in Figures 3.4(a) and (b). These images reveal that, during sliding, substrate atoms both accumulate in the tip-substrate interface and adhere to the perimeter of the contact.

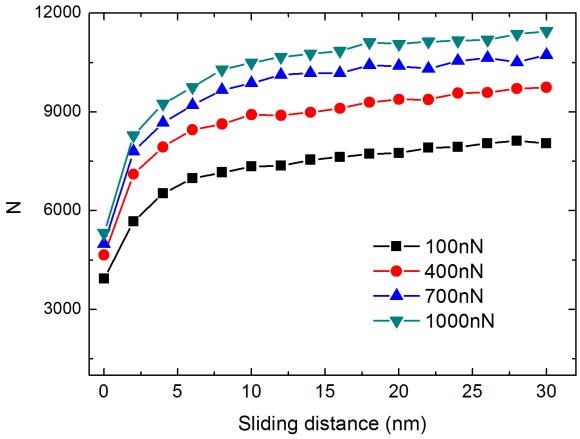

Figure 3.3: Number of atoms transferred from substrate to tip, N increases with sliding distance at different loads for $W = 6.16 J/m^2$.

Figure 3.3 also shows that, at different sliding distances, material transfer increases with load. The number of atoms transferred before sliding and after 30 nm of sliding are plotted for different work of adhesion values in Figure 3.5. First, we observe that the number of atoms transferred increases approximately linearly with applied load at a given work of adhesion before and after sliding. This is consistent with previous simulations of sliding wear, which revealed that the material loss rate during sliding is linearly proportional to applied load [53]. The trend can be understood by the fact that contact area increases with load such that there are more tip atoms in contact with the substrate. Examples of contact areas that increase with load are shown in Figures 3.4(c) and (d).

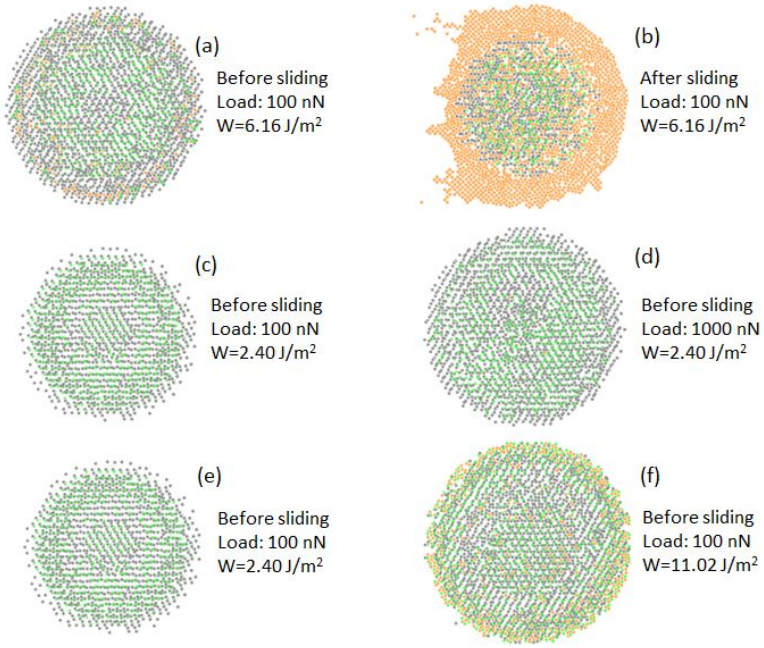

Figure 3.4: Snapshots of the contact area under various conditions. Color scheme same as in Figure

Figure 3.5 also shows that, for each load, the number of atoms transferred increases with work of adhesion, W. This is reasonable because, with stronger adhesive strength, the contact area is larger (as shown in Figures 3.4(e) and (f)) and the stronger interaction between tip and substrate will increase the likelihood of atoms being pulled away from the substrate to adhere to the tip.

We observe from Figure 3.5 that, for some cases, there is no material transfer if the work of adhesion is small enough. Without sliding, there is no material transfer at any load for the smallest work of adhesion $W = 2.4J/m^2$; similar observations were made in previous MD-based studies of indentation-induced wear [104, 105]. There is also one sliding case with no material transfer ($W = 2.4J/m^2$, 100 nN). Previous work showed that there is a load threshold below which no measurable wear occurs [111]. Here, the observations from Figure 3.5 suggest the threshold for material transfer wear is dependent on load, adhesive strength and sliding. This is illustrated in Figure 3.6. Using the data points from simulation as guides, we can approximate the adhesive strength- and load-dependent thresholds for material transfer before and after sliding. In Figure 3.6, thresholds drawn as solid lines are those bound by simulation data and those drawn as dashed lines are estimations based on expected limiting behavior. More data near these lines would enable the threshold conditions to be further refined.

Adhesion and abrasion are two major mechanisms through which nanoscale

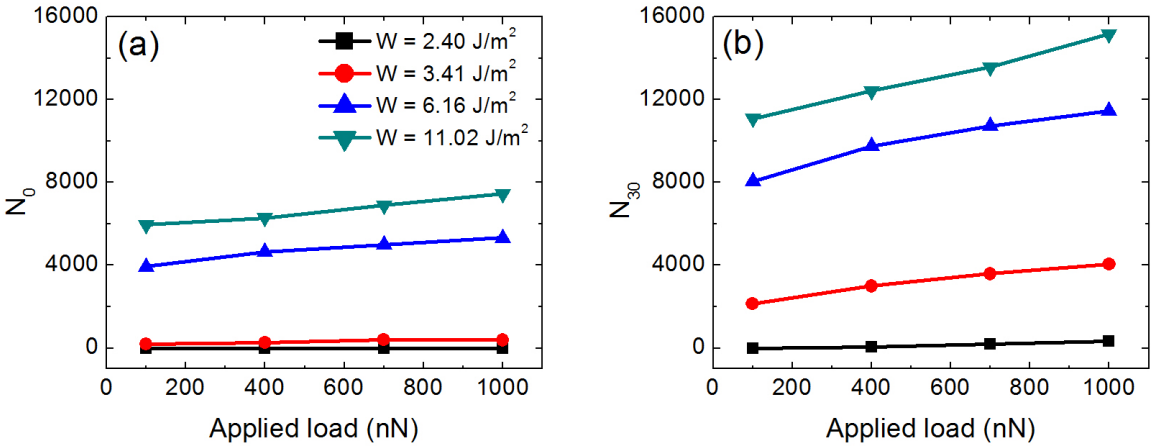

Figure 3.5: The number of Cu atoms on the tip as a function of applied load (a) before sliding, N_0, and (b) after sliding 30 nm, N_{30}.

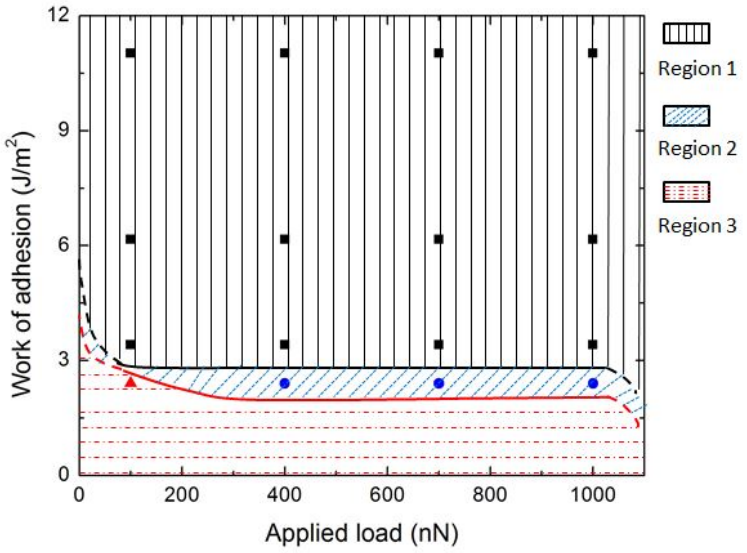

Figure 3.6: Map of material transfer where black squares represent load and work of adhesion combinations at which material transfer occurs before or after sliding, blue circles represent combinations at which material transfer occurs after sliding but does not occur before sliding, and the red triangles represent combinations at which material transfer does not occur before or after sliding. The lines are approximations of the adhesive strength- and load-dependent thresholds for material transfer.

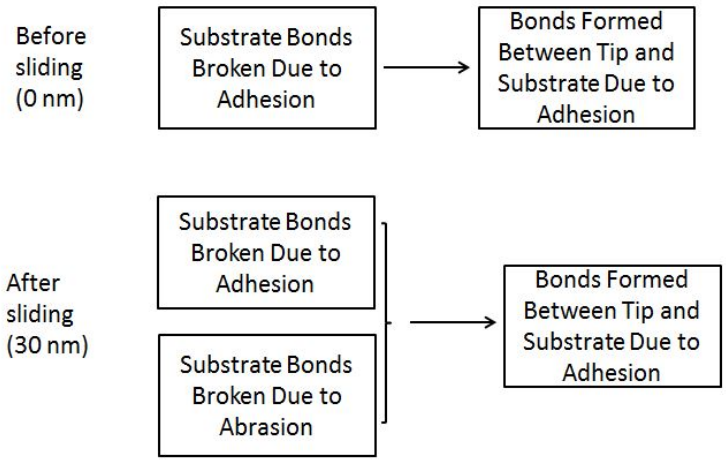

Figure 3.7: Schematic illustration of factors contributing to material transfer

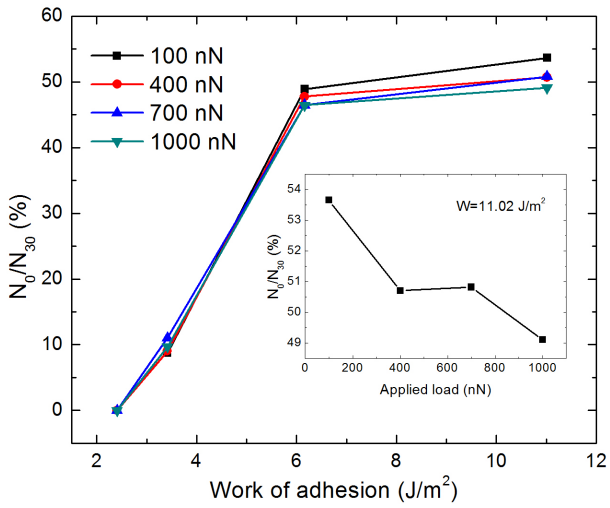

Figure 3.8: The ratio of the number of atoms transferred at 0 nm to that at 30 nm as a function of work of adhesion for each load. Inset shows this ratio as a function of load at $W = 11.02\ J/m^2$

wear occurs [30]. Adhesion involves the detachment of a fragment from one surface and attachment to the other surface when two surfaces are in contact. Thus, the transfer of material is regarded as the characteristic feature of adhesive wear. During abrasion, material removal from a surface can occur by several deformation modes such as ploughing (ridge formation), wedge formation and cutting. The roles of adhesion and abrasion in material transfer are illustrated schematically in Figure 3.7. Three processes are generally involved in material transfer: substrate bonds broken due to abrasion, substrate bonds broken due to adhesion, and bonds formed between the tip and substrate due to adhesion. At 0 nm, before sliding, substrate bonds break and new bonds form between the tip and substrate due to adhesion only. At 30 nm, however, it is also possible for substrate bonds to break due to abrasion during the sliding process which means that there are more atoms available to bond with the tip due to adhesion.

Based on this observation, the number of atoms transferred at 30 nm can be attributed to adhesion and abrasion, while the number of atoms transferred at 0 nm can only be attributed to adhesion. Using this assumption, we can analyze the relative contributions of adhesion and abrasion in material transfer by comparing the number of atoms transferred at 0 nm with the number of atoms transferred at 30 nm, (i.e. N_0/N_{30}), where increasing N_0/N_{30} indicates more adhesion dominated wear. The result is shown in Figure 3.8. It can be seen that N_0/N_{30} increases with work of adhesion for all loads. This is reasonable since adhesion can play a more important role in material transfer when work of adhesion is larger. In addition, it can also be observed from the inset of Figure 3.8 that, for the largest work of adhesion, N_0/N_{30} decreases with load. This observation indicates that the role of abrasion becomes more important with increasing load. This is consistent with the observation that higher loads correspond to larger penetration depths which in turn facilitates the formation of a wedge in front of the tip or a ridge on the sides of the tip, both of which are characteristics of abrasive wear [30].

3.4 Summary

In summary, MD simulation was used to investigate the effect of adhesive strength and load on material transfer before and after sliding, where adhesive strength was quantified by the work of adhesion. We observed that the number of atoms transferred from substrate to tip increased with load, work of adhesion and sliding. These trends were correlated qualitatively to contact area. We also identified a condition-dependent threshold below which no material transfer occurs. Work of adhesion appears to be the most significant parameter in determining this threshold. However, at lower adhesive strengths, the load can determine the onset of material transfer. The wear threshold is also dependent on if the tip is sliding. Above this wear threshold, we used the observation that there is no abrasion without sliding to analyze the relative contributions of adhesion and abrasion to wear in terms of

the ratio of the number of atoms transferred at 0 nm to that at 30 nm. This ratio was found to increase with work of adhesion and decrease with load for large adhesion. The trends indicate that adhesive wear will play a more significant role in the wear process with increasing adhesive strength and decreasing load. Although this behavior is expected for wear processes in general, here we have characterized it quantitatively, specifically for material transfer. In summary, this research reveals that both adhesion and abrasion contribute to the material transfer during nanoscale wear and both wear mechanisms are affected by the work of adhesion and applied load.

Chapter 4

THE EFFECT OF ROUGHNESS ON NANOSCALE WEAR

4.1 Introduction

At the nanoscale, the AFM tip is not ideally smooth, and the roughness can affect the nature of the contact between tip and substrate [4, 44, 54–57, 112–114]. These contact features in turn affect nanoscale wear. Thus, a fundamental understanding of the effect of nanoscale roughness on surface wear is critical to enable reliable and precise measurements at the nanoscale, as well as tip-based nanomanufacturing methods.

Previous studies have shown that roughness significantly affects the adhesive strength of nanoscale contacts. Such studies showed that adhesive strength decreases with increasing nanoscale roughness, due to the reduction in real contact area between the two surfaces [115–118]. It has also been found that adhesion can be minimized at an optimum surface roughness and that roughness can be tuned by the size or density of asperities on the surface [119–123].

As suggested in Chapter 3, adhesive strength plays a significant role in determining wear in nanoscale contacts. Studies have reported that there will be a larger number of atoms transferred from one surface to another when there are more interfacial bonding bridges formed between surfaces [124] or when the adhesive strength is stronger [41, 104, 105, 125]. This was corroborated by studies that showed adhesion and wear decreased or increased together when different tips were used in AFM measurements [99, 100]. However, although nanoscale wear increases with adhesive strength and roughness decreases adhesive strength for small surface roughnesses, wear has been found to increase with roughness [126]. This observation suggests that nanoscale wear is not solely determined by adhesion and, like at the macroscale, both adhesion and abrasion contribute, and both are affected by roughness. Although this is a reasonable assumption, it has not been systematically studied.

To address this, in this chapter, we used MD simulation to characterize the wear between a model Si AFM tip and a Cu substrate using tips with different degrees of roughness at different loads. Then we analyzed the relationship between the tip roughness and wear in terms of adhesion and abrasion, which were assumed

to be the two major wear mechanisms during nanoscale dry sliding [32–34, 125]. Macroscale wear theories that relate adhesive and abrasive wear to sliding distance, load and roughness were used to isolate the contributions of the two wear modes. To apply these expressions to describe nanoscale wear, we introduced an additional term to capture the effect of adhesion on contact and redefined the wear coefficients in terms of atom-atom interaction energy. The resulting expression makes it possible to predict the effect of load and roughness on nanoscale wear and to determine the roughness of scanning probe tips that will minimize that wear.

4.2 Methods

The MD model consists of a Si tip, which has a diamond crystal structure, and a face-centered-cubic Cu (100) surface, as shown in Figure 4.1. To model rough tips, we superpose a spherical cap, which has a radius of 29 nm and a height of 3 nm, with a cosine wave along the x-direction and another cosine wave along the y- direction. We artificially adjust the amplitude of the cosine wave to obtain tips with different roughnesses. The inset of Figure 4.1 shows a schematic of the model rough tip geometry. The amplitude of the cosine wave is varied from 0.01 nm to 1 nm while the wavelength is kept at 4 nm. Seven different tips are obtained by setting the amplitude of the cosine wave to 0.01, 0.2, 0.35, 0.5, 0.6, 0.8 and 1 nm, which correspond to root mean square roughnesses R_q of 0.184, 0.214, 0.271, 0.352, 0.409, 0.526 and 0.638 nm, respectively. The substrate lattice orientations along the x, y and z directions are [100],[010] and [001], respectively. The dimensions of the Cu substrate are 60×40×2.2 nm in the x-, y- and z-directions, respectively. Periodic boundary conditions are applied in the x- and y-directions. The atoms in the top three layers of the tip and the bottom two layers of the substrate are fixed. All inter-atomic interactions within the model are described by the Modified Embedded-Atom Method [127] with reported parameters in [128]. The Nosé-Hoover thermostat is applied to the free atoms in the system with a target temperature of 300 K.

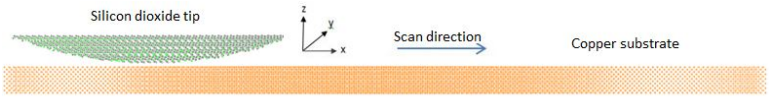

Figure 4.1: Snapshot of the simulation system consisting of a Si tip and Cu substrate during sliding. The inset shows the geometry of a rough tip created by superposing a spherical cap with a cosine wave. Cu atoms are shown in orange, Si atoms in gray.

Sliding simulations are conducted with each model tip to investigate the effect of tip roughness on wear. A constant normal load W (10, 25, 50, 100 nN)

is maintained on the rigid top layers of the tip and the system is allowed to relax for 0.05 ns. Then the tip slides along the x-direction through a distance of 34 nm. A sliding speed of 100 $m\,s^{-1}$ is applied on the tip during the first 14 nm sliding to decrease the time required for the run-in stage, and then the sliding speed is reduced to 50 $m\,s^{-1}$ for the remainder of the simulation. Both of these speeds are fast compared to typical AFM experiments, but necessitated by the small time step of the simulations and the relatively large model system. We observe that the vertical position of the tip is constant after 24 nm of sliding and so identify from 24 to 34 nm as steady-state sliding.

Wear predominantly occurs on the substrate in our model, as expected since the Si tip is harder than the Cu substrate. We therefore quantity wear in terms of plastic deformation of the substrate during sliding. Because MD simulation makes it possible to know the exact position of each atom in the model, we can calculate the displacement of each substrate atom at each moment in time to quantify wear [97]. When the displacement of an atom is greater than the Cu lattice constant (0.361 nm), it is identified as displaced (worn). To characterize wear only in steady-state, a displaced atom is assumed to be one whose position at some sliding distance x (x >24nm) has changed by more than 0.361 nm compared to its position at a sliding distance of 24 nm. The total number of displaced substrate atoms N at a given sliding distance is a measure of substrate wear.

To assess the adhesive strength of the interfaces between different rough tips and substrate, we calculate the interaction energy E between each rough tip and substrate before sliding:

$$E = E_1 + E_2 - E_{12} \tag{4.1}$$

where E_{12} is the total energy of the interface (consisting of the tip and substrate) at equilibrium, and E_1 and E_2 are the total energies of the tip and the substrate at equilibrium, respectively [107]. E_1 and E_2 are calculated from energy minimization after the tip and substrate are relaxed separately. To obtain E_{12}, the tip is placed 0.3 nm above the substrate surface and then the system is relaxed without applied load for 0.05 ns to allow the system to reach a stable potential energy. Then the system energy is minimized to calculate E_{12}.

4.3 Results and Discussion

Figure 4.2 shows wear, quantified as the number of displaced substrate atoms, increases with sliding distance for the different tips and at a range of normal loads; recall that x and N are by definition zero at the beginning of steady-state wear. Wear increases with sliding distance in all cases. If we take the last point on this plot, i.e. wear after 10 nm of steady-state sliding, we can analyze the effects of roughness and load. Figure 4.3 shows the number of displaced substrate atoms as

a function of tip root mean square roughness R_q at applied loads of 10, 25, 50 and 100 nN. At any load, wear increases with tip roughness.

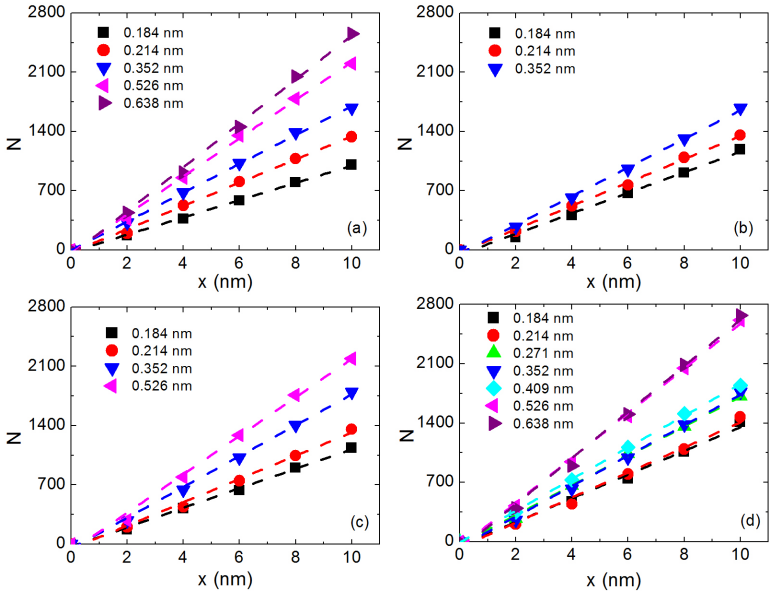

Figure 4.2: Number of displaced substrate atoms N as a function of sliding distance x at 10 nN (a), 25 nN (b), 50 nN (c) and 100 nN (d) using different tips. The relationship between the number of displaced substrate atoms and sliding distance for each tip is linearly fitted (dashed line).

The results are replotted as a function of load for the R_q=0.214 nm case in the inset of Figure 4.3. It can be observed that wear increases with applied load, consistent with previous observations of nanoscale dry sliding [53, 69]. The increase of wear with load is associated with an increase in contact area. Further, the contact area is expected to be non-zero at zero externally applied load due to the adhesion between tip and substrate [49]. To illustrate the effect on wear, a linear fit is used as a rough approximation of the load-wear trend in the inset of Figure 4.3 and shows that the number of atoms displaced does not go to zero. This is consistent with the behavior observed for all model tips.

Adhesive and abrasive wear are typically the two dominant wear mechanisms in dry sliding. Adhesive wear evolves through the formation of adhesive junctions, their growth and their fracture. An expression for adhesive wear at the macroscale is [30],

$$V_{adh} = \frac{k_1 W x}{R_q} \tag{4.2}$$

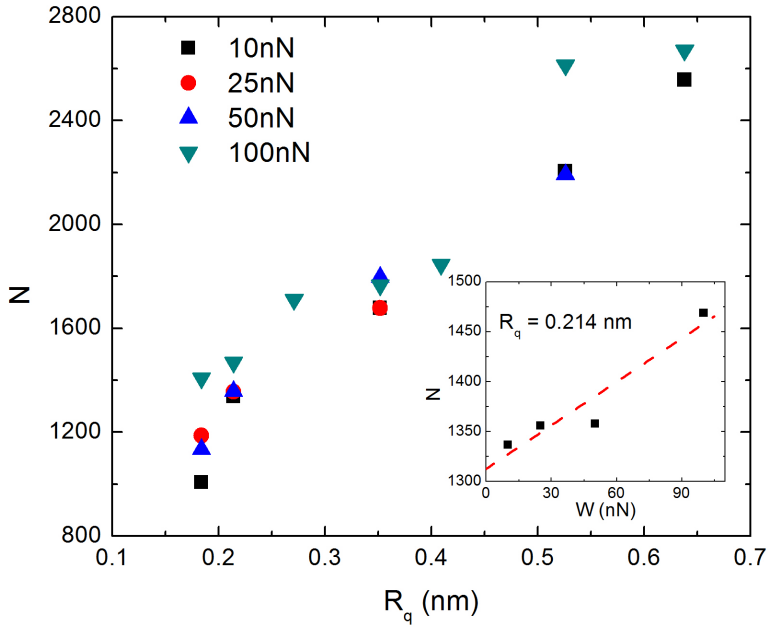

Figure 4.3: Number of displaced substrate atoms N as a function of tip roughness R_q at various loads. The inset shows N as a function of applied load W when R_q is 0.214 nm with a linear fit shown as a dashed line.

where V_{adh} is adhesive wear volume; k_1 is an adhesive wear coefficient which, at the macroscale, is related to the correlation length of the surface and the effective modulus of elasticity. Equation 4.2 predicts that adhesive wear is proportional to applied load W, sliding distance x and the inverse of roughness $1/R_q$. However, only the first two of these trends are observed in our simulation results.

The observation that simulation-predicted wear increases with roughness suggests that it may be dominated by abrasion, in which the asperities of a harder surface cut or plow into a softer counterface. Assuming that the surface consists of an array of conical asperities, abrasive wear at the macroscale can be described by [30]

$$V_{abr} = k_2 W x \overline{\tan\theta} \tag{4.3}$$

where V_{abr} is abrasive wear volume; k_2 is an abrasive wear coefficient that is related to the likelihood of cutting as opposed to ploughing of the asperities; θ is the attack angle and $\overline{\tan\theta}$ is a weighted average of the $\tan\theta$ values of the individual asperities (also called as the roughness factor). Equation 4.3 predicts that abrasive wear is proportional to applied load W, sliding distance x, and the roughness factor $\overline{\tan\theta}$. Although this equation was developed for macroscale wear, it has been suggested

that a larger attack angle will result in more abrasive wear debris at the nanoscale as well [78, 129].

We can calculate the roughness factor for our model. Though we consider each asperity on the tip as spherical rather than conical, the form of Equation 4.3 does not change. The attack angle is measured as the angle between the tangent of the centered asperity bottom and the straight line, which connects the bottommost point on the centered asperity and the point at which it contacts substrate at the front edge during sliding. During sliding, this angle is primarily determined by the tip roughness rather than the normal load as shown in Figure 4.4. This figure also shows that $\tan\theta$ is linearly proportional to the tip roughness when the roughness is larger than 0.214 nm. The exception to this is the atomically smooth tip, that has a roughness of 0.184 nm, but no asperities from which to calculate the attack angle. Although the roughness factor cannot be calculated for this tip, we assume the linear relationship between roughness and abrasion holds such that we can rewrite Equation 4.3 as:

$$V_{abr} = k_2 W x R_q \tag{4.4}$$

and apply this expression to tips of any roughness.

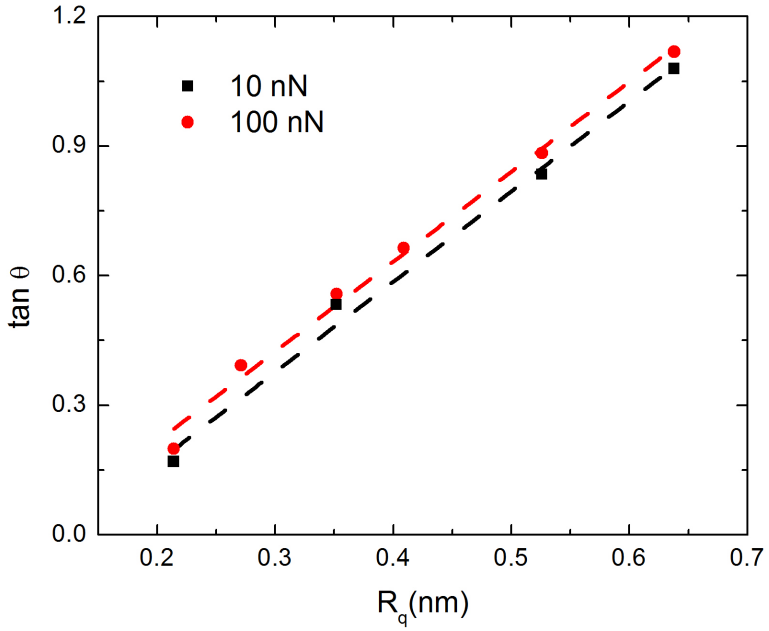

Figure 4.4: Tangent of the attack angle as a function of roughness at 10 nN (black squares) and 100 nN (red circles). The relationship between the tangent of the attack angle and tip roughness is fitted linearly (dashed lines).

Although some of the trends predicted by the macroscopic wear equations are observed in our simulation results, the wear coefficients, k_1 and k_2, are defined in the original expressions in terms of continuum material properties and concepts which may not be applicable at the nanoscale. Further, neither equation explicitly includes the adhesive strength of the interface, which is known to play a significant role in nanoscale contact. Previous simulations have shown that both adhesive and abrasive wear increase with tip-sample interaction strength [34, 125]. Here, we calculate the interaction energy E for each tip using Equation 4.1 and the results are shown in Figure 4.5. It can be seen that the interaction energy increases as the tip roughness decreases. This trend is reasonable because the real contact area decreases when the tip roughness increases, which reduces the strength of the interaction between the tip and substrate.

The interaction energy ΔE between a sphere and a flat surface can be calculated theoretically as [130],

$$\Delta E = \frac{AR}{6D} \tag{4.5}$$

where A is the Hamaker constant, R is the radius of the sphere and D is the distance between the sphere and the surface. To apply this to model tips, such as that shown in the inset of Figure 4.1, we assume the tip consists of independent asperities. When the tip comes into contact with the substrate, the interaction energy can then be regarded as the sum of interaction energy between each asperity and substrate. Because the tip asperity is formed by superposing a spherical cap with a cosine wave, the radius of curvature at the bottom of each asperity is inversely proportional to the amplitude of the cosine wave. Further, since there is a linear relationship between tip roughness and the amplitude of the cosine wave, the interaction energy between the tip asperity and the substrate is inversely proportional to tip roughness. Thus, the interaction energy between the tip and the substrate is inversely proportional to tip roughness, i.e., $\Delta E \propto R_q^{-1}$, consistent with the trend expected for adhesive wear (Equation 4.2).

Equation 4.5 also predicts that interaction energy is a function of the Hamaker constant that is determined by atom density and the strength of the atom-atom interactions. Both adhesive and abrasive wear have been found to increase with interaction energy, which suggests alternative, nanoscale definitions for the coefficients k_1 and k_2 in the macroscopic wear equations. Specifically, since both coefficients are independent of roughness and the tip atom density is constant, k_1 and k_2 may be determined by the strength of the atom-atom interaction strength. This then implies that Equations 4.2 and 4.4 can be applied to describe nanoscale wear, but with different coefficient dependencies. We therefore move forward using these equations to determine the relative contributions of adhesive and abrasive wear modes in the simulation results.

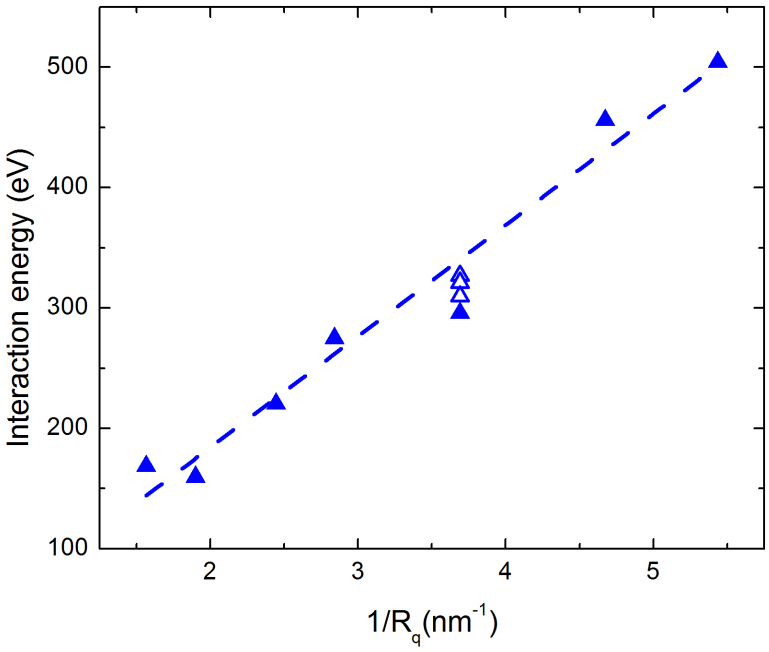

Figure 4.5: The interaction energy between the tip and substrate as a function of the inverse of roughness. Open triangles represent interaction energy calculated from independent simulations of the same tip. The dashed line is a linear fit to the data.

At the nanoscale, we quantify the wear as the number of displaced substrate atoms N, which can be related to wear volume as $N = V/V_0$, where V_0 is the volume of each substrate atom. Thus, N can also be expressed as the sum of the number of substrate atoms displaced due to adhesion N_{adh} and that due to abrasion N_{abr},

$$N = N_{adh} + N_{abr} \tag{4.6}$$

Based on the adhesive wear equation (Equation 4.2) and the abrasive wear equation (Equation 4.4), as well as the fact that the number of displaced substrate atoms increases linearly with sliding distance and that this number is not zero when there is no load applied, the total substrate wear equation can be written

$$N = \left(\frac{1}{R_q} a_{adh} \left(W + b_{adh} \right) + R_q a_{abr} \left(W + b_{abr} \right) \right) x \tag{4.7}$$

where a_{adh} and a_{abr} are coefficients, which are associated with the dependence of adhesive and abrasive wear on tip roughness, and b_{adh} and b_{abr} account for the non-zero contact at zero applied load. Based on the previous analysis, all coefficients in this expression should be functions of the strength of the interaction between atoms in the tip and atoms in the substrate. To obtain a_{adh}, a_{abr}, b_{adh} and b_{abr}, we fit the simulation-predicted data to Equation 4.7. Fitting N/x as a function of tip roughness and load yields $a_{adh} = 0.05 nN^{-1}$, $a_{abr} = 0.165 nm^{-2} nN^{-1}$, $b_{adh} = 175.8 nN$ and $b_{abr} = 2371.6 nN$.

This analysis makes it possible to quantify the relative contributions of adhesion and abrasion to nanoscale wear. First, with the coefficients in Equation 4.7 known, we can calculate N_{adh}/N and N_{abr}/N, which are the percent of wear due to adhesion and due to abrasion, respectively. When the tip roughness is 0.184 nm, the adhesive wear percent is 41, 43, 46 and 50% at applied loads of 10, 25, 50 and 100 nN; when the tip roughness is 0.638 nm, this percent drops to 5.5, 5.9, 6.5 and 7.7% at the same applied loads. Thus, the relative contribution of adhesive wear increases with increasing load and decreases with increasing tip roughness. Note that these trends are dependent on the magnitude of the coefficients in Equation 4.7. For example, in our system $b_{adh} < b_{abr}$ and the adhesive wear percent increases with load, but if b_{adh} is greater than b_{abr}, the adhesive wear percent would decrease with load.

Figure 4.6 shows the simulation data and the wear predicted by Equation 4.7 as a function of tip roughness at 10 nN and 100 nN. The trend indicates that there is some roughness at each load that should exhibit the least wear. This optimum roughness can be calculated by setting the derivative of Equation 4.7 with respect to R_q to zero. So, minimum substrate wear should occur when the tip roughness is $\sqrt{\left(a_{adh} \left(W + b_{adh} \right)\right) / \left(a_{abr} \left(W + b_{abr} \right)\right)}$. This indicates that the optimum tip roughness is determined by adhesive and abrasive wear coefficients as well as the applied

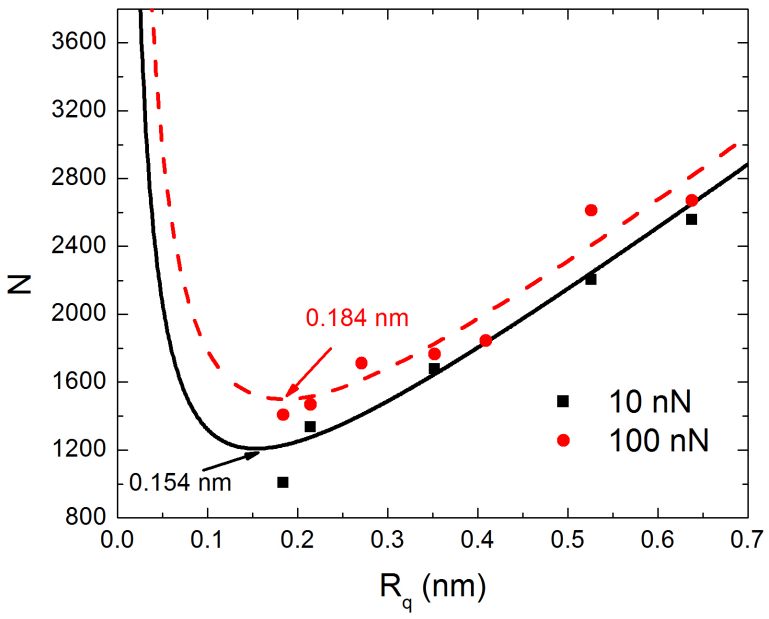

Figure 4.6: Number of displaced substrate atoms as a function of tip roughness at 10 nN (black squares) and 100 nN (red circles). The solid black line and dashed red line show the prediction of total wear from Equation 4.7 at 10 nN and 100 nN, respectively.

load. In this case, the results indicate that, as the load increases, the roughness of the tip that will yield minimum wear increases.

From our simulations, the optimum tip roughness is 0.154 nm, 0.159 nm, 0.168 nm and 0.184 nm when the applied load is 10 nN, 25 nN, 50 nN and 100 nN, respectively. These optimum tip roughnesses approach the lower end of the range (0.17 to 10.5 nm) reported from previous measurement of tip roughness [115, 123]. However, in general, they are quite small and may not be obtained in some experiments. This suggests that, while adhesion determines the size of nanoscale contacts, the effect of roughness on wear can be expected to be determined by abrasion in most cases.

4.4 Summary

MD simulation was used to investigate the effect of tip roughness on nanoscale surface wear during dry sliding at different applied loads. We observed that substrate wear increased with tip roughness, normal load and sliding distance. However, the nonlinear increase of wear with roughness suggested that more than one wear mechanism contributed to the process of removing atoms from the substrate surface. To isolate these contributions, we evaluated expressions for macroscale adhesive and abrasive wear volumes in terms of their ability to describe nanoscale wear. For both adhesion and abrasion, the form of the macroscale expression captures the increase of wear of load and sliding distances observed in the simulations. However, to apply the macroscale equations to nanoscale wear, it was necessary to add a term to account for wear that occurs at zero external load due to the contact area formed by adhesive forces alone. Also, analysis of the form of a theoretical expression for interaction energy implied that, for both wear mechanisms, the wear coefficients that were related to continuum material properties and concepts at the macroscale, were likely to be functions of atom-atom interaction strength in nanoscale sliding. With this modification, the forms of the adhesive and abrasive wear equations could be used to describe the total simulation-predicted nanoscale wear. The resulting expression, with variables fit to the simulation data, enabled prediction of trends beyond those directly observed in simulation. The equation was then used to identify the optimum tip roughness for a tip-sample sliding system to minimize substrate wear, where the optimum tip roughness was load dependent. This provides a way to evaluate the adhesive and abrasive contributions to nanoscale wear as well as to determine the optimum tip roughness to minimize surface wear at a given load.

Chapter 5

AMORPHIZATION-ASSISTED NANOSCALE WEAR

5.1 Introduction

The quality of AFM-based measurements and manufacturing processes are critically dependent on the reliability and durability of the AFM tip itself [100, 131–134]. However, contact between the tip and sample, and the associated high mechanical stress and/or chemical reactions, can result in wear of the tip during use [49, 57, 69, 81, 124, 135–137]. Tip wear is undesirable because it can result in an inability to resolve fine structures during AFM implementation [3]. These wear processes are necessarily nanoscale, suggesting that standard macroscale wear theories may not always be applicable to describe or predict tip wear. Thus, a fundamental understanding of wear mechanisms at the nanoscale is a critical first step towards ensuring the structural and chemical integrity of an AFM tip during instrument use.

Recently, a number of experimental studies have used AFM to characterize nanoscale wear on a variety of different material systems [49, 57, 81, 138]. These studies have been complemented by MD simulation of the AFM tip apex sliding on well-defined substrate surfaces [53, 136, 137]. One observation from such studies is that a crystalline-to-amorphous transition may contribute to nanoscale wear. Experimental measurements of sliding on nanocrystalline diamond revealed that amorphous carbon was formed by the wear process [59, 60]. This observation was explained theoretically by an MD study of a diamond-diamond interface that showed mechanical amorphization drives wear [58]. These studies suggest that wear at the nanoscale may not be a simple process of material removal, but rather may be assisted by material change during sliding. Further complicating the issue is that wear rate is not only a material- and condition-specific property, but is also dependent on how long sliding has progressed. At the onset of sliding, the system is "running-in" and the wear rate can be orders of magnitude higher than that during steady state wear [81]. During running-in, the two sliding partners adjust to each other in terms of stress, surface roughness or crystal orientation [139–141]. The chemical and mechanical processes that occur during running-in are expected to play an important role in steady state wear [139]. This means that understanding the processes that leads to material removal in the first tens of nanometers of sliding is critical to understanding nanoscale wear in general.

In this chapter, MD simulations were used to study the nanoscale wear of a crystalline silicon AFM tip with a native oxide due to sliding against an amorphous silicon dioxide substrate. The size, shape and crystallographic orientation of the tip apex in the MD model were defined to be comparable to those in a corresponding AFM experiment, where the tip was imaged before and after 40 nm of sliding using *ex situ* TEM. All experiments were performed by our collaborator Dr. Virginia Altoe from Lawrence Berkeley National Laboratory (LBNL) [142], Tip wear was quantified in the simulation as the volume of silicon atoms removed from the tip at intervals up to the same 40 nm sliding distance as in the experiment. We also quantified tip amorphization as the change of amorphous tip volume due to sliding. The amorphization process was analyzed in the context of a previously-proposed model for sliding-induced amorphization and considered in terms of local strain within the tip. Lastly, the wear and amorphization rates were evaluated together to determine how these two processes are related and better understand the running-in process at the nanoscale.

5.2 Methods

In the simulation, consistent with the materials in experiments, we modeled a Si tip with an oxidized surface and an amorphous SiO_2 substrate. From the high-resolution tip image obtained from TEM before sliding, shown in Figure 6.1(a), the tip profile was extracted and fit with a parabola, indicated by a dashed red line in the figure. Based on this profile, a corresponding parabolic tip was cut from a cubic model of crystalline silicon. The radius of curvature of the tip profile was estimated to be 1 nm, and the model tip height of 10 nm was sufficient to capture the wear mechanisms expected under the conditions explored here. Then the tip was placed in an atmosphere of atomic oxygen. After the reaction between silicon atoms and oxygen atoms, unbonded oxygen atoms were removed from the simulation box. A cross section of the oxygen-terminated tip is shown in Figure 6.1(b).

The amorphous SiO_2 substrate was created using Visual Molecular Dynamics (VMD), in which crystalline silicon dioxide was annealed by increasing the temperature to 8000 K and then decreasing it to 300 K [143, 144]. The dimensions of the substrate were $23.2 \times 11.4 \times 3.5$ nm in the x-, y-, and z- directions, respectively. To maintain computation efficiency, we did not initially create a substrate long enough to accommodate the entire target sliding distance, i.e. 40 nm. However, when the tip was about to exceed the right boundary during sliding, we removed the worn part of the substrate near the left boundary and added a newly prepared amorphous SiO_2 block to the substrate at the right boundary. The new block of material was added to the model when the tip was at least 5 nm away from the right boundary to ensure there was initially no interaction between the tip and the extended block.

The surface roughness of the SiO_2 substrate was 0.18 nm in the simulation, comparable to 0.22 nm in the experiment. A perspective-view snapshot of the entire model system is shown in Figure 6.1(c).

In the simulated system, the top 2 nm of the tip and the bottom 1.5 nm of the substrate were held rigid. Adjacent to the rigid layer, thermostatted layers were created and held at 300 K using the Langevin thermostat. The Langevin thermostat was applied only in the directions perpendicular to the direction of tip movement. The remaining atoms in the model were free to evolve according to Newtonian dynamics. Periodic boundary conditions were applied in the x- and y- directions. The charge-optimized many-body (COMB) potential for Si/SiO_2 [145] was used with a time step of 0.2 fs to describe all atomic interactions. This potential includes many-body effects that allow for the breaking of existing bonds and the formation of new bonds and has been successfully applied to model a Si/SiO_2 interface [145].

Indentation simulations were performed to partially validate the model. A load of 5 nN was applied to the rigid layer of the tip in the z [1 1 7] direction. After the potential energy of the system was stable, which indicates that the system was at equilibrium, the tip was pulled away from the surface at a constant velocity of 20 m/s. The pull off force was identified as the minimum force during tip retraction. The pull off force measured in the simulation was 12.4 ± 4.1 nN, which was reasonable, although somewhat larger than the 3.93 ± 1.27 nN measured in the experiment. From the Derjaguin−Muller−Toporov (DMT) contact model [83], the work of adhesion in the simulation and experiment were estimated to be 2.0 ± 0.7 J/m^2 and 0.6 ± 0.2 J/m^2, respectively. The difference between experiment and simulation may be attributed to the existence of water in the experiment. In a previous study, it was observed that water adsorbed on silicon dioxide surface can change the adhesive strength of nanoscale contacts [146].

Sliding simulations were then performed to observe tip wear due to shear. A constant normal load of 100 nN was applied on the rigid top layer of the tip and then the system was relaxed for 40 ps, after which the potential energy was stable. Then, the tip was slid along either the x- or the y- direction at a constant speed of 10 m/s. Here, the y [1 -1 0] direction was the same as the sliding direction in the experiment.

To quantify wear, the tip was pulled away from the surface at a constant velocity of 20 m/s after sliding a given distance. Any silicon atom that was removed from the tip was considered to be worn. Then the worn volume was estimated by multiplying the number of worn atoms by the volume per atom, which was taken to be 0.02 nm^3 for a silicon atom in a perfect lattice. The number of silicon atoms changing from crystalline to amorphous after sliding a given distance was calculated using OVITO [147], in which the diamond lattice of silicon is identified using an extended common neighbor analysis [148]. By multiplying the volume per atom, this number can be converted to the tip volume that changed from crystalline to

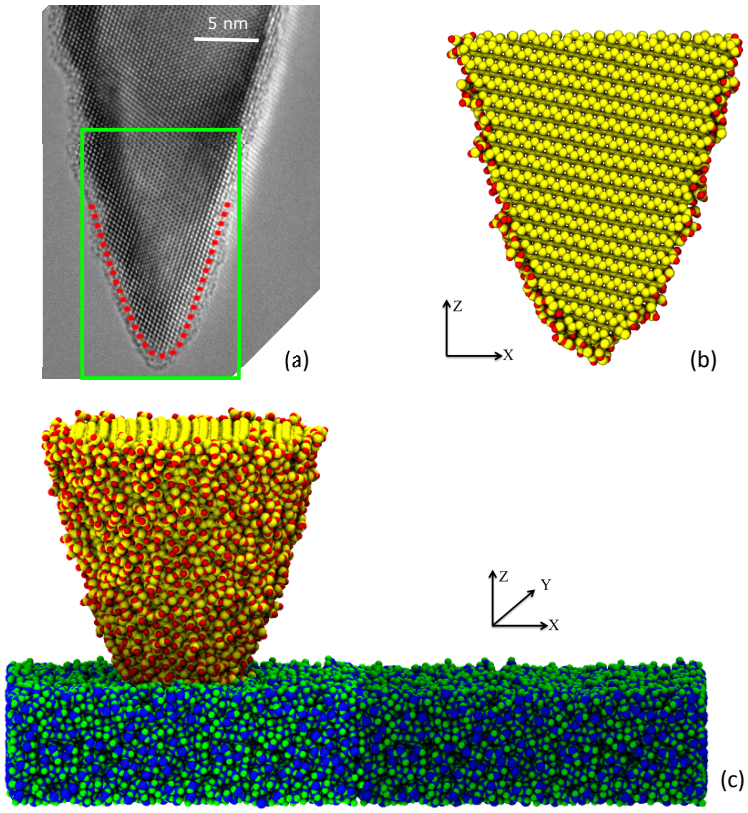

Figure 5.1: (a) TEM image of the silicon AFM tip before sliding, where the dashed line represents a parabola fit to the traced profile of the tip; (b) xz cross section of the model tip, which represents the Si (1 -1 0) plane; (c) Snapshot of the simulation setup. The brightness change of the substrate indicates that the substrate can be extended along its sliding direction. Silicon atoms in the tip are shown in yellow, oxygen atoms in the tip in red, silicon atoms in the substrate in blue, and oxygen atoms in the substrate in green. All experimental results in this chapter are provided by Dr. Virginia Altoe.

amorphous due to sliding.

5.3 Results and Discussion

The tip wear volumes from the experiment and from simulations in two different sliding directions are shown in Figure 5.2(a). Analysis of the simulation results shows that wear increases with sliding distance and that the sliding direction had little effect on wear volume, as expected for an amorphous substrate. However, comparison of the experiment and simulation results at 40 nm reveals that the tip wear volume in the experiment was approximately four times larger than that in the simulation. We also calculated the wear rate as the tip wear volume per sliding distance per load (sometimes called specific wear rate). From the inset in Figure 5.2(a), it can be seen that the wear rate decreased with sliding distance, consistent with the observed in previous AFM measurements of nanoscale wear [81]. It also can be seen that the wear rate is nearly constant by the end of the test, indicating an approach to steady state. The wear rate in the simulation was estimated to be $0.28 \times 10^{-2}\ nm^3 nm^{-1} nN^{-1}$ at a sliding distance of 40 nm. In the experiment, at the same distance, the wear rate was estimated as $1.15 \times 10^{-2}\ nm^3 nm^{-1} nN^{-1}$, larger than that in the simulation.

We next consider possible explanations for the larger experimental wear volume and wear rate at 40 nm. One difference between the simulation and experiment is the wear volume calculation method, which was obtained using a truncated cone approximation in experiment and by summing the volume of removed atoms in simulation. To test this, we applied the truncated cone approximation to calculate the wear volume in the simulation. This yielded a slightly larger wear volume estimate than that obtained from the worn atom count, but the difference between the results from the two calculation methods was small compared to the difference between the simulation and experiment. Thus, the method of calculating the wear volume does not appear to be a major factor contributing to the difference between experiment and simulation. Another possible reason for the difference is that, in the experiment, there may be water on the surface which can change the surface properties such as adhesion [146, 149]. Such surface properties can affect wear [150], suggesting that the presence of water may partially explain the difference between experiment and simulation. However, we believe the most significant factor is likely to be the sliding speed, as discussed next.

The sliding speed in the simulation was 10 m/s, which is orders of magnitude larger than the speed of 2.5 $\mu m/s$ in the experiment. As suggested previously, nanoscale wear may occur through a process of atom-by-atom removal, which involves bond formation and bond breaking at the sliding interface [49]. Within the framework, a smaller sliding speed would provide more time for tip atoms and substrate atoms to form bonds and more bond breaking events are expected during sliding. This is supported by observations from a recent experimental study where

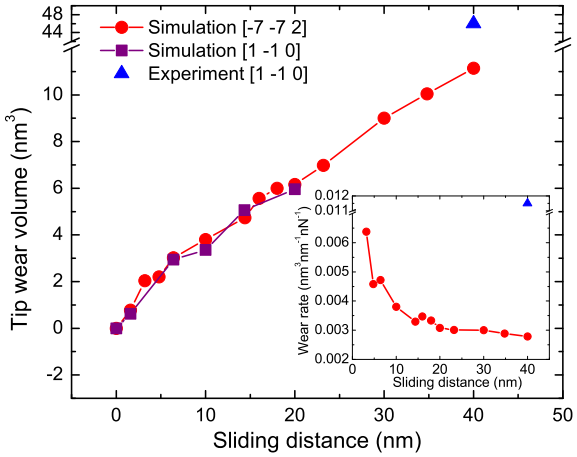

Figure 5.2: (a) Tip wear volume as a function of sliding distance:*red circles* represent simulation-calculated wear volume for sliding direction [-7 -7 2], *purple squares* represent simulation-calculated wear volume for sliding direction [1 -1 0], and the *blue triangle* represents experimentally measured wear volume for sliding direction [1 -1 0]. The inset shows the wear rate as a function of sliding distance for sliding direction [-7 -7 2].

an increase in sliding speed caused a decrease in the wear rate of nanocrystalline Ni [151]. To investigate the effect of sliding speed on wear, we tested additional sliding speeds of 5 and 20 m/s in the simulations. We did not observe any statistically significant difference between the wear rate calculated at these speeds (less than 2 % variation for wear rates at 5, 10 and 20 m/s). However, the speed in the experiment was much slower than any speed accessible to the simulations, so this is likely to be a significant factor causing the difference in wear and wear rates.

We next analyze the amorphization process exhibited in the simulation. During tip indentation, we observed that crystalline silicon atoms near the end of the tip became amorphous as shown in inset (a) of Figure 5.3. Further, it can be seen that, after contact, the amorphous silicon atoms in the tip form a shape that is similar to the pressure profile predicted by continuum contact mechanics models. This suggests a connection between amorphization and contact, which may also imply that amorphization contributes to the sliding wear processes. Evidence of this mechanism was seen in the fact that the worn tip material left on the substrate surface was amorphous; an example of the removal of amorphous material from the bottom of the tip is shown in inset (b) of Figure 5.3. This observation is consistent with previous experimental studies which showed that the wear particles formed from crystalline diamond sliding on diamond were mainly amorphous carbon [60]. We also observed that clusters of material were removed from the tip, consistent

with observations from previous simulations of wear of an amorphous tip [53]. We quantified amorphization during sliding as the change of the total volume of amorphous silicon atoms in the tip (including silicon atoms removed from the tip)relative to the amorphous material volume after indentation and before sliding. As shown in Figure 5.3, amorphous volume change increased with sliding distance, a trend similar to wear volume. The qualitative and quantitative observations suggest that amorphization is happening during sliding and that it may be part of the wear process.

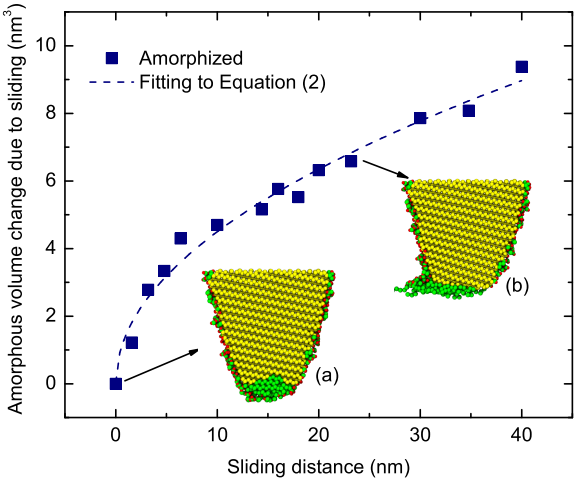

Figure 5.3: Amorphous volume change (the change of the volume of amorphous silicon atoms in the tip relative to the volume of amorphous silicon atoms after indentation and before sliding) as a function of sliding distance for the [-7 -7 2] sliding direction, where the *navy dashed line* represents a fit of Equation 5.2 to the simulation data. Inset are snapshots of the (1 -1 0) plane of the tip (a) after indentation and (b) after sliding ∼25 nm, where the atom color indicates crystallinity; crystalline silicon atoms are shown in yellow, amorphous silicon atoms in green, and oxygen atoms in red.

In a previous study, an amorphization model was proposed to explain the time evolution of the thickness of amorphous carbon during diamond polishing [58]. In this model, crystalline atoms experience random collisions by amorphous atoms and then have a probability to become amorphous. Based on this model, the thickness of the amorphous material $h(t)$ can be expressed as

$$h(t) = -\beta + \sqrt{(\beta + h(t_0))^2 + 2(C_1 P_1 + C_2 P_2)\alpha v_0 (t - t_0)} \tag{5.1}$$

where constants α and β are dependent on the Herschel-Bulkley parameters; t_0 and $h(t_0)$ are the initial time and thickness of amorphous carbon, respectively; C_1 and C_2

are geometry constants for two sliding surfaces; and P_1 and P_2 are the corresponding probabilities of a successful amorphization event, which are dependent on crystal direction.

To analyze amorphization in our simulation, we convert amorphous thickness $h(t)$ to amorphous volume V using $V = Ah(t)$, where we assume that the contact area A changes little with time. In addition, $v_0\,(t - t_0)$ can be replaced by the sliding distance L. Thus, we obtain

$$V = -\beta' + \sqrt{\gamma + \alpha' L} \tag{5.2}$$

where β', γ and α' are constants, which are dependent on parameters α, β, t_0, $h\,(t_0)$, C_1, P_1 and A in Equation 5.1. From Equation 5.2, it can be seen that the change in the amorphous volume is proportional to the square root of sliding distance. We then fit the data from MD to Equation 5.2. The fitting curve is shown in Figure 5.3 and the R-squared value of the fitting is 0.98, indicating that the behavior predicted by the theory agrees well with simulation observations.

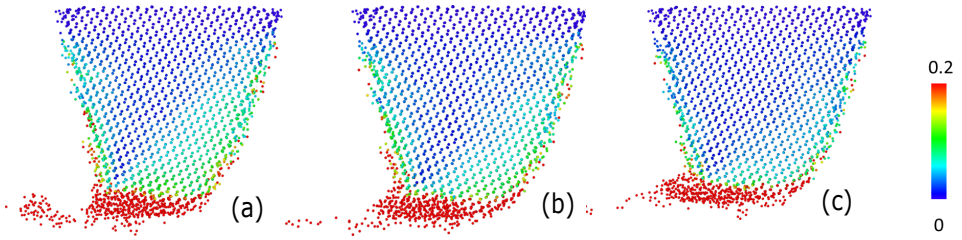

Figure 5.4: The (1 -1 0) plane of silicon atoms in the tip after sliding (a) 6.4 nm, (b) 14.4 nm and (c) 23.2 nm. The color indicates local atomic shear strain.

The remaining question is why the amorphization rate decreases with sliding distance. To explore this, we analyzed the strain distribution within the tip. Strain is quantified using OVITO as the von Mises shear strain per atom [147, 152–154], where the reference atomic configuration for the strain calculation is taken to be the configuration just before sliding begins in the simulation and the cutoff distance for this calculation is 0.6 nm. The results at three representative moments in time are shown in Figure 5.4. Early in the sliding process, we observe large shear strain in the lower right region of the tip. However, as sliding continues, this strain is gradually released. A crystalline-to-amorphous transition in silicon can be assisted by strain [155]. Therefore, the observation that strain is released during sliding may be associated with the decreasing rate of amorphization.

To relate the amorphization to wear, we plot amorphization rate and wear rate as functions of sliding distance as shown in Figure 5.5. Here, the amorphization rate was defined to be similar to wear rate, i.e., the change of amorphous tip volume

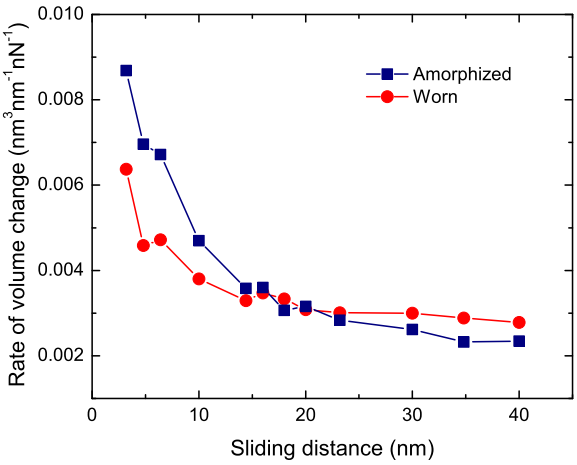

Figure 5.5: Amorphization and wear rate as functions of sliding distance.

per sliding distance per applied load. It can be seen that both wear and amorphization rates exhibit similar trends. That is, they both decrease during running-in and then reach a constant value as the system approaches steady state. This implies that wear occurs through a process in which atoms become amorphous and then are worn away. This is consistent with our observation that worn material is primarily amorphous and that, in steady-state, the total amount of amorphous material within the tip remains constant over time. These observations suggest that wear processes at the nanoscale may be assisted by amorphization, but additional simulations and experiments performed to longer sliding distances would be needed to verify this for steady state sliding.

5.4 Summary

We studied the running-in phase of nanoscale wear using MD simulations and an AFM experiment of a silicon AFM tip sliding against an amorphous silicon dioxide substrate. TEM images of the experimental tip provided a measurement of tip material worn away after 40 nm of sliding. Simulations complement this measurement with atom-scale information about the wear processes that during those 40 nm. From the simulations, we found that tip wear volume increases with sliding distance and the wear rate decreases with sliding distance. Based on the change of wear rate with sliding distance, the beginning of the wear transition from running-in to steady state was observed. The wear rate in the simulation was observed to be smaller than that in the experiment, a difference that was attributed to the possible presence of water in the experiments and the much faster sliding speed in the simulations. The volume and rate of tip material amorphization was also quantified. The change of amorphous tip volume exhibited a square-root relationship with sliding distance, which suggests that a previously-proposed amorphization model

can be applied to wear of silicon. The observed amorphization behavior was related qualitatively to a release of local strain in the tip. Lastly, we calculated the wear and amorphization rates and found that they exhibit similar trends with sliding distance. The similar trends suggest that wear processes may be assisted by amorphization of the material during running-in. Thus, our study provides insight into the mechanisms of shear-induced silicon amorphization and nanoscale wear.

Chapter 6

MOLECULAR DYNAMICS SIMULATION OF AM-AFM

6.1 Introduction

We have introduced nanoscale wear in contact mode AFM so far. Wear can also occur in the imaging process of AM-AFM due to the high frequency of the tip oscillation and intermittent contact between the tip and surface. Previous theoretical studies of AM-AFM have explained the oscillation behavior of the AFM tip in terms of the forces that the tip experiences [156–160]. The dynamics of AM-AFM has also been investigated in experimental studies [22, 161–165]. However, the interactions between the AFM tip and sample that occur during oscillation are still not fully understood. This understanding has been hindered by the fact that the contact between the tip and sample is nanoscale, and so atomic scale interactions between the tip and sample may not be captured by continuum contact mechanics [22, 54]. This limitation suggests the use of MD simulation, a modeling technique that can capture atomic scale interactions and has played an important role in the study of nanoscale contacts in general [16]. However, there have been few MD-based studies focusing on AM-AFM. In the two recent studies where AM-AFM was modeled using MD, it was shown that the local stiffness and energy dissipation for a nanoscale tip and substrate under conditions relevant to AM-AFM could be correlated to local surface topography [166, 167]. In addition, several studies have employed MD simulation and theoretically approximated equations to understand the physics of dynamic AFM [168–170]. However, a fully atomistic MD model of an AM-AFM experiment, including an excitation signal and multiple cycles of oscillation, has not been performed. The development of such a model is necessary to understand the non-linear and complex forces involved in an AM-AFM experiment and to predict the relationship between the nanoscale features of the tip apex and the resolution of topography measurements using AM-AFM.

In this chapter, the AM-AFM experimental setup was simulated using an MD model of an AFM tip apex, sample and virtual representation of the cantilever connected to the tip apex via a harmonic spring. A sinusoidal excitation signal was applied to the virtual cantilever such that the dynamics of model tip apex was determined both by its response to that signal and the interaction with the substrate. This first of its kind MD model therefore captured most of the key features of an AM-AFM experiment. The amplitude and phase shift of the tip oscillation as functions of

tip-sample distance were measured in the simulation and compared to experimental results, as well as analytical models of AM-AFM. The simulation predictions were then fit to an existing AM-AFM model enabling estimation of energy dissipation, which was then analyzed as a function of tip radius.

6.2 Methods

A schematic of the experimental AM-AFM apparatus is illustrated in Figure 6.1(a). The similarities and differences between the experimental setup and the MD simulation depicted in Figure 6.1(b) are highlighted within the figure. The fully atomistic MD simulation consists of a hemispherical Si tip apex and a three-layer graphite substrate. The tip radius is 3 nm and the height of the spherical cap is 1.2 nm. The dimensions of the graphite substrate were $17.8\times17.1\times0.67$ nm^3 in the x-, y- and z-directions, respectively. Substrate atoms at the perimeter of the graphite along the x- and y- directions are fixed. The effect of this boundary setting on the results were found to be negligible, likely due to the relatively large size of the substrate compared to the size of tip. The bottom layer of the substrate and the tip are treated as rigid bodies. The AIREBO potential is employed to describe the carbon-carbon interactions within each graphene layer [171]. The interaction between the graphene layers is modelled by the Lennard-Jones (LJ) potential with parameters ($\varepsilon_{C-C} = 2.84$ meV and $\sigma_{C-C} = 0.34$ nm) adopted from Ref. [171] as well. For the interaction between the tip and substrate, the LJ parameters for Si-C ($\varepsilon_{Si-C} = 8.909$ meV and $\sigma_{Si-C} = 0.3326$ nm) reported in recent work are used [50]. The cut-off distances of the LJ potential for the C-C and Si-C interactions are 1.19 nm [172] and 0.8315 nm [50], respectively. The NVT ensemble, where the number of atoms (N), volume (V) and temperature (T) are conserved, is employed and the Nosé-Hoover thermostat is applied to the free atoms in the system with a target temperature of 300 K. All simulations were performed using LAMMPS simulation software [62, 63] with a time step of 1 fs.

A virtual atom is employed to simulate the cantilever base in an experiment. In the simulation, the virtual atom is connected to the tip apex through a harmonic spring with a stiffness $k = 40$ N/m in the z-direction. The ensemble of tip and virtual atom is placed above the graphite substrate as shown in Figure 6.1. The initial distance between the virtual atom and sample surface is identified as z_c. The virtual atom is oscillated with a sinusoidal excitation signal, mimicking acoustic excitation in an AM-AFM experiment. In the simulation, the sinusoidal excitation signal has an amplitude of 1 nm with a frequency of 200 GHz. The excitation frequency of 200 GHz was chosen to be close to the natural frequency of the tip f_0, which was determined by $(1/2\pi)\sqrt{k/m}$. Here, k is the spring stiffness and m is the mass of the tip. The quality factor Q, which is determined by $Q = \sqrt{mk}/c$, is around 7.3, where c is the damping coefficient of the tip. The value of Q was chosen to be on the same order of magnitude as that in an experiment [156, 157, 164]. The

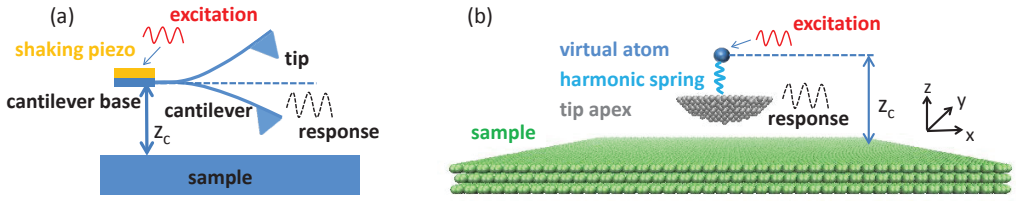

Figure 6.1: (a) A simplified schematic of a dynamic atomic force microscope in which an excitation voltage is applied to the shaking piezo, resulting in the tip oscillation (response); (b) Snapshot of the molecular dynamics simulation in which a model tip apex is connected with a virtual atom by a harmonic spring over a sample (graphite substrate). z_c is the distance between the virtual atom at rest (cantilever base in the simplified experiment schematic) and sample surface. The dynamic response of the tip (black dashed sine wave) is determined by the sinusoidal excitation of the virtual atom (red solid sine wave) and tip-sample interactions.

damping force F applied on the tip is given by $F = -cv$, where v is the velocity of the tip. Because most dynamic AFM experiments operate in the underdamped regime [157], the value of c was chosen to be $4.4 \times 10^{-12} N \cdot s/m$ to ensure that the correct damping of the tip oscillation would be reproduced in the model.

6.3 Results and Discussion

The oscillation amplitude of the tip and the phase shift between the tip oscillation and the excitation signal are two important experimental parameters typically measured in AM-AFM [156]. In the simulation, these parameters were obtained from the oscillating displacement of the virtual atom and the tip. A representative result displaying the time variation of the displacement of the virtual atom and the tip is shown in Figure 6.2. The tip position z can be described by the equation $z = z_0 + A\sin(w_{tip}t - \phi)$, where z_0 is the average tip-sample separation, A is the amplitude of tip oscillation, which is dependent on the angular frequency of the excitation signal w, ϕ is the phase shift compared to excitation signal, and w_{tip} is the angular frequency of tip oscillation, which is determined by w, i.e., $w_{tip} = w$. A sine function was fit to the two waveforms generated by the simulation to obtain the amplitude A and phase shift ϕ. To obtain statistically relevant fits for these values, 10 oscillation cycles for both the virtual atom and tip displacement were acquired in the MD simulation and subsequently fit with the sine waveform. Since z_0 was obtained from the fit, we report subsequent results in terms of z_c, the initial tip-sample distance, since the latter was the parameter specified in our simulation.

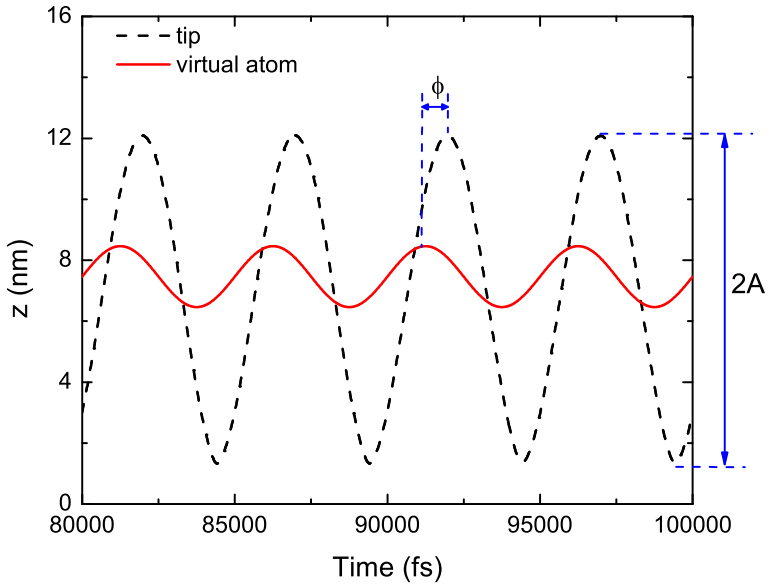

Figure 6.2: The time dependent vertical displacement of the virtual atom (red solid line) and the tip (black dashed line) at z_c equal to 6.79 nm. A is the oscillation amplitude and ϕ is the phase shift between the tip and the virtual atom oscillations.

To verify the ability of the simulation to effectively capture the AM-AFM dynamics, the model-predicted amplitude and phase shift were analyzed as functions of tip-sample distance. The amplitude of tip oscillation A and the corresponding phase shift ϕ as functions of z_c are shown in Figures 6.3 and 6.4. As discussed next, these trends were found to be consistent with previous theoretical and experimental studies.

When the tip was close to the sample, i.e., z_c was less than 9.2 nm, the tip oscillation was determined by both tip-sample interaction and external excitation. From Figure 6.3, the amplitude was observed to linearly increase with z_c. A linear fit to the data points below 8.6 nm yielded a slope 0.989 ± 0.002. This result indicates that the amplitude reduction (free oscillation amplitude minus amplitude of oscillation) is approximately equal to the change of tip-sample distance, consistent with previous theoretical and experimental reports [156, 158, 163]. This trend was observed when z_c was approximately between 2.7 and 8.6 nm. As the tip-sample distance increased beyond this range (z_c greater than 8.6 nm) the amplitude continued to increase, but with a smaller slope; this trend is more clearly seen in the close up in the inset of Figure 6.3. This slope change suggests a transition from the repulsive to attractive regime, as previously observed [159, 160].

When z_c reached 9.2 nm, the amplitude plateaued to a value corresponding to the free oscillation amplitude of $A_0 = 7.2$ nm, where the tip dynamic response

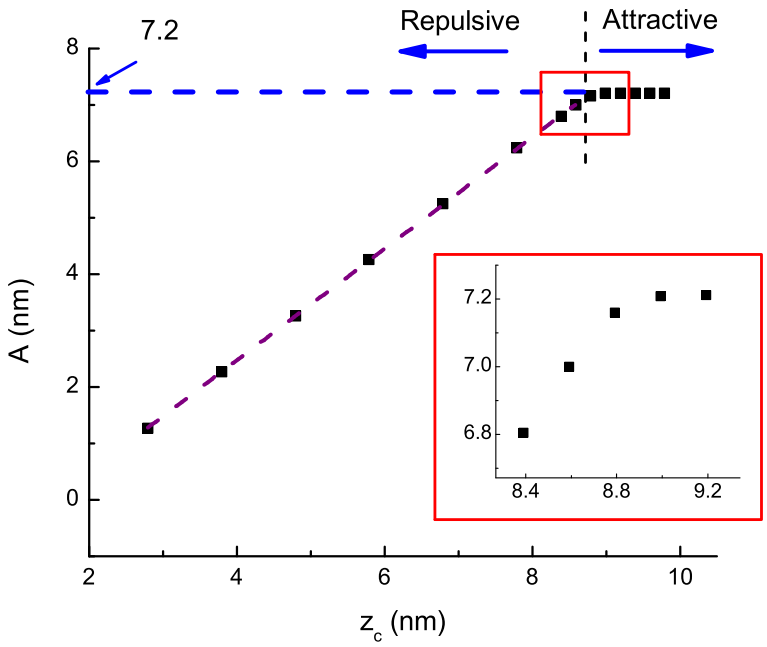

Figure 6.3: The amplitude of tip oscillation A as a function of z_c. Purple dashed line overlayed on the points shows the linear fit to the data below 8.6 nm, yielding a slope of 0.989 ± 0.002. The horizontal blue dashed line represents the free tip oscillation amplitude of 7.2 nm and the vertical black dashed line at $z_c = 8.6$ nm identifies the transition from repulsive to attractive contact between the tip and sample. This transition is observed more clearly in the inset.

was only determined by the excitation signal. In the absence of tip-sample force, the dependence of the amplitude on the excitation frequency can be calculated by the Lorenztian expression [156],

$$A\left(w\right) = \frac{kA_d/m}{\left[\left(w_0^2 - w^2\right)^2 + \left(ww_0/Q\right)^2\right]^{1/2}} \tag{6.1}$$

where, A_d is the amplitude of the virtual atom or the amplitude of the excitation signal and kA_d is equivalent to the excitation force in experiment, w is the angular frequency of virtual atom and w_0 is natural angular frequency of tip, which is determined by $\sqrt{k/m}$. Thus, when the excitation frequency is close to the natural frequency of tip, the amplitude of tip oscillation can be approximated by simplifying Equation 6.1 as $A \approx A_d Q$. From $A_d = 1$ nm and $Q = 7.3$ and in the absence of tip-sample force, the amplitude of tip was calculated to be around 7.3 nm. This approximated result was close to the measured value of 7.2 nm from the simulation.

Although consistent with the theoretical value, the free amplitude in the model was smaller than that typical of an experiment; for example, a more typical value of 10 to 100 nm [22,161–165] is usually encountered in experimental AM-AFM measurements. The free amplitude was restricted to smaller values in this model in part due to the very large frequency of the excitation signal (200 GHz), which was necessitated by the timescale limitations of MD simulation. This limitation resulted from the requirement that atomistic models must run with time steps corresponding to atomic vibrations, corresponding to femtosecond time steps. Thus, a maximum simulation duration is typically on the order of nanoseconds. Therefore, a low oscillation frequency on the order of kilohertz, more closely replicating the cantilever oscillation frequencies encountered in experiments, would require an enormous amount of computation time. The high oscillation frequencies are also a result of the fact that only the end of the tip apex was simulated in the model, rather than the entire tip and cantilever, which typically have dimensions on the order of 10 and 100 microns, respectively. Therefore, the mass of the oscillating body in the simulation is much smaller than that typically encountered in experiments. The high frequency dictated by these simulation constraints in turn limited the free amplitude that could be attained in the simulation. For example, driving the cantilever at higher oscillation amplitudes resulted in an increase in the speed at which the tip apex approached and retracted from the surface, the acceleration at the point of contact, and thus the contact forces, which may cause instability. We observed instability, manifested as non-sinusoidal tip oscillation, for free amplitudes larger than ~ 10 nm. Thus, amplitudes were restricted to below this value to prevent instabilities.

Phase shift is another key experimental parameter measured in AM-AFM, and is often used to map compositional variations in heterogeneous samples [162,

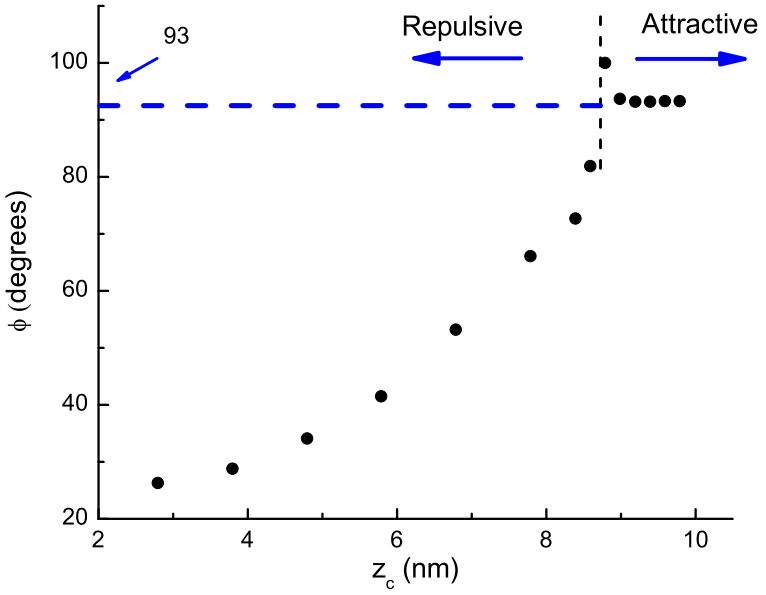

Figure 6.4: The phase shift ϕ as a function of z_c. The horizontal blue dashed line represents the free tip phase shift of 93° and the vertical black dashed line at $z_c = 8.6$ nm identifies the transition from repulsive to attractive contact between the tip and sample.

164,165,173,174]. Assuming that the excitation frequency is exactly the same as the resonance frequency of the tip, it has been proposed that, for a system operating in the repulsive force regime, the phase shift between the drive and cantilever oscillation signal will be less than 90°, and for a system operating in the attractive regime, the phase shift will be greater than 90° [159, 161]. Based on this guideline, both attractive and repulsive regimes can be observed in our simulation results shown in Figure 6.4. When z_c was less than 8.6 nm, the phase shift was below $\sim 90°$ (93° in our simulation) and its magnitude increased with tip-sample distance, due to the inverse relationship between interaction force and tip-sample distance [164]. The phase shift changed quickly to above $\sim 90°$ at a distance of 8.6 nm. This indicates a transition from the repulsive to attractive regime and is in agreement with that exhibited by the amplitude-distance curve shown in Figure 6.3. As z_c continued increasing, the phase shift decreased until z_c became larger than 9.2 nm, at which point the phase shift reached a constant value of 93°. This is consistent with the expected phase shift of $\sim 90°$ when the tip oscillates near its natural frequency [156]. Since most AM-AFM experiments operate in the repulsive regime, a range for z_c of 2.7 to 8.6 nm was identified as the effective AM-AFM operating range for our model. Data from this region will be used to perform the following analyses.

Phase shift is generally related to the local energy dissipation. Specifically,

the sine of the phase shift ϕ is proportional to the amount of inelastic energy transferred from the tip to the sample surface. The relationship between the phase shift ϕ and energy dissipation per period E_{dis} due to the tip-sample interaction has been proposed as [162],

$$\sin\phi = \frac{f}{f_0}\frac{A}{A_0} + \frac{QE_{dis}}{\pi k A_0 A} \tag{6.2}$$

where f is the external excitation frequency and f_0 is the natural frequency. By fitting the simulation-predicted phase shift ϕ (Figure 6.4) versus amplitude A (Figure 6.3) in the repulsive regime, the energy dissipation of the system was found to be $E_{dis} = 276.6$ eV. This value is on the same order of magnitude, but smaller than the 510 eV previously reported for energy dissipation from experimental data similarly analyzed and collected from a similar system [162].

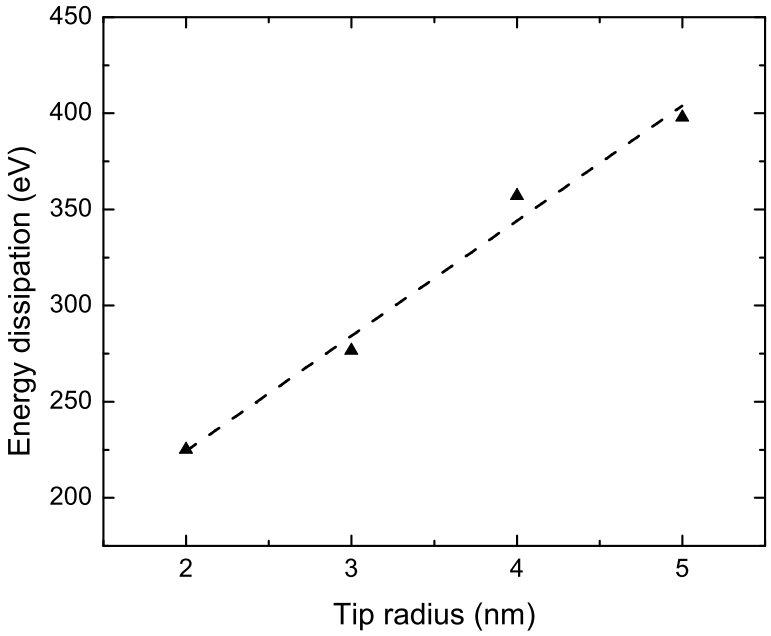

Figure 6.5: Energy dissipation as a function of tip radius. Symbols are data from simulations and the dashed line is a linear fit.

One possible reason for the difference in the energy dissipation between experiment and simulation may be the tip size. As suggested previously [164, 175], Equation 6.2 does not consider the effect of tip radius on the energy dissipation. However, due to the fact that the total van der Waals force is proportional to the radius of the tip, a larger tip radius suggests stronger interaction force between the tip and substrate. The radius of the tip used in the model is 3 nm, which is relatively small compared to that in most AM-AFM experiments. To evaluate the

effect of tip size on energy dissipation, the radius of the model tip was varied with the tip mass held constant by artificially decreasing the mass of individual atoms as the radius was increased so that the natural frequency of the oscillation f_0 was unchanged. As shown in Figure 6.5, the energy dissipation increased with tip radius as expected based on theoretical predictions [173]. Although there are only a few data points, this increase appears to be approximately linear. This trend is consistent with our observation that the adhesive force between the tip and the surface also increased linearly with tip radius, as suggested by the Derjaguin-Muller-Toporov (DMT) adhesive contact mechanics model [176]. This suggests that energy dissipation is correlated to the adhesive tip-sample interactions. However, as the intercept of the linear fit in Figure 6.5 is non-zero, an additional dissipation mechanism, i.e. beyond adhesion hysteresis, must influence the tip-sample contact. In a previous work, adhesion hysteresis, long-range interfacial interactions and viscoelasticity were identified as important energy dissipation mechanisms [173, 174].

Another factor that might affect energy dissipation is the number of graphene layers in the model. The thickness of graphite in an experiment is typically larger than that of the three-layer graphite in the model. To investigate this effect, the number of graphene layers was increased for a simulation with a tip radius of 3 nm and $z_c = 6.79$ nm. When the model contained five or more layers, corresponding to thicknesses larger than the cut-off distance for the LJ interactions between the tip and substrate, the energy dissipation was approximately twice that of the three-layer graphite. Therefore, similar to the tip size, the limited substrate size in this model may also affect energy dissipation. However, a more complete understanding of the energy dissipation mechanisms, using both experimental measurements and simulation predictions, is required to understand the increased trend of energy dissipation with tip radius as well as other parameters that may affect the energy dissipation difference in the current comparison between simulation and experiment.

6.4 Summary

In summary, the first fully atomistic model of an AM-AFM that includes both the tip-sample interactions and a sinusoidal excitation signal has been created. The model was used to predict the amplitude and phase shift of the tip oscillation. These parameters and their variation with tip-sample distance were compared with previous experimental measurements or theoretical predictions. It was found that the free amplitude in the simulation was in good agreement with that predicted theoretically and, in the repulsive regime, the amplitude of tip oscillation increased linearly with tip-sample distance with a slope near unity, consistent with observations from AM-AFM experiments. In addition, the transition from a repulsive to attractive regime in the simulation was identified by the variation of phase lag relative to $\sim 90°$, as suggested by previous experiments and theories. The ability of

the simulations to reproduce these trends indicates that the model is a reasonable representation of an AM-AFM system.

A limitation of the model was revealed by analysis of the energy dissipation obtained by fitting the amplitude and phase shift from the simulations to theory. This energy dissipation was found to be smaller than that reported from similar experiments. The difference was analyzed in terms of the possible differences in tip radius and substrate thickness. The result suggested that model size played a role, but the exact nature of how it affected energy dissipation could not be determined using the simulations alone. Regardless, the ability of the model to capture the dynamics of the AM-AFM suggests that it may be a powerful tool to complement and provide mechanistic insight into experiments performed using this technique. Most significantly, such simulations may be able to shed light on the complex forces in the tip-sample interface and how they affect AM-AFM measurements.

Chapter 7

TIP CONVOLUTION IN AM-AFM MEASUREMENT

7.1 Introduction

Different AFM modes, have been extensively used to characterize the nanoscale structures that exist on many surfaces [4,177]. Despite advances in the control electronics and other experimental parameters that can influence the attainable resolution of an AFM, the size of the tip and associated convolution are limiting factors in the lateral resolution that can be achieved by AFM [178]. The topographic image obtained in AFM assuming a parabolic tip is often used as an example to demonstrate the influence of the tip on the attainable lateral resolution [179]. More recently, greater attention to the exact size and/or shape of the tip, measured through electron microscopy after surface imaging [27], or over the course of a given AFM measurement [22, 47, 49, 100], has shown that AFM tips have more complex shapes than assumed in most tip convolution algorithms. Despite this fact, relative success has been achieved in using tip convolution algorithms, particularly when imaging very hard surfaces with a hard tip apex in AFM. [22].

One possible way to characterize tip size *in-situ* is to use the well-defined geometry of an atomic step, measure the convolved topographic image using AFM, and then determine the shape of the tip apex from the experimentally measured data and the known structure of the atomic step [27]. Many studies on friction at atomic steps [28, 29, 180–185] have suggested that there is a correlation between tip shape and friction at the step. However, the width of the friction peak obtained from measurements of a relatively large tip apex radius sliding up a single atomic step of highly oriented pyrolytic graphite (HOPG) was larger than that calculated based on the geometries of the step and tip [27]. Based on results from atomistic simulations, the difference between measured and calculated friction peaks at the step was hypothesized to be a result of deformation or buckling of the step during contact mode scanning. This fact suggests that friction measurements on steps can be correlated to tip shape.

To avoid the influence of atomic step buckling during AFM imaging, here we explore the correlation between topography measurements obtained using AM-AFM and tip shape. AM-AFM has been used as one imaging mode of the AFM for soft samples, where shearing forces between the tip and sample in contact mode can damage the sample [158]. Rather than pressing a nanoscale tip on the sample and

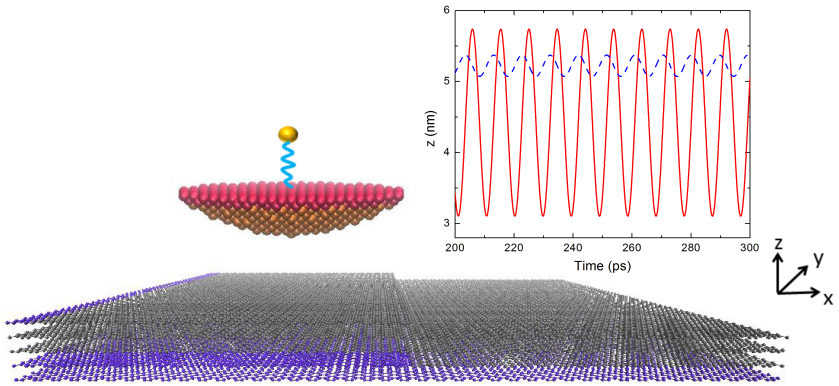

Figure 7.1: A model tip apex is connected with a virtual atom by a harmonic spring over a HOPG substrate. Fixed substrate atoms are represented by blue and the tip atoms colored in red are treated as a rigid body. The inset shows that the tip oscillation (red solid line) is driven by the oscillation of the virtual atom (blue dashed line).

sliding across the surface, as in contact mode, one oscillates the tip above the surface and brings it into contact such that the tip makes a brief repulsive contact with the surface at the turning point of each oscillation cycle, thus effectively eliminating shear stresses on the tip and sample.

AM-AFM was modelled using atomistic simulation in Chapter 6, allowing for greater insight into the buried contact between the tip and sample, as well as the dynamics that occur during AM-AFM scanning. In this chapter, we explored the topographic profiles of single atomic steps of HOPG acquired with AM-AFM using both experiments and MD simulations. All experiments were performed by our collaborators from University of Calgary in Canada [186]. The resolution of the AFM measurements and simulations was quantified as the width of topography at the step. The step widths of the experiments and simulations were compared to the profile calculated from the known step and tip geometries to understand the influence of AM-AFM on measured topographic profiles.

7.2 Methods

The atomistic model is shown in Fig. 7.1. In order to reconstruct the experimental measurement with a computer simulation, we modeled the apex of a hemispherical Si tip with a HOPG substrate. Tips with three different radii (3, 5 and 10 nm) were modelled, all with a tip height of 1.2 nm. The atoms in the top 0.3 nm of the tip were treated as a rigid body, allowing for the tip to be connected to the virtual atom through a harmonic spring that drove the tip oscillation. The substrate consisted of five-layer HOPG with a step edge on the surface along

$x-$direction. To accommodate different tip sizes, the size of the substrate was also varied. The dimensions of the substrate were 17.8×12.2 nm^2 for 3 and 5 nm tips and 29.6×16.6 nm^2 for the 10 nm tip. Fixed substrate atoms are shown in blue in Fig. 7.1. To the left of the step, the bottom two layers of the substrate were fixed and to the right of the step the bottom most layer was fixed to ensure that the measurement would not be affected by the number of free layers. The boundaries were periodic in the y-direction.

The interatomic interactions within the tip and substrate were described by Tersoff [187] and AIREBO [171] potentials, respectively. The interactions between the tip and substrate were modelled by a Lennard-Jones (LJ) potential with parameters $\varepsilon_{Si-C} = 8.909$ meV and $\sigma_{Si-C} = 0.3326$ nm [50]. The temperature of the free atoms was maintained using the Nosé-Hoover thermostat in the NVT ensemble. Simulations were run with a 1 fs timestep [62, 63].

The rigid body of the tip (red in Fig. 7.1) and the virtual atom (yellow in Fig. 7.1), were connected by a harmonic spring with a stiffness of $k = 40$ N/m in the z-direction. A sinusoidal oscillation with an amplitude of 0.15 nm and a frequency of 100 GHz was applied on the virtual atom. The frequency was chosen to be close to the natural frequency of the tip. Although this frequency is much larger than that in an experiment due to the timescale limitations of the simulation, the simulations still complement experiments by providing atomic-scale details about the materials and the interactions between them. The damping coefficient c was chosen to be 1.22×10^{-10} N·s/m to ensure that the tip would oscillate in the underdamped regime [157]. The quality factor was determined as 8.78 from $Q = \sqrt{mk}/c$, where m, k and c are mass of the tip, spring stiffness and damping coefficient, respectively. A plot of the oscillation of the virtual atom and tip during a representative simulation is shown in the inset of Fig. 7.1. A more detailed description of AM-AFM modeling approach can be found in Chapter 6.

7.3 Results and Discussion

Five tips in the experiment were used to perform the topography measurement. The surface topography was fit with a sigmoidal function shown in Equation 7.1.

$$z = z_2 + \frac{z_1 - z_2}{1 + \exp\left(\frac{x - x_\circ}{\tau}\right)} \tag{7.1}$$

In this equation, z_1 is the height of the bottom of the step in nm, z_2 is the height of the top of the step in nm, $x_\circ$ is the lateral position where the step is located, τ is the rate of change of the topography at the step in nm. Then the width of the topography at the step, or step width, was calculated as $w = x_2 - x_1$, where x_1 and x_2 are obtained from Equation 7.1 when z equal $(z_1 - 0.02nm)$ and $(z_2 + 0.02nm)$, respectively. Here, 0.02 nm is chosen to be 10 times the tolerance

used to determine constant amplitude in the MD simulations. Fig. 7.2 shows the variation of the step width measured in AFM experiments with the radius of the AFM tip used in imaging the surface. The associated TEM images of the tip apex for each data point measured are shown in the insets of Fig. 7.2. The general trend of the experimental data shows a monotonic increase of the step width with increasing radius of the tip apex. We also calculated the step width analytically using the known geometry of the step and that of an ideal hemisphere, assuming only hard shell repulsion and no deformation on the tip and the surface using Equation 7.2:

$$z = h - R + \sqrt{R^2 - x^2} \tag{7.2}$$

where h is the step height of a single HOPG atomic step, R is the tip radius, and (x, z) represents the tip trajectory. This calculation is shown in Fig. 7.2 as a dashed line and, in all cases, the measured step width is larger than that calculated from geometry and the difference increases with tip size.

One explanation for the difference between experimentally-measured step width and the geometric calculation is that the real tips are not perfectly hemispherical, as assumed in the geometric calculation. To isolate this effect, we analyze the MD simulation results for model hemispherical tips. Fig. 7.3 shows the topographic line profile generated using a 5 nm model tip. Each data point (red filled circles) was acquired by oscillating the tip in the MD simulation and then changing the tip-sample separation until the amplitude ratio was 0.8 (with a tolerance of 0.002 nm). The topographic profile was then fit to Equation 7.1, as shown by the black dashed line. The geometric profile (Equation 7.2) is shown as the blue solid line. A green vertical line at x=0 nm marks the known location of the step edge in the simulation. It can be seen that the total simulation step width has contributions from both the left side and right side of the actual position of the step. This is in contrast to the geometric model whose width is entirely on the right side of the step. To quantify the contributions of the left and right side of the step location to the overall step width, we define the right step width w_r as the distance from the location of the step to x_2 and left step width w_l as the distance from the location of the step to x_1.

Fig. 7.4 shows the variation of w_r (green squares), w_l (red circles), and the total step width (blue triangles) as functions of tip radius. The step width obtained from the geometric model is also shown as a dashed line. We observe that all widths increase with increasing tip apex radius, as expected. Also, for the three tips investigated (3 nm, 5 nm, and 10 nm), the geometric step width is in good agreement with the simulation-calculated right step width. This suggests that the overall step width is due to the geometric contribution, which is manifested as the width to the right of the step location, and another contribution, which increases the width on the left side of the step. The contribution on the left side of the step will be discussed in the next section.

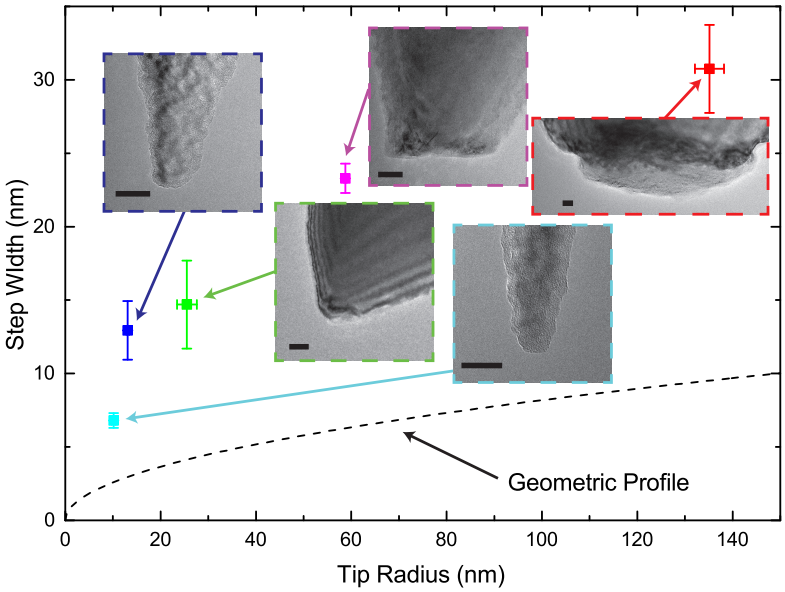

Figure 7.2: Experimental measurements of step width versus tip radius measured for five tips. The insets show TEM images of the individual tips used to determine the tip radius on the x-axis. The black solid line in each TEM image corresponds to 20 nm. Each TEM image has been rotated to compensate for the tilt angle of the AFM cantilever with respect to the plane of the sample surface. The dashed black line indicates the step width calculated from the known geometry of the step and an ideal hemisphere with varying radius, referred to as the geometric profile. All experimental results in this chapter are provided by the group led by Dr. Philip Egberts.

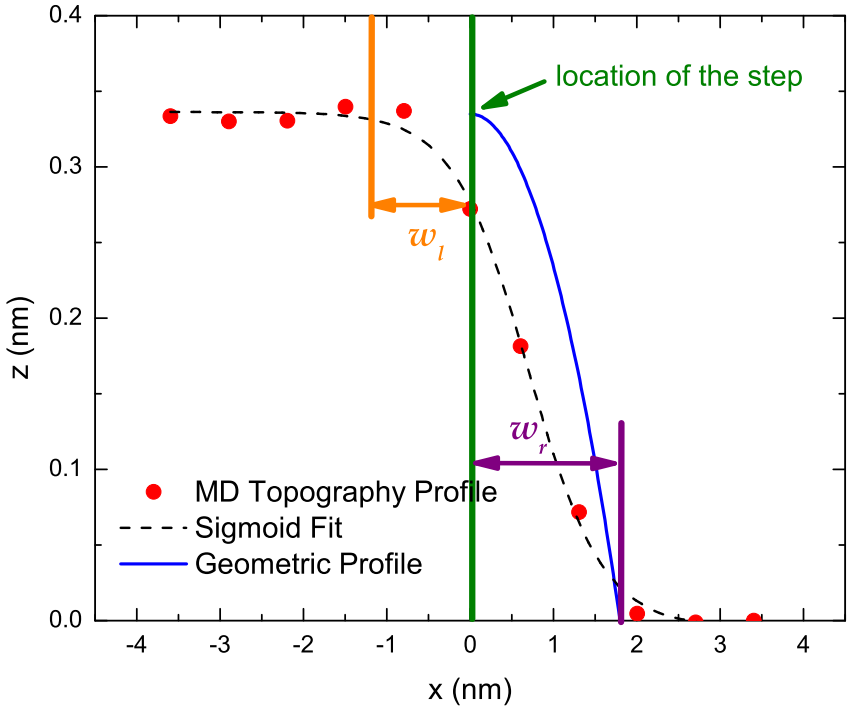

Figure 7.3: The simulation-calculated topographic profile of a single HOPG step traced with a tip having a radius of 5 nm (red circles) and an amplitude ratio of 0.8. The sigmoidal fit of the topographic data is shown as a black dashed line. The solid blue line represents the topographic profile generated assuming the geometric model. For both the MD simulation data and the geometric profile, the location of the step edge of the surface is at an x-position of 0 nm, denoted by a green vertical line. The step width to the right of x=0 nm is denoted by w_r, and corresponds to the distance in x between the solid green line (at position x=0 nm) and the x position where z=0.02 nm, denoted by the purple vertical line. The step width to the left of x=0 nm is denoted by w_l, and corresponds to the distance in x between the x position where z=0.32 nm, denoted by the vertical orange line, and x=0 nm.

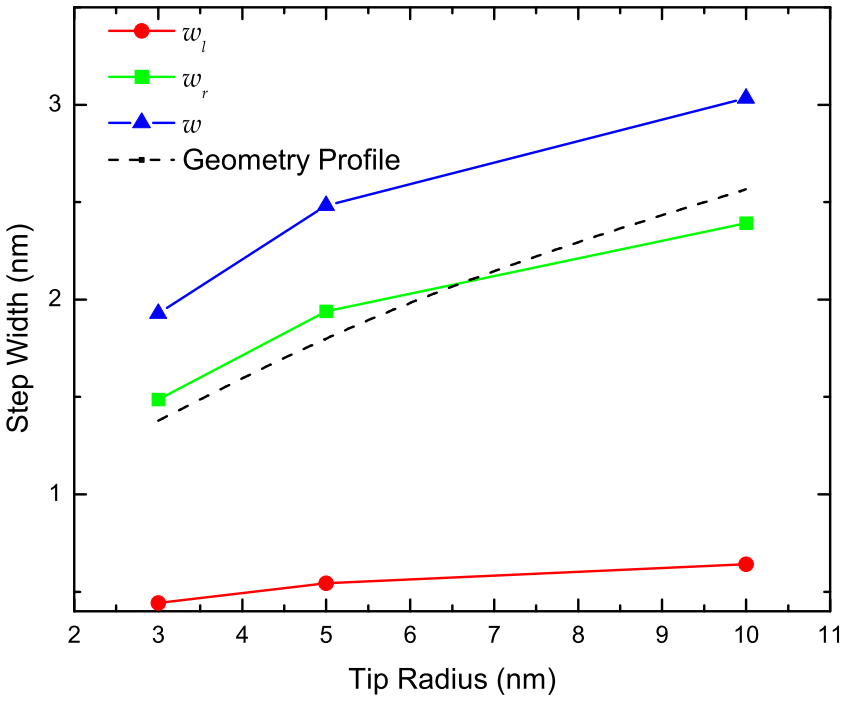

Figure 7.4: Step widths from MD simulations with different model tip sizes. The total step width w (blue triangles), the width of the profile to the right of the step w_r (green squares) and the width of the profile to the left of the step w_l (red circles) all increase with tip radius. The width calculated assuming only geometric effects is shown as a black dashed line.

We first examine the origin of the difference between the simulation data and the geometric profile, where effects of the non-ideal shape of the experimental tips or any environmental effect (discussed later) can be neglected. As observed in Fig. 7.4, the difference between the simulation and geometric step width is primarily on the left side of the step. One major difference between the simulation and geometric calculation is that the calculation assumes rigid bodies, whereas both the tip and substrate can deform in the simulation. Indeed, we observe that the topmost layer of graphene deflects downward by approximately 0.13 ± 0.04 nm when the tip is at its lowest position during the oscillation. However, the amount of deflection does not increase with tip size, unlike w_l which increases with tip radius as shown in Fig. 7.4. So the substrate deflection cannot directly explain the observed step width.

We hypothesize instead that deflection indirectly affects step width through its relationship to contact area and the associated average interaction force, which is the sum of the repulsive and attractive forces the tip experiences at the bottom of the oscillation cycle. The size of the contact area (number of tip and substrate atoms that interact) when the tip is near the substrate determines the interaction force. Near the step, the contact area is necessarily smaller and the interaction force decreases. This will in turn affect the amplitude of the tip's oscillation such that, to maintain a constant amplitude ratio, the vertical position of tip will be lowered, which will change the measured topography.

To evaluate this hypothesis, a constant height simulation (as opposed to constant amplitude) was performed with the 10 nm tip. Fig. 7.5 (a) shows the number of tip atoms in contact with the substrate when the tip is closest to the surface during one oscillation cycle, where contact atoms are identified as tip atoms that are within 3.7 Å from the substrate; Fig. 7.5 (b) shows the corresponding interaction force averaged over 10 cycles of stable oscillation; and Fig. 7.5 (c) shows the amplitude of tip oscillation. The step edge is located at $x = 0$ nm. We observe that between -2 and 0 nm (the same region where we measured w_l in Fig. 7.3) the number of contact atoms decreases, the interaction force decreases, and the amplitude increases slightly. This result is consistent with previous studies which showed that, in the repulsive regime, larger repulsive force can result in a smaller amplitude [159, 188]. Thus, a larger oscillation amplitude is observed when the tip is closer to the step edge. Then, in order to maintain a constant amplitude, the vertical position of the tip needs to be lowered, as shown in Fig. 7.5 (d) from a simulation run at constant amplitude. Correspondingly, the number of contacting atoms and interaction force will result in a decrease in z-topographic height as the tip approaches the step under constant amplitude imaging conditions.

Further support for the hypothesis is provided by analyzing the effect of tip size on step width. As shown in Fig. 7.4, w_l increases monotonically with tip radius. If our hypothesis is correct, the effect of the step on the interaction force should increase with radius as well. Fig. 7.6 shows the interaction force as a function of

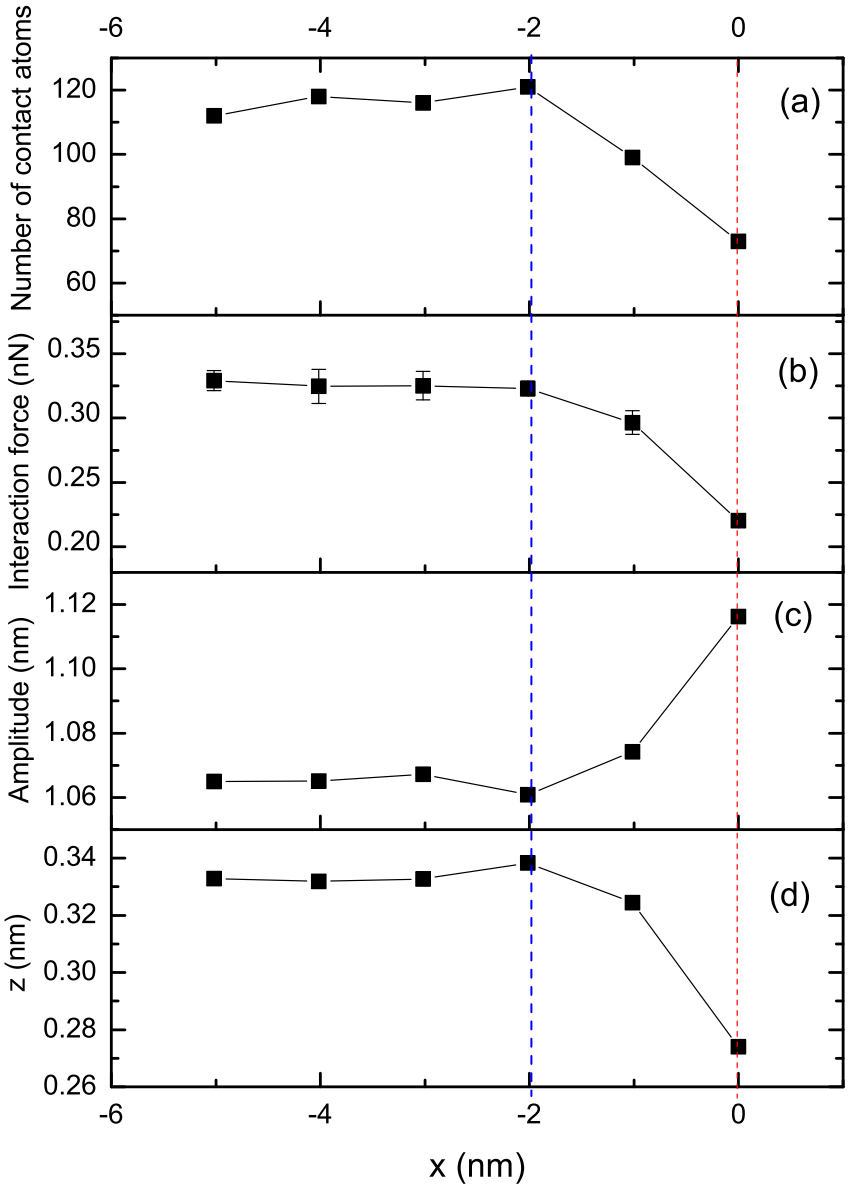

Figure 7.5: From a constant z height simulation, the variation of the (a) number of contacting atoms at the lowest point in the oscillation cycle, (b) interaction force, and (c) amplitude of oscillation are plotted as a function of x lateral translation. (d) Topography from a constant amplitude simulation. The blue dashed line indicates where the steps starts to affect measurements and red dashed line corresponds to the location of the step.

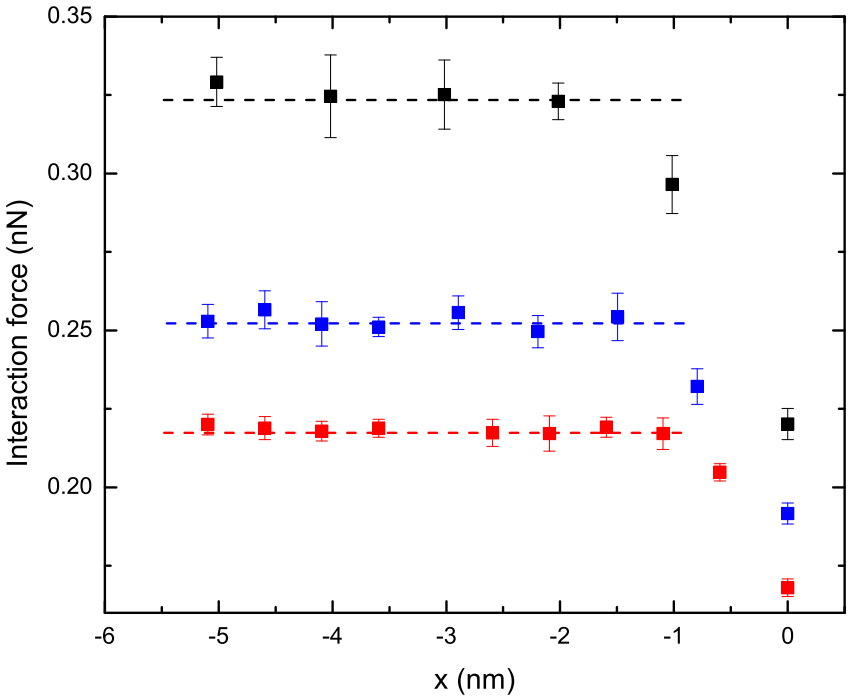

Figure 7.6: The interaction force as a function of tip lateral position at constant height measurement obtained from MD simulations for three tips having a radius of 3 nm (red squares), 5 nm (blue squares), and 10 nm (black squares). The error bars represent the variation of interaction force during 10 oscillation cycles. Dashed lines represent the interaction force when the tip is on the terrace for each of the three tips. We observe that the simulation data decreases relative to this mean value and that the position at which the decrease begins is further from the step (the step is at x=0) for larger tips.

lateral position for different tips. It can be seen that increasing the tip size causes the interaction force to start decreasing further from the step (further left). This can be correlated directly to the increase in w_l with tip size.

Experimental measurements to examine the decrease in the amplitude at a constant tip-sample separation were conducted. However, due to the small range over which this variance occurs, the difficulty in locating the exact step edge in comparison with the measured step edge, and the drift associated with experimental measurements on this length scale, we were unable to conclusively experimentally validate this simulation data. However, we do see a significant variance in the feedback signal (the oscillation amplitude) in the region of the step edge, which increases when scanning from a higher step of graphite to a lower one.

It is likely that the mechanism proposed in the previous paragraphs based on the simulation results is relevant and contributes to the step width measured in experiment as well. However, there are expected to be other factors at play as well, including the irregular shape of the tip, which we can only characterize in the axis perpendicular to the cantilever beam. An additional contributing factor to the much larger step width measured in AFM experiments compared with the geometric model may arise from the approximate 30% humidity present in experiments. This humidity will increase the contact between the tip and sample, as a meniscus bridge will likely form between the tip and sample [189, 190]. However, the contribution of a water meniscus, beyond perhaps increasing the contact area, has been suggested to have little influence on the tip sample contacts in dynamic AFM [156]. A detailed experimental evaluation of graphite steps becomes difficult, as ultra-high vacuum (UHV) AM-AFM images, required to evaluate the impact of water on the acquired images, are difficult to acquire because the Q-factor becomes very large, and thus the response time of the cantilever dynamics to tip-sample interactions becomes unrealistically long for image acquisition. On the other hand, the measured topographic profile convolved with the shape of the tip apex on diamond-like carbon films and measured in a drier environment has been shown to match well with TEM images [22]. The lower relative humidity during those measurements was approximately 15%, possibly contributing to the greater overlap of the tip convolution measurement and the real shape of the tip.

7.4 Summary

Experimental and simulation measurements of tip-convoluted topographic measurements of HOPG single atomic steps were performed. Both show that the topographic measurements are convolved with the shape of the tip, specifically influencing the sharpness of the step measured in the lateral dimensions. This blurring of the atomic step due to the finite shape of the tip was greater than expected from simple geometric calculations. It was further shown that the difference between the geometric calculation and the measured/simulated step widths increased with tip size. Detailed analysis of the simulations suggested that this difference is in part attributable to the deformation of the bodies, in this case primarily of the HOPG, due to the interactions between tip and substrate. This deformation is not accounted for in the geometric calculation that assumes rigid bodies. The effect of the deformation is that there is a finite contact area between tip and substrate. The size of this contact is at a maximum when the tip is in the lowest position of its oscillation and is approximately the same for any position on a terrace of HOPG. However, as the tip approaches the step edge, the contact area decreases, causing an increase in the interaction forces, which in turn affects the amplitude of oscillation. In a constant amplitude measurement, this is adjusted for by shifting the equilibrium position of the tip, which is detected as a change in the measured topography. This deviation

occurs further from the step for larger tips, thus also explaining the observed effect of tip size.

In general, this study has shown that, although AM-AFM does not suffer from issues associated with step bucking like contact mode, there are still limitations to correlating step topography measurements directly to tip size. This limitation arises in part due to the sensitivity of AM-AFM to the interaction forces that occur during dynamic oscillation, and deformation. Deformation is determined by the elastic properties of the contacting bodies and the strength of the interaction between them. Therefore, for as well-defined material system, it may be possible to relate the deformation of the bodies and corresponding contact area, and then deduce the tip size from the difference between the measured topography and the combined effects of the rigid-body tip-substrate convolution and the deformation effects. However, this calculation would be very sensitive to the specific materials used in the experiment, and also likely affected by the operating conditions. Nonetheless, AM-AFM may be useful as a technique for measuring tip wear since normally the elasticity and interaction strength of the materials remain nearly the same throughout a test. Therefore, the change in the measured step width should be a reasonable reflection of the change in effective tip size.

Chapter 8

SUMMARY AND FUTURE WORK

8.1 Summary

In summary, we investigated the mechanisms of nanoscale wear in contact mode AFM and the effect of nanoscale wear on topography measurement using AM-AFM. The primary research tool used was MD simulation, where models were designed to capture the key features of corresponding experiments. Wear was characterized in terms of wear track depth, change in tip radius and chemical composition. From comparison of the experimentally-observed and simulation-predicted wear, it was shown that nanoscale wear can occur through both adhesion and abrasion, and that the dominant mode is determined by both sliding distance and load. Then we studied the running-in phase of nanoscale wear and showed that wear processes may be assisted by amorphization of the material, that is, crystalline materials become amorphous before they are removed from the surface. The effects of load, adhesion and roughness of the surface on nanoscale wear were also explored, which enabled the prediction of wear beyond that direct observable in simulation to identify an optimum sliding interface to minimize wear. In addition, we developed a novel model of AM-AFM in MD simulation, where the model AFM tip responds to both tip-sample interactions and to a sinusoidal excitation signal. This model was then used to examine the influence of wear of the AFM tip apex on the measured surface topography of single HOPG atomic steps. The majority of the contents of this thesis has been published in peer-reviewed journals [69, 125, 142, 186, 191, 192].

8.2 Future Work

We propose several important future research topics to further explore the mechanisms of wear and its effect on nanoscale devices. Based on the research in this thesis, there are four proposed research topics. First, in Chapter 2, it was shown that atom-by-atom wear could not be applied to describe wear under the conditions in that study. Thus, it is necessary to further explore the applicability of the atom-by-atom wear model and factors such as the size, load, materials and environment which may affect it. Second, in Chapter 6, we developed an MD model of AM-AFM, which enabled the estimation of energy dissipation during the tip oscillation. However, the wear mechanisms during AM-AFM are still not clear. Therefore, further MD studies, which can provide direct access to the atomic structure at the interface, are necessary to explore wear mechanisms during AM-AFM. Third, in Chapter 7, tip wear was expressed in terms of the radius of the tip. However, the tip does not only change in size but also in shape due to wear. Using simulation, it would be possible to directly relate sliding wear from contact AFM with resolution loss in AM-AFM. Fourth, nanoscale wear not only occurs in AFM measurement, but also in other devices such as nanoelectromechanical systems (NEMS). Thus, it is important to explore wear mechanisms in these devices and determine how wear affects the electrical, chemical and mechanical properties of components. The details of each proposed topic will be described in following sections.

8.2.1 Thermal Activation of Nanoscale Wear

Atom-by-atom wear, which is based on the assumption that wear occurs gradually and through atom-by-atom, stress-assisted bond formation and breaking, has been proposed in previous experimental research [49, 57, 86]. We analyzed wear trends from MD simulation in the context of atom-by-atom wear in Chapter 2, and showed that atom-by-atom wear is not always applicable. Thus, it is necessary to further investigate the effects of tip size, load, materials and environment on atom-by-atom wear, which may help define the applicability of atom-by-atom wear under different conditions.

In the context of atom-by-atom wear, the process of atom loss is considered to be a thermally activated process, in which the temperature plays an important role. However, during sliding, the temperature at the interface is difficult to measure in experiments. In addition, it has been shown that, in the atom-by-atom wear model, sliding velocity has an effect on wear rate due to contact time [49]. Therefore, MD simulation can be used to analyze wear trends by changing variables such as temperature, sliding velocity and surface termination. Studying the effects of various conditions on the atom-by-atom removal process can provide insight into the underlying mechanisms of atomic wear.

This study can then help resolve the question of whether the Archard's wear law or atom-by-atom wear is applicable at different conditions. A previous study

using MD simulation showed a transition from atom-by-atom wear to plastic wear: at low load, the atomic wear rate has an exponential dependence on the normal stress, in agreement with the mechanically assisted bond-rupture theory; while at high load, the plastic wear rate exhibits a linear dependency on the normal stress [136]. This wear transition was observed to occur due to load, but may also occur due to changes in sliding velocity, temperature and surface termination. Thus, future MD studies combined with experimental investigations can isolate the applicability of different wear mechanisms and the transition from one wear mechanism to another under different conditions.

8.2.2 Nanoscale Wear in AM-AFM

In Chapters 6 and 7, we developed an AM-AFM model in MD simulation and it was applied to investigate the effect of tip size on topography measurement. This model can also be used to explore wear during operation of AM-AFM. Wear during contact mode AFM has been studied widely [35, 37, 38, 40, 49, 100]. AM-AFM was introduced in part to reduce wear during measurement by eliminating the shearing forces between the tip and sample due to sliding and reducing the total amount of time the tip interacts strongly with the sample. However, tip wear can still be a limiting factor in AM-AFM due to the high frequency of tip oscillations. Previous experimental studies have shown that tip wear can be significant in AM-AFM imaging and wear mechanisms such as fracture, plastic deformation and atom-by-atom removal can also exist in AM-AFM [20, 22, 23, 161].

In contact mode AFM, the dominating wear mechanism is dependent on the stress and tip-sample interactions at the contact interface. The mechanisms of wear in AM-AFM are likely to be different due to the negligible shear stresses. For example, it has been suggested that the cyclic loading and impact as well as high compressive stresses in AM-AFM are the main factors that contribute to wear [22]. Despite the importance of wear in AM-AFM, there are limited studies on wear in this operation mode. In addition, forces and stresses are generally calculated using simplified analytical equations in AM-AFM experiments [12, 193]. Modelling AM-AFM would provide information about the tip-sample interaction force and the buried interface near the contact, which are not directly accessible to current experimental techniques. Thus, the newly developed AM-AFM model in MD simulation can be used to gain insight into the atomic wear that occurs during an AM-AFM measurement.

8.2.3 The Effect of Sliding Wear on Resolution in AM-AFM

We studied the effect of tip wear on topography measurement by changing the radius of the tip in Chapter 7. Although tip radius is a typical characterization of wear, that is, larger tip radius indicates more wear, wear can also cause a change of the tip shape [23, 47]. In addition, in Chapter 5, we showed that materials

can become amorphous near the sliding interface. Both tip shape and material change can contribute to resolution loss in AFM measurement. Thus, future research may try to understand the effect of actual tip wear on resolution in AM-AFM measurement. A sliding simulation, such as those described in Chapter 2 or 5, can be performed first, so that the evolution of the tip can be observed. Then tips obtained by sliding different distances can be used for topography measurement in AM-AFM as described in Chapter 7. This would make it possible to explore the effect of actual tip wear on image resolution and identify the individual contributions of tip size, shape and material to resolution loss.

8.2.4 Nanoscale Wear in Nanoelectromechanical Systems

In this thesis, we discussed nanoscale wear in AFM measurement. In addition to AFM, nanoscale wear can also affect the performance and life of NEMS such as nanoswitches. In the application of nanoswitches, one electrode is at a distance away from another electrode due to the balance of interaction force between them when the switch is in the off-state. When a voltage is applied between the two electrodes, electrostatic force contributes to the interaction force, which brings the two electrodes closer so that the tunnelling current goes through and the switch is on. Typical nanoswitch structures require high actuation voltages and can fail through permanent adhesion of device components [45]. Thus, a thin film consisting of dielectrics is placed between the active metal electrodes to reduce the adhesion [45, 51, 194]. However, although the increasing thickness of thin films can reduce adhesion between active electrodes, it can also lower the electrical contact conductance. Optimal performance of nanoswitches requires substantial contact conductance and minimal asperity deformation, which is mainly due to adhesion between the metal electrodes. Therefore, using MD simulation to study the relationship between deformation of electrodes and electrical conductivity can provide insights into the mechanisms of the switching process and the materials choice for such applications.

MD simulations have been widely used to study the adhesion between asperities. However, using them to study electrical conductivity is challenging since electrons are not explicitly modelled in MD simulation. A recently-developed method, EChemDID (electrochemical dynamics with implicit degrees of freedom), which is implemented in MD simulation, has been used to investigate nanoscale resistance switching [51, 52]. Here we propose using this method to study the relationship between adhesion, deformation and conductivity of electrodes in nanoswitches.

To demonstrate this approach, we applied EChemDID to an indentation model as shown in Figure 8.1. The MD model consisted of a gold tip apex indenting an eight-layer graphite substrate. The tip was initially placed over the center of the graphite, where the interaction between the tip and substrate is negligible. Before indentation, the model system was equilibrated at the desired temperature. Then

the tip was displaced in the z direction at a certain speed, towards the substrate. To calculate the interaction force between the tip and substrate during indentation, the system should be relaxed. The z-component of the force on the tip was then averaged during the relaxation. In order to calculate the conductance during indentation, an external voltage difference was applied to the top of the tip and the right end of the substrate as shown in Figure 8.1(a). After equilibration of the electrochemical potential of the system, the current going through the gold-graphite interface was calculated using EChemDID. From Figure 8.1(b), it can be seen that the current going through the interface increases with the load applied on the tip. This method provides a possible way to study the relationship between the deformation of contact asperities and conductivity. Then it can further help determine optimal parameters, such as material, size, shape and surface termination, for good conductance and minimal deformation of contact asperities used in nanoswitches.

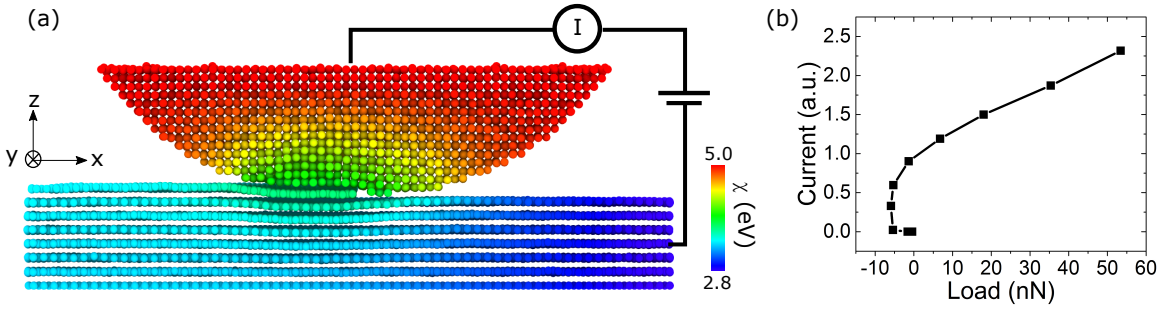

Figure 8.1: (a) Cross section of a simulation system consisting of a gold tip and graphite substrate with a step edge. The external voltage difference was applied to the top of the tip and the right end of the substrate. The color on the atoms indicates the electrochemical potential after equilibration. (b) Current going through the gold-graphite interface as a function of load applied on the tip.

8.3 Concluding Remarks

In this work, we developed models of contact and amplitude modulation AFM in MD simulation and studied sliding wear by varying materials, load, adhesive strength and surface roughness. Some results were compared with those observed from AFM and TEM experiments. A newly developed AM-AFM model in MD simulation was applied to investigate the effect of tip size on topography measurements. In this chapter, we presented future research topics. Specifically, it is important to further explore the applicability of different wear mechanisms and extend the study of nanoscale wear to other applications, such as AM-AFM and NEMS. Combined with the current research, we hope the proposed studies can provide better understanding of the mechanisms of nanoscale wear and the effect of wear on the operation of nanoscale devices. With the advancement of experimental techniques and atomistic simulations, a scientific understanding of wear at the nanoscale can eventually enable technological progress for a variety of fields and applications.

BIBLIOGRAPHY

[1] G. Binnig, C. F. Quate, C. Gerber, Atomic force microscope, Phys. Rev. Lett. 56 (1986) 930.

[2] D. Rugar, P. Hansma, Atomic force microscopy, Phys. Today 43 (1990) 23–30.

[3] A. Yacoot, L. Koenders, Aspects of scanning force microscope probes and their effects on dimensional measurement, J. Phys. D Appl. Phys. 41 (2008) 103001.

[4] I. Szlufarska, M. Chandross, R. W. Carpick, Recent advances in single-asperity nanotribology, J. Phys. D: Appl. Phys. 41 (2008) 123001.

[5] H.-U. Danzebrink, L. Koenders, G. Wilkening, A. Yacoot, H. Kunzmann, Advances in scanning force microscopy for dimensional metrology, CIRP Ann.-Manuf. Techn. 55 (2006) 841–878.

[6] S. Morita, R. Wiesendanger, E. Meyer, Noncontact atomic force microscopy, Springer Science, 2002.

[7] F. J. Giessibl, Advances in atomic force microscopy, Rev. Mod. Phys. 75 (2003) 949.

[8] Z. Liu, Z. Li, G. Wei, Y. Song, L. Wang, L. Sun, Manipulation, dissection, and lithography using modified tapping mode atomic force microscope, Microsc. Res. Techniq. 69 (2006) 998–1004.

[9] Y. Wang, X. Hong, J. Zeng, B. Liu, B. Guo, H. Yan, AFM tip hammering nanolithography, Small 5 (2009) 477–483.

[10] B. Cappella, G. Dietler, Force-distance curves by atomic force microscopy, Surf. Sci. Rep. 34 (1999) 1–104.

[11] G. Binnig, M. Despont, U. Drechsler, W. Haeberle, M. Lutwyche, P. Vettiger, H. Mamin, B. Chui, T. W. Kenny, Ultrahigh-density atomic force microscopy data storage with erase capability, Appl. Phys. Lett. 74 (1999) 1329–1331.

[12] S. Hu, Nonlinear dynamics and force spectroscopy in dynamic atomic force microscopy, ProQuest, 2007.

[13] G. Meyer, N. M. Amer, Simultaneous measurement of lateral and normal forces with an optical-beam-deflection atomic force microscope, Appl. Phys. Lett. 57 (1990) 2089–2091.

[14] R. W. Carpick, N. Agrait, D. Ogletree, M. Salmeron, Measurement of interfacial shear (friction) with an ultrahigh vacuum atomic force microscope, J. Vac. Sci. Technol. 14 (1996) 1289–1295.

[15] D. Ogletree, R. W. Carpick, M. Salmeron, Calibration of frictional forces in atomic force microscopy, Rev. Sci. Instrum. 67 (1996) 3298–3306.

[16] Y. Dong, Q. Li, A. Martini, Molecular dynamics simulation of atomic friction: A review and guide, J. Vac. Sci. Technol., A 31 (2013) 030801.

[17] R. Bennewitz, Friction force microscopy, Mater. Today 8 (2005) 42–48.

[18] C. M. Mate, G. M. McClelland, R. Erlandsson, S. Chiang, Atomic-scale friction of a tungsten tip on a graphite surface, Phys. Rev. Lett. 59 (1987) 1942.

[19] S. Y. Krylov, J. W. Frenken, The physics of atomic-scale friction: Basic considerations and open questions, Phys Status Solidi B 251 (4) (2014) 711–736.

[20] V. Vahdat, R. W. Carpick, Practical method to limit tip–sample contact stress and prevent wear in amplitude modulation atomic force microscopy, ACS Nano 7 (2013) 9836–9850.

[21] A. San Paulo, R. Garcia, High-resolution imaging of antibodies by tapping-mode atomic force microscopy: attractive and repulsive tip-sample interaction regimes, Biophys. J. 78 (2000) 1599–1605.

[22] V. Vahdat, D. S. Grierson, K. T. Turner, R. W. Carpick, Mechanics of interaction and atomic-scale wear of amplitude modulation atomic force microscopy probes, ACS Nano 7 (2013) 3221–3235.

[23] V. Vahdat, K. E. Ryan, P. L. Keating, Y. Jiang, S. P. Adiga, J. D. Schall, K. T. Turner, J. A. Harrison, R. W. Carpick, Atomic-scale wear of amorphous hydrogenated carbon during intermittent contact: A combined study using experiment, simulation, and theory, ACS Nano 8 (2014) 7027–7040.

[24] L. Gross, F. Mohn, N. Moll, B. Schuler, A. Criado, E. Guitián, D. Peña, A. Gourdon, G. Meyer, Bond-order discrimination by atomic force microscopy, Science 337 (2012) 1326–1329.

[25] D. G. de Oteyza, P. Gorman, Y.-C. Chen, S. Wickenburg, A. Riss, D. J. Mowbray, G. Etkin, Z. Pedramrazi, H.-Z. Tsai, A. Rubio, et al., Direct imaging of covalent bond structure in single-molecule chemical reactions, Science (2013) 1434–1437.

[26] T. Çagin, J. Che, M. N. Gardos, A. Fijany, W. A. Goddard III, Simulation and experiments on friction and wear of diamond: a material for mems and nems application, Nanotechnology 10 (3) (1999) 278.

[27] Y. Dong, X. Z. Liu, P. Egberts, Z. Ye, R. W. Carpick, A. Martini, Correlation between probe shape and atomic friction peaks at graphite step edges, Tribol. Lett. 50 (2013) 49–57.

[28] Z. Ye, A. Otero-de-la Roza, E. R. Johnson, A. Martini, Effect of tip shape on atomic-friction at graphite step edges, Appl. Phys. Lett. 103 (2013) 081601.

[29] P. Egberts, Z. Ye, X. Z. Liu, Y. Dong, A. Martini, R. W. Carpick, Environmental dependence of atomic-scale friction at graphite surface steps, Phys. Rev. B 88 (2013) 035409.

[30] B. Bhushan, Introduction to tribology, John Wiley & Sons, 2013.

[31] R. Chattopadhyay, Surface wear: analysis, treatment, and prevention, ASM International, 2001.

[32] M. d' Acunto, Theoretical approach for the quantification of wear mechanisms on the nanoscale, Nanotechnology 15 (2004) 795–801.

[33] E. Gnecco, R. Bennewitz, E. Meyer, Abrasive wear on the atomic scale, Phys. Rev. Lett. 88 (2002) 215501.

[34] E. J. Sandoz-Rosado, O. A. Tertuliano, E. J. Terrell, An atomistic study of the abrasive wear and failure of graphene sheets when used as a solid lubricant and a comparison to diamond-like-carbon coatings, Carbon 50 (2012) 4078 – 4084.

[35] R. Bassani, M. D'Acunto, Nanotribology: tip-sample wear under adhesive contact, Tribol. Int. 33 (2000) 443 – 452.

[36] A. Hase, H. Mishina, M. Wada, Microscopic study on the relationship between AE signal and wear amount, Wear 308 (2013) 142–147.

[37] A. Gåård, N. Hallbäck, P. Krakhmalev, J. Bergström, Temperature effects on adhesive wear in dry sliding contacts, Wear 268 (2010) 968–975.

[38] A. G. Khurshudov, K. Kato, H. Koide, Wear of the AFM diamond tip sliding against silicon, Wear 203 (1997) 22–27.

[39] J. P. Killgore, R. H. Geiss, D. C. Hurley, Continuous measurement of atomic force microscope tip wear by contact resonance force microscopy, Small 7 (2011) 1018–1022.

[40] K. Degiampietro, R. Colaco, Nanoabrasive wear induced by an AFM diamond tip on stainless steel, Wear 263 (2007) 1579–1584.

[41] J. Zhong, R. Shakiba, J. B. Adams, Molecular dynamics simulation of severe adhesive wear on a rough aluminum substrate, J. Phys. D Appl. Phys. 46 (2013) 055307.

[42] J. Archard, W. Hirst, The wear of metals under unlubricated conditions, in: Proceedings of the Royal Society of London A: Mathematical, Physical and Engineering Sciences, Vol. 236, The Royal Society, 1956, pp. 397–410.

[43] E. Rabinowicz, The least wear, Wear 100 (1984) 533–541.

[44] B. Gotsmann, M. Lantz, Quantized thermal transport across contacts of rough surfaces, Nat. Mater. 12 (2013) 59–65.

[45] F. Niroui, A. I. Wang, E. M. Sletten, Y. Song, J. Kong, E. Yablonovitch, T. M. Swager, J. H. Lang, V. Bulovic, Tunneling nanoelectromechanical switches based on compressible molecular thin films, ACS Nano 9 (2015) 7886–7894.

[46] C. Tangpatjaroen, D. S. Grierson, S. Shannon, J. E. Jakes, I. Szlufarska, Size dependence of nanoscale wear of silicon carbide, ACS Appl. Mater. Inter.

[47] J. Liu, J. K. Notbohm, R. W. Carpick, K. T. Turner, Method for characterizing nanoscale wear of atomic force microscope tips, ACS Nano 4 (2010) 3763–3772.

[48] K.-H. Chung, Y.-H. Lee, H.-J. Kim, D.-E. Kim, Fundamental investigation of the wear progression of silicon atomic force microscope probes, Tribol. Lett. 52 (2013) 315–325.

[49] T. D. Jacobs, R. W. Carpick, Nanoscale wear as a stress-assisted chemical reaction, Nat. Nanotechnol. 8 (2013) 108–112.

[50] Z.-Y. Ong, E. Pop, Molecular dynamics simulation of thermal boundary conductance between carbon nanotubes and SiO_2, Physical Review B 81 (2010) 155408.

[51] N. Onofrio, D. Guzman, A. Strachan, Atomic origin of ultrafast resistance switching in nanoscale electrometallization cells, Nat. Mater. 14 (2015) 440–446.

[52] N. Onofrio, A. Strachan, Voltage equilibration for reactive atomistic simulations of electrochemical processes, J. Chem. Phys. 143 (2015) 054109.

[53] Z. Sha, V. Sorkin, P. S. Branicio, Q. Pei, Y. Zhang, D. J. Srolovitz, Large-scale molecular dynamics simulations of wear in diamond-like carbon at the nanoscale, Appl. Phys. Lett. 103 (2013) 073118.

[54] B. Luan, M. O. Robbins, The breakdown of continuum models for mechanical contacts, Nature 435 (2005) 929–932.

[55] B. Luan, M. O. Robbins, Contact of single asperities with varying adhesion: comparing continuum mechanics to atomistic simulations, Phys. Rev. E 74 (2006) 026111.

[56] Y. Mo, K. T. Turner, I. Szlufarska, Friction laws at the nanoscale, Nature 457 (2009) 1116–1119.

[57] B. Gotsmann, M. A. Lantz, Atomistic wear in a single asperity sliding contact, Phys. Rev. Lett 101 (2008) 125501.

[58] L. Pastewka, S. Moser, P. Gumbsch, M. Moseler, Anisotropic mechanical amorphization drives wear in diamond, Nat. Mater. 10 (2011) 34–38.

[59] A. R. Konicek, D. Grierson, P. Gilbert, W. Sawyer, A. Sumant, R. W. Carpick, Origin of ultralow friction and wear in ultrananocrystalline diamond, Phys. Rev. Lett. 100 (2008) 235502.

[60] F. Van Bouwelen, A. Bleloch, J. Field, L. Brown, Wear by friction between diamonds studied by electron microscopical techniques, Diam. Relat. Mater. 5 (1996) 654–657.

[61] J. Haile, Molecular dynamics simulation, Vol. 27, Wiley, New York, 1992.

[62] http://lammps.sandia.gov.

[63] S. Plimpton, Fast parallel algorithms for short-range molecular dynamics, J. Comput. Phys. 117 (1995) 1–19.

[64] N. Tambe, B. Bhushan, Nanowear mapping: a novel atomic force microscopy based approach for studying nanoscale wear at high sliding velocities, Tribol. Lett. 20 (2005) 83–90.

[65] A. M'ndange-Pfupfu, J. Ciston, O. Eryilmaz, A. Erdemir, L. Marks, Direct observation of tribochemically assisted wear on diamond-like carbon thin films, Tribol. Lett. 49 (2013) 351–356.

[66] T.-H. Fang, C.-I. Weng, Three-dimensional molecular dynamics analysis of processing using a pin tool on the atomic scale, Nanotechnology 11 (2000) 148–153.

[67] D. Mulliah, S. Kenny, R. Smith, C. Sanz-Navarro, Molecular dynamic simulations of nanoscratching of silver (100), Nanotechnology 15 (2004) 243–249.

[68] C. Tourek, S. Sundararajan, Study of atomic force microscopy probes using a local electrode atom probe microscope, Microsc. and Microanal. 15 (2009) 290–291.

[69] X. Hu, C. J. Tourek, Z. Ye, S. Sundararajan, A. Martini, Structural and chemical evolution of the near-apex region of an atomic force microscope tip subject to sliding, Tribology Letters 53 (2014) 181–187.

[70] J. Tersoff, Modeling solid-state chemistry: Interatomic potentials for multicomponent systems, Phys. Rev. B 39 (1989) 5566–5568.

[71] S. Munetoh, T. Motooka, K. Moriguchi, A. Shintani, Interatomic potential for Si–O systems using tersoff parameterization, Comp. Mater. Sci. 39 (2007) 334–339.

[72] M. S. Daw, M. I. Baskes, Embedded-atom method: Derivation and application to impurities, surfaces, and other defects in metals, Phys. Rev. B 29 (1984) 6443.

[73] J. Adams, S. Foiles, W. Wolfer, Self-diffusion and impurity diffusion of fee metals using the five-frequency model and the embedded atom method, J. Mater. Res. 4 (1989) 102–112.

[74] H. Gong, W. Lu, L. Wang, G. Li, S. Zhang, The effects of substrate size and temperature on the deposition of Cu clusters on a Si substrate, J. Appl. Phys. 112 (2012) 024903–024903.

[75] H. J. Hwang, O.-K. Kwon, J. W. Kang, Copper nanocluster diffusion in carbon nanotube, Solid State Commun. 129 (2004) 687–690.

[76] R. R. Gamache, J. Fischer, Half-widths of H216O, H218O, H217O, HD16O, and D216O: I. comparison between isotopomers, J. Quant. Spectrosc. Radiat. Transfer 78 (2003) 289–304.

[77] S. Sundararajan, B. Bhushan, Micro/nanotribology of ultra-thin hard amorphous carbon coatings using atomic force/friction force microscopy, Wear 225 (1999) 678–689.

[78] X. Zhao, B. Bhushan, Material removal mechanisms of single-crystal silicon on nanoscale and at ultralow loads, Wear 223 (1998) 66–78.

[79] K.-H. Chung, D.-E. Kim, Fundamental investigation of micro wear rate using an atomic force microscope, Tribol. Lett. 15 (2003) 135–144.

[80] C. Lhymn, R. Light, Effect of sliding velocity on wear rate of fibrous polymer composites, Wear 116 (1987) 343–359.

[81] H. Bhaskaran, B. Gotsmann, A. Sebastian, U. Drechsler, M. A. Lantz, M. Despont, P. Jaroenapibal, R. W. Carpick, Y. Chen, K. Sridharan, Ultralow nanoscale wear through atom-by-atom attrition in silicon-containing diamond-like carbon, Nat. Nanotechnol. 5 (2010) 181–185.

[82] H. Kitsunai, K. Kato, K. Hokkirigawa, H. Inoue, The transitions between microscopic wear modes during repeated sliding friction observed by a scanning electron microscope tribosystem, Wear 135 (1990) 237–249.

[83] B. Derjaguin, V. Muller, Y. P. Toporov, Effect of contact deformations on the adhesion of particles, J. Colloid Interf. Sci. 53 (1975) 314–326.

[84] P. Sheehan, The wear kinetics of nacl under dry nitrogen and at low humidities, Chem. Phys. Lett. 410 (2005) 151 – 155.

[85] N.-S. Park, M.-W. Kim, S. Langford, J. Dickinson, Atomic layer wear of single-crystal calcite in aqueous solution using scanning force microscopy, J. Appl. Phys. 80 (1996) 2680–2686.

[86] T. D. Jacobs, B. Gotsmann, M. A. Lantz, R. W. Carpick, On the application of transition state theory to atomic-scale wear, Tribol. Lett. 39 (2010) 257–271.

[87] G. Dearnaley, Adhesive, abrasive and oxidative wear in ion-implanted metals, Mater. Sci. Eng. 69 (1985) 139–147.

[88] K. Hokkirigawa, K. Kato, An experimental and theoretical investigation of plowing, cutting and wedge formation during abrasive wear, Tribol. Int. 21 (1988) 51–57.

[89] N. K. Myshkin, M. I. Petrokovets, A. V. Kovalev, Tribology of polymers: adhesion, friction, wear, and mass-transfer, Tribol. Int. 38 (2006) 910–921.

[90] L. Chen, D. Rigney, Adhesion theories of transfer and wear during sliding of metals, Wear 136 (1990) 223–235.

[91] B. Bhushan, J. N. Israelachvili, U. Landman, Nanotribology: friction, wear and lubrication at the atomic scale, Nature 374 (1995) 607–616.

[92] M. de Rooij, D. Schipper, Analysis of material transfer from a soft workpiece to a hard tool: Part I-lump growth model, J. Tribol. 123 (2001) 469–473.

[93] M. de Rooij, D. Schipper, Analysis of material transfer from a soft workpiece to a hard tool: part iiexperimental verification of the proposed lump growth model, J. Tribol. 123 (2001) 474–478.

[94] M. Chandross, C. D. Lorenz, M. J. Stevens, G. S. Grest, Probe-tip induced damage in compliant substrates, J. Manuf. Sci. E. 132 (2010) 030916.

[95] J. Heinrichs, M. Olsson, S. Jacobson, Mechanisms of material transfer studied in situ in the sem:: Explanations to the success of DLC coated tools in aluminium forming, Wear 292 (2012) 49–60.

[96] M. de Rooij, G. van der Linde, D. Schipper, Modelling material transfer on a single asperity scale, Wear 307 (2013) 198–208.

[97] M. Vargonen, Y. Yang, L. Huang, Y. Shi, Molecular simulation of tip wear in a single asperity sliding contact, Wear 307 (2013) 150–154.

[98] O. D. S. Ferreira, E. Gelinck, D. de Graaf, H. Fischer, Adhesion experiments using an AFM-parameters of influence, Appl. Surf. Sci. 257 (2010) 48–55.

[99] L. Gou, X. Shi, X. Zhao, Y. Bai, L. Qiao, Composite diamond-DLC coated nanoprobe tips for wear resistance and adhesion reduction, Surf. Coat. Technol. 206 (2012) 4099–4105.

[100] J. Liu, D. S. Grierson, N. Moldovan, J. Notbohm, S. Li, P. Jaroenapibal, S. D. O'Connor, A. V. Sumant, N. Neelakantan, J. A. Carlisle, et al., Preventing nanoscale wear of atomic force microscopy tips through the use of monolithic ultrananocrystalline diamond probes, Small 6 (2010) 1140–1149.

[101] A. Khurshudov, K. Kato, Wear of the atomic force microscope tip under light load, studied by atomic force microscopy, Ultramicroscopy 60 (1995) 11–16.

[102] C. Tourek, S. Sundararajan, Characterization of the chemistry and structure of material transfer on AFM tips resulting from contact and sliding experiments, Microsc. Microanal. 17 (2011) 748–749.

[103] C. Tourek, S. Sundararajan, Detection and analysis of the native oxide layer and material transfer on the near apex region of atomic force microscope tips using atom probe tomography, Microsc. Microanal. 18 (2012) 914–915.

[104] J. Song, D. J. Srolovitz, Adhesion effects in material transfer in mechanical contacts, Acta Mater. 54 (2006) 5305 – 5312.

[105] J. Song, D. J. Srolovitz, Mechanism for material transfer in asperity contact, J Appl. Phys. 104 (2008) 124312.

[106] H. Yu, J. B. Adams, L. G. Hector Jr, Molecular dynamics simulation of high-speed nanoindentation, Model. Simul. Mater. Sc. 10 (2002) 319.

[107] S. Kisin, J. B. Vukic, P. G. T. Varst, G. With, C. E. Koning, Estimating the polymer-metal work of adhesion from molecular dynamics simulations, Chem. Mater. 19 (2007) 903–907.

[108] Q. Zhang, Y. Qi, L. G. Hector, T. Cagin, W. A. Goddard, Origin of static friction and its relationship to adhesion at the atomic scale, Phys. Rev. B 75 (2007) 144114.

[109] K. Nagao, J. B. Neaton, N. W. Ashcroft, First-principles study of adhesion at Cu/SiO_2 interfaces, Phys. Rev. B 68 (2003) 125403.

[110] M. D. Kriese, N. R. Moody, W. W. Gerberich, Effects of annealing and interlayers on the adhesion energy of copper thin films to SiO_2/Si substrates, Acta Mater. 46 (1998) 6623–6630.

[111] R. Colaço, An AFM study of single-contact abrasive wear: The rabinowicz wear equation revisited, Wear 267 (2009) 1772–1776.

[112] Y. Mo, I. Szlufarska, Roughness picture of friction in dry nanoscale contacts, Phys. Rev. B 81 (2010) 035405.

[113] S. Cheng, M. O. Robbins, Defining contact at the atomic scale, Tribol. Lett. 39 (2010) 329–348.

[114] T. Liu, G. Liu, P. Wriggers, S. Zhu, Study on contact characteristic of nanoscale asperities by using molecular dynamics simulations, J. Tribol. 131 (2009) 022001.

[115] T. D. Jacobs, K. E. Ryan, P. L. Keating, D. S. Grierson, J. A. Lefever, K. T. Turner, J. A. Harrison, R. W. Carpick, The effect of atomic-scale roughness on the adhesion of nanoscale asperities: A combined simulation and experimental investigation, Tribol. Lett. (2013) 1–13.

[116] K. E. Ryan, P. L. Keating, T. D. Jacobs, D. S. Grierson, K. T. Turner, R. W. Carpick, J. A. Harrison, Simulated adhesion between realistic hydrocarbon materials: Effects of composition, roughness, and contact point, Langmuir 30 (2014) 2028–2037.

[117] W. Gao, R. Huang, Effect of surface roughness on adhesion of graphene membranes, J. Phys. D: Appl. Phys. 44 (2011) 452001.

[118] N. Mulakaluri, B. Persson, Adhesion between elastic solids with randomly rough surfaces: Comparison of analytical theory with molecular-dynamics simulations, Eur. Phys. J. (2011) 66003.

[119] D.-L. Liu, J. Martin, N. Burnham, Optimal roughness for minimal adhesion, Appl. Phys. Lett. 91 (2007) 043107.

[120] J. Katainen, M. Paajanen, E. Ahtola, V. Pore, J. Lahtinen, Adhesion as an interplay between particle size and surface roughness, J. Colloid Interf. Sci. 304 (2006) 524–529.

[121] S. N. Ramakrishna, L. Y. Clasohm, A. Rao, N. D. Spencer, Controlling adhesion force by means of nanoscale surface roughness, Langmuir 27 (2011) 9972–9978.

[122] Y. I. Rabinovich, J. J. Adler, A. Ata, R. K. Singh, B. M. Moudgil, Adhesion between nanoscale rough surfaces: I. role of asperity geometry, J. Colloid Interf. Sci. 232 (2000) 10–16.

[123] Y. I. Rabinovich, J. J. Adler, A. Ata, R. K. Singh, B. M. Moudgil, Adhesion between nanoscale rough surfaces: II. measurement and comparison with theory, J. Colloid Interf. Sci. 232 (2000) 17–24.

[124] A. Li, Y. Liu, I. Szlufarska, Effects of interfacial bonding on friction and wear at silica/silica interfaces, Tribol. Lett. 56 (2014) 481–490.

[125] X. Hu, S. Sundararajan, A. Martini, The effects of adhesive strength and load on material transfer in nanoscale wear, Comput. Mater. Sci. 95 (2014) 464–469.

[126] L. Zhang, C. Tang, Friction and wear of diamond–silicon nano-systems: Effect of moisture and surface roughness, Wear 302 (2013) 929–936.

[127] M. Baskes, Modified embedded-atom potentials for cubic materials and impurities, Phys. Rev. B 46 (1992) 2727.

[128] B. Jelinek, S. Groh, M. Horstemeyer, J. Houze, S. Kim, G. Wagner, A. Moitra, M. Baskes, Modified embedded atom method potential for al, si, mg, cu, and fe alloys, Phys. Rev. B 85 (2012) 245102.

[129] V. N. Koinkar, B. Bhushan, Scanning and transmission electron microscopies of single-crystal silicon microworn/machined using atomic force microscopy, J. Mater. Res. 12 (1997) 3219–3224.

[130] J. N. Israelachvili, Intermolecular and surface forces: revised third edition, Academic press, 2011.

[131] F. F. Abraham, I. P. Batra, S. Ciraci, Effect of tip profile on atomic-force microscope images: a model study, Phys. Rev. Lett. 60 (1988) 1314–1317.

[132] C. Odin, J. Aimé, Z. El Kaakour, T. Bouhacina, Tip's finite size effects on atomic force microscopy in the contact mode: simple geometrical considerations for rapid estimation of apex radius and tip angle based on the study of polystyrene latex balls, Surf. Sci. 317 (1994) 321–340.

[133] M. A. Lantz, B. Gotsmann, P. Jaroenapibal, T. D. Jacobs, S. D. O′Connor, K. Sridharan, R. W. Carpick, Wear-resistant nanoscale silicon carbide tips for scanning probe applications, Adv. Funct. Mater. 22 (2012) 1639–1645.

[134] H. Edwards, R. McGlothlin, U. Elisa, Vertical metrology using scanning-probe microscopes: imaging distortions and measurement repeatability, J. Appl. Phys. 83 (1998) 3952–3971.

[135] R. Aghababaei, D. H. Warner, J.-F. Molinari, Critical length scale controls adhesive wear mechanisms, Nat. Commun. 7 (2016) 1–8.

[136] Y. Yang, L. Huang, Y. Shi, Adhesion suppresses atomic wear in single-asperity sliding, Wear 352 (2016) 31–41.

[137] L. Dai, V. Sorkin, Y. Zhang, Effect of surface chemistry on the mechanisms and governing laws of friction and wear, ACS Appl. Mater. Interf. 8 (2016) 8765–8772.

[138] J. Furustig, I. Dobryden, A. Almqvist, N. Almqvist, R. Larsson, The measurement of wear using AFM and wear interpretation using a contact mechanics coupled wear model, Wear 350–351 (2016) 74–81.

[139] D. Mondal, S. Das, R. Rao, M. Singh, Effect of SiC addition and running-in-wear on the sliding wear behaviour of Al–Zn–Mg aluminium alloy, Mater. Sci. Eng. A 402 (2005) 307–319.

[140] Y.-R. Jeng, Z.-W. Lin, S.-H. Shyu, Changes of surface topography during running-in process, J. Tribol. 126 (2004) 620–625.

[141] L. Chen, S. H. Kim, X. Wang, L. Qian, Running-in process of Si-SiO_x/SiO_2 pair at nanoscale-sharp drops in friction and wear rate during initial cycles, Friction 1 (2013) 81–91.

[142] X. Hu, M. V. P. Altoe, A. Martini, Amorphization-assisted nanoscale wear during the running-in process, Wear 370 (2017) 46–50.

[143] W. Humphrey, A. Dalke, K. Schulten, VMD: visual molecular dynamics, J. Mol. Graphics 14 (1996) 33–38.

[144] E. R. Cruz-Chu, A. Aksimentiev, K. Schulten, Water-silica force field for simulating nanodevices, J. Phys. Chem. B 110 (2006) 21497–21508.

[145] T.-R. Shan, B. D. Devine, J. M. Hawkins, A. Asthagiri, S. R. Phillpot, S. B. Sinnott, et al., Second-generation charge-optimized many-body potential for Si/SiO_2 and amorphous silica, Phys. Rev. B 82 (2010) 235302.

[146] D. B. Asay, S. H. Kim, Evolution of the adsorbed water layer structure on silicon oxide at room temperature, J. Phys. Chem. B 109 (2005) 16760–16763.

[147] A. Stukowski, Visualization and analysis of atomistic simulation data with OVITO–the Open Visualization Tool, Model. Simul. Mater. Sci. 18 (2009) 015012.

[148] E. Maras, O. Trushin, A. Stukowski, T. Ala-Nissila, H. Jonsson, Global transition path search for dislocation formation in Ge on Si (001), Comput. Phys. Commun. 205 (2016) 13–21.

[149] B. Bhushan, S. Sundararajan, Micro/nanoscale friction and wear mechanisms of thin films using atomic force and friction force microscopy, Acta Mater. 46 (1998) 3793–3804.

[150] H. Li, T. Xu, C. Wang, J. Chen, H. Zhou, H. Liu, Humidity dependence on the friction and wear behavior of diamond-like carbon film in air and nitrogen environments, Diamond Relat. Mater. 15 (2006) 1585–1592.

[151] M. Shafiei, A. Alpas, Effect of sliding speed on friction and wear behaviour of nanocrystalline nickel tested in an argon atmosphere, Wear 265 (2008) 429–438.

[152] F. Shimizu, S. Ogata, J. Li, Theory of shear banding in metallic glasses and molecular dynamics calculations, Mater. Trans. 48 (2007) 2923–2927.

[153] M. Falk, J. Langer, Dynamics of viscoplastic deformation in amorphous solids, Phys. Rev. E 57 (1998) 7192–7205.

[154] A. Cao, Y. Cheng, E. Ma, Structural processes that initiate shear localization in metallic glass, Acta Mater. 57 (2009) 5146–5155.

[155] Y.-C. Wang, W. Zhang, L.-Y. Wang, Z. Zhuang, E. Ma, J. Li, Z.-W. Shan, In situ TEM study of deformation-induced crystalline-to-amorphous transition in silicon, NPG Asia Mater. 8 (2016) e291.

[156] R. Garcia, R. Perez, Dynamic atomic force microscopy methods, Surf. Sci. Rep. 47 (2002) 197–301.

[157] R. García, Amplitude modulation atomic force microscopy, John Wiley & Sons, 2010.

[158] J. Tamayo, R. Garcia, Deformation, contact time, and phase contrast in tapping mode scanning force microscopy, Langmuir 12 (1996) 4430–4435.

[159] R. Garcia, A. San Paulo, Attractive and repulsive tip-sample interaction regimes in tapping-mode atomic force microscopy, Phys. Rev. B 60 (1999) 4961.

[160] R. Garcia, A. San Paulo, Dynamics of a vibrating tip near or in intermittent contact with a surface, Phys. Rev. B 61 (2000) R13381.

[161] V. Vahdat, D. S. Grierson, K. T. Turner, R. W. Carpick, Nano-scale forces, stresses, and tip geometry evolution of amplitude modulation atomic force microscopy probes, in: ASME 2011 International Design Engineering Technical Conferences and Computers and Information in Engineering Conference, American Society of Mechanical Engineers, 2011, pp. 543–549.

[162] J. Tamayo, R. Garcia, Relationship between phase shift and energy dissipation in tapping-mode scanning force microscopy, Appl. Phys. Lett. 73 (1998) 2926–2928.

[163] R. Höper, T. Gesang, W. Possart, O.-D. Hennemann, S. Boseck, Imaging elastic sample properties with an atomic force microscope operating in the tapping mode, Ultramicroscopy 60 (1995) 17–24.

[164] N. F. Martínez, R. García, Measuring phase shifts and energy dissipation with amplitude modulation atomic force microscopy, Nanotechnology 17 (2006) S167.

[165] S. Santos, N. H. Thomson, Energy dissipation in a dynamic nanoscale contact, Appl. Phys. Lett. 98 (2011) 013101.

[166] H. Kim, G. Venturini, A. Strachan, Molecular dynamics study of dynamical contact between a nanoscale tip and substrate for atomic force microscopy experiments, J. Appl. Phys. 112 (2012) 094325.

[167] N. Onofrio, G. Venturini, A. Strachan, Molecular dynamic simulation of tip-polymer interaction in tapping-mode atomic force microscopy, J. Appl. Phys. 114 (2013) 094309.

[168] A. Abdurixit, A. Baratoff, E. Meyer, Molecular dynamics simulations of dynamic force microscopy: applications to the si (111)-7× 7 surface, Appl. Surf. Sci. 157 (2000) 355–360.

[169] B. Bat-Uul, S. Fujii, T. Shiokawa, T. Ohzono, M. Fujihira, Molecular dynamics simulation of non-contact atomic force microscopy of self-assembled monolayers on au (111), Nanotechnology 15 (2004) 710.

[170] T. Shiokawa, T. Ohzono, M. Fujihira, Molecular dynamics simulation of non-contact atomic force microscopy of an ordered monolayer consisting of single united atoms chemisorbed strongly on a continuum substrate, Appl. Surf. Sci. 210 (2003) 117–122.

[171] S. J. Stuart, A. B. Tutein, J. A. Harrison, A reactive potential for hydrocarbons with intermolecular interactions, J. Chem. Phys. 112 (2000) 6472–6486.

[172] M. Neek-Amal, F. Peeters, Nanoindentation of a circular sheet of bilayer graphene, Phys. Rev. B 81 (2010) 235421.

[173] R. Garcia, C. Gomez, N. Martinez, S. Patil, C. Dietz, R. Magerle, Identification of nanoscale dissipation processes by dynamic atomic force microscopy, Phys. Rev. Lett. 97 (2006) 016103.

[174] C. J. Gomez, R. Garcia, Determination and simulation of nanoscale energy dissipation processes in amplitude modulation AFM, Ultramicroscopy 110 (2010) 626–633.

[175] S. Santos, K. R. Gadelrab, A. Silvernail, P. Armstrong, M. Stefancich, M. Chiesa, Energy dissipation distributions and dissipative atomic processes in amplitude modulation atomic force microscopy, Nanotechnology 23 (2012) 125401.

[176] B. Derjaguin, V. Muller, Y. Toporov, Effect of contact deformations on the adhesion of particles, Journal of Colloid and Interface Science 53 (2) (1975) 314 – 326.

[177] R. W. Carpick, M. Salmeron, Scratching the surface: fundamental investigations of tribology with atomic force microscopy, Chem. Rev. 97 (1997) 1163–1194.

[178] E. Meyer, H. J. Hug, R. Bennewitz, Scanning probe microscopy: the lab on a tip, Springer Science, 2013.

[179] D. J. Keller, F. S. Franke, Envelope reconstruction of probe microscope images, Surf. Sci. 294 (1993) 409–419.

[180] H. Hölscher, D. Ebeling, U. D. Schwarz, Friction at atomic-scale surface steps: experiment and theory, Phys. Rev. Lett. 101 (2008) 246105.

[181] D. R. Baselt, J. D. Baldeschwieler, Lateral forces during atomic force microscopy of graphite in air, J Vac. Sci. Technol. B 10 (1992) 2316–2322.

[182] D. P. Hunley, T. J. Flynn, T. Dodson, A. Sundararajan, M. J. Boland, D. R. Strachan, Friction, adhesion, and elasticity of graphene edges, Phys. Rev. B 87 (2013) 035417.

[183] T. Müller, M. Lohrmann, T. Kässer, O. Marti, J. Mlynek, G. Krausch, Frictional force between a sharp asperity and a surface step, Phys. Rev. Lett. 79 (1997) 5066.

[184] P. Steiner, E. Gnecco, F. Krok, J. Budzioch, L. Walczak, J. Konior, M. Szymonski, E. Meyer, Atomic-scale friction on stepped surfaces of ionic crystals, Phys. Rev. Lett. 106 (2011) 186104.

[185] Z. Ye, A. Martini, Atomic friction at exposed and buried graphite step edges: experiments and simulations, Appl. Phys. Lett. 106 (2015) 231603.

[186] X. Hu, N. Chan, A. Martini, P. Egberts, Tip convolution on hopg surfaces measured in am-afm and interpreted using a combined experimental and simulation approach, Nanotechnology 28 (2016) 025702.

[187] T. Kumagai, S. Izumi, S. Hara, S. Sakai, Development of bond-order potentials that can reproduce the elastic constants and melting point of silicon for classical molecular dynamics simulation, Comput. Mater. Sci. 39 (2007) 457–464.

[188] A. San Paulo, R. García, Tip-surface forces, amplitude, and energy dissipation in amplitude-modulation (tapping mode) force microscopy, Phys. Rev. B 64 (2001) 193411.

[189] A. A. Feiler, J. Stiernstedt, K. Theander, P. Jenkins, M. W. Rutland, Effect of capillary condensation on friction force and adhesion, Langmuir 23 (2007) 517–522.

[190] Z. Ye, P. Egberts, G. H. Han, A. C. Johnson, R. W. Carpick, A. Martini, Load-dependent friction hysteresis on graphene, ACS Nano 10 (2016) 5161–5168.

[191] X. Hu, A. Martini, Atomistic simulation of the effect of roughness on nanoscale wear, Comput. Mater. Sci. 102 (2015) 208–212.

[192] X. Hu, P. Egberts, Y. Dong, A. Martini, Molecular dynamics simulation of amplitude modulation atomic force microscopy, Nanotechnology 26 (2015) 235705.

[193] H. V. Guzman, A. P. Perrino, R. Garcia, Peak forces in high-resolution imaging of soft matter in liquid, ACS Nano 7 (4) (2013) 3198–3204.

[194] F. Yang, R. W. Carpick, D. J. Srolovitz, Mechanisms of contact, adhesion and failure of metallic nanoasperities in the presence of adsorbates: Toward conductive contact design, ACS Nano.